RICE UNIVERSITY

Multi-Modal Imaging Techniques for Early Cancer Diagnostics

by

Noah Denis Bedard

A THESIS SUBMITTED
IN PARTIAL FULFILLMENT OF THE
REQUIREMENTS FOR THE DEGREE

Doctor of Philosophy

APPROVED, THESIS COMMITTEE

Tomasz S. Tkaczyk, Chair, Assistant Professor
Bioengineering, Electrical and Computer Engineering

Rebecca Richards-Kortum, Stanley C. Moore Professor
Bioengineering

Erzsébet Merényi, Professor
Statistics, Electrical and Computer Engineering

Ann M. Gillenwater, Professor, Head and Neck Surgery
The University of Texas at MD Anderson Cancer Center

HOUSTON, TEXAS
April 2012

ABSTRACT

Multi-Modal Imaging Techniques for Early Cancer Diagnostics

by

Noah Bedard

Cancer kills more Americans under the age of 75 than any other disease. Although most cancers occur in epithelial surfaces that can be directly visualized, the majority of cases are detected at an advanced stage. Optical imaging and spectroscopy may provide a solution to the need for non-invasive and effective early detection tools. These technologies are capable of examining tissue over a wide range of spatial scales, with widefield macroscopic imaging typically spanning several square-centimeters, and high resolution *in vivo* microscopy techniques enabling cellular and subcellular features to be visualized. This work presents novel technologies in two important areas of optical imaging: high resolution imaging and widefield imaging. For subcellular imaging applications, new high resolution endomicroscope techniques are presented with improved lateral resolution, larger field-of-view, increased contrast, decreased background signal, and reduced cost compared to existing devices. A new widefield optical technology called multi-modal spectral imaging is also developed. This technique provides real-time *in vivo* spectral data over a large field-of-view, which is useful for detecting biochemical alterations associated with neoplasia. The described devices are compared to existing technologies, tested using *ex vivo* tissue specimens, and evaluated for diagnostic potential in a multi-patient oral cancer clinical trial.

Acknowledgments

I would like to thank my advisor, Dr. Tomasz Tkaczyk, for his guidance and friendship during the past six years. His passion for research and in-depth technical knowledge has kept me excited, inquisitive, and focused throughout my graduate education.

Many thanks to the other committee members: Dr. Rebecca Richards-Kortum, Dr. Ann Gillenwater, and Dr. Erzsébet Merényi for their expert advice and help along the way. I am honored to have such a talented committee.

I would like to thank members and alumni of the Tkaczyk and Kortum labs for their friendship, advice, and support, including Matt Kyrish, Brian McCall, Dr. Liang Gao, Thuc-Uyen Nguyen, Dr. Nathan Hagen, Aaron Hu, Dr. Mike Pawlowski, Tim Quang, Sharon Mondrik, Anne Hellebust, and Nadhi Thekkek. At M.D. Anderson Cancer Center, Vijayashree Bhattar helped coordinate clinical studies and Dr. Michelle Williams reviewed pathology slides.

I would also to thank Dr. Mark Pierce and Dr. Robert Kester for their mentorship.

Most importantly, I would like to thank my parents Martha and Denis, who have inspired and supported me every step of the way. I could not have done it without you.

This work was funded by NIH grants R01CA124319, R01EB002179, R01CA103830, and R21EB009186.

Contents

List of Figures

List of Tables

Chapter 1

Introduction

1.1. Objectives and Specific Aims

The objective of this research is to develop improved optical imaging techniques for cancer detection and to evaluate their diagnostic potential. A promising procedure for optical diagnostics is to use a two-step approach where widefield imaging is used to identify suspicious regions within a large area of tissue, and then high resolution endomicroscopy is used for the final diagnosis. This work presents advancements in both widefield imaging and high resolution endomicroscopy techniques. To improve upon current endomicroscope devices, new techniques are presented that (1) expand the field-of-view, (2) increase lateral resolution, and (3) provide axial sectioning. To improve widefield imaging, a new spectral imaging modality is developed that allows visualization of spectral features over a large field-of-view. The techniques are tested on *ex vivo* and *in vivo* tissue specimens and also evaluated in an oral cancer clinical trial.

The specific aims are as follows:

Specific Aim 1: Develop and test high resolution endomicroscope systems and techniques that improve existing clinical devices and support miniature endoscope objective lenses.

Specific Aim 2: Develop a multi-modal widefield spectral imaging device and evaluate its diagnostic value for oral cancer in a pilot clinical study.

The impact of this work is to provide new effective and user-friendly tools that increase clinicians' ability to diagnose cancer at the point-of-care. Knowledge gained through this research will facilitate integration of improved imaging technologies for cancer screening and surveillance.

1.2. Overview

This dissertation describes the development of (1) high resolution endomicroscope techniques and (2) a widefield spectral imaging technology for cancer diagnosis. It presents four endomicroscope technologies, a multi-modal widefield imaging spectrometer, and an oral cancer clinical study. The organization of the dissertation is as follows.

Chapter 1 lists the specific aims of the research and provides a brief overview of the topics to be discussed.

Chapter 2 provides background information on oral cancer statistics and disease progression.

Chapter 3 discusses the role of optical imaging for detection and diagnosis of cancer. The content is, *in extenso*, the work published in [1]. It provides an overview of multi-modal optical imaging, with an emphasis on low-resource settings. Concepts in widefield autofluorescence imaging, high resolution endomicroscopy, and combined two-step optical screening are discussed and implemented in a proof-of-concept system.

Chapter 4 presents a technique to increase the field-of-view of endomicroscopes. Details of the algorithm are given and the method is tested on tissue specimens.

Chapter 5 presents two techniques to provide axial sectioning in endomicroscopes. The design and construction of each device is described. The devices are compared with existing high resolution imaging technologies and tested on tissue specimens.

Chapter 6 presents a technique to increase lateral resolution of an endomicroscope using spectral encoding. The implementation and calibration of the new modality is described. The device is tested on standard optical targets and an *in vivo* tissue specimen.

Chapter 7 introduces a new spectral imaging device. Calibration and characterization of the device is described. Oxygen saturation maps of tissue are also shown.

Chapter 8 presents the design and construction of a multi-modal widefield imaging spectrometer for clinical studies. Optical specifications, software, and the design of a clinical trial are described. Autofluorescence/reflectance images and spectra are shown for different tissue regions.

Chapter 9 summarizes the results of the various technologies, reviews the impact of the research, and discusses future work.

Chapter 2

Background

2.1. Motivation and Significance

Cancer is the second leading cause of death in the United States. While over 80% of cancers occur in epithelial surfaces, most of which can be directly visualized, the majority of cases are detected at an advanced stage. The stage that the disease is detected is directly related to survival, therefore early detection is vital. The ultimate goal of this work is to develop optical imaging techniques for the early diagnosis of cancer in a variety of tissue sites. However, for the research reported here, we particularly focus on oral cancer, because the oral cavity is convenient model for device testing.

Oral cancer is a major global health problem. Each year there are approximately 310,000 new cases worldwide [2]. In the US alone, it is a significant problem with 34,000 new cases and 7,550 deaths in 2007, yet the problem is much greater in developing countries [3, 4]. In India, for example, oral cancer is the most common cancer in men and the third most common cancer in women [4]. Localized disease can be more successfully

and easily treated than advanced disease, leading to an optimistic five-year survival rate [5]. Unfortunately, 2/3 of patients in the US are diagnosed with more advanced disease that leads to much greater mortality. The treatment for late stage disease is also more aggressive and can lead to permanent physical and physiological damage, which decreases quality of life.

Although the need for early diagnosis is clear, there are many factors which contribute to delay. Localized oral cancer may appear benign to a physician and could remain unsuspicious until an advanced stage. Lesions that are suspicious should be biopsied to determine disease status, but the invasiveness of the procedure could lead to hesitation that prolongs diagnosis. Biopsies also takes time to process and examine, adding to patient stress and prolonging the time to diagnosis.

2.2. Oral cancer disease progression

The oral cavity includes the buccal mucosa, the upper and lower alveolus and gingiva, the hard palate, the tongue, and the floor of the mouth. Over 90% of oral cancers are squamous cell carcinomas, and most of these result from genetic alterations caused by years of tobacco and alcohol exposure [5, 6]. Stratified squamous cells line the oral mucosa and reside above the basement membrane and stroma. In normal tissue, tall basal cells line the basement membrane with progressively flatter cells approaching the surface, whereas in squamous cell carcinoma this differentiation does not occur. Dentists sometimes screen for white or red oral lesions, known as leukoplakia or erythroplakia respectively, which can indicate or accompany squamous cell carcinoma [7].

Screening techniques for cancer are better understood by examining the pathophysiology of the disease. Cancer is generally defined as uncontrolled growth and spread of abnormal cells [8]. The development of an invasive cancer from normal cells follows a multi-step progression of genetic changes that usually takes years to occur. The major defect in cancer cells is within the regulatory mechanisms that govern cell proliferation and homeostasis. From this fact, it has been suggested that all cancers have the same set of at least six functional capabilities, sometimes called the "hallmarks of cancer": self-sufficiency in growth signals, insensitivity to anti-growth signals, tissue invasion and metastasis, limitless replicative potential, sustained angiogenesis, and evasion of apoptosis [9].

These acquired capabilities of cancer are also associated with early morphological and biochemical changes at the cellular and tissue levels, which can allow precancer to be distinguished from normal tissue. Cancerous lesions are typically made up of genetically unstable, poorly differentiated, rapidly dividing cells. From early on, these cells cause a number of changes in the tissue that indicate precancer and such lesions are referred to as dysplasia. Recognized biochemical changes include changes in NADH and FAD activity, decreased collagen crosslinks, and an upregulation of proteins such as EGFR, HER2, and MMP [10-14]. The morphological alterations associated with these cells include: enlarged nuclei, hyperchromatic nuclei, pleomorphism, keratinization, loss of polarity of basal cells, and irregular epithelial stratification [7]. The best indicators for dysplasia are usually nuclear-to-cytoplasmic ratio (N/C), pleomorphic cells and nuclei, and increased nuclear chromatin. Histology with hematoxylin and eosin staining is used to analyze these characteristics, and is currently the gold standard for oral cancer diagnosis [15].

Mild, moderate, and severe dysplasia are characterized by abnormal changes in the lower one-third, two-thirds, and entire epithelium, respectively. Dysplasia throughout the entire epithelium that has not invaded through the basement membrane is called carcinoma *in situ* [16]. Cancer that has progressed beyond the basement membrane is further classified into stages that relate to size, lymph node involvement, and spread to other regions of the body [6].

2.3. Optical imaging and spectroscopy for cancer diagnostics

Current oral cancer screening techniques are generally inadequate, as evidenced by the fact that the 5-year survival rate for oral cancer has remained relatively unchanged for the last 30 years. Therefore, new technologies are needed to detect precancerous lesions. The optical detection technologies presented in this dissertation can be divided into two categories: widefield devices and high resolution devices (see Figure 2-1: Widefield and high resolution optical techniques for cancer detection.. Wide-field devices survey multiple centimeters of tissue at one time using specialized light sources and filters. These systems show increased visibility of tissue microvasculature and can reveal changes associated with tissue autofluorescence. Typically they can detect precancerous lesions with high sensitivity but can have false positives (such as inflammation, lichen planus, hyperkeratosis) which leads to low specificity. Ideally, a second high-resolution device is used to interrogate localized tissue properties. High-resolution imaging is often called endomicroscopy or microendoscopy and includes devices such as confocal microscopy and OCT. These devices can reveal cellular morphology and function, which yields both high sensitivity and specificity. Another

technique called point spectroscopy can measure the reflectance and autofluorescence properties at a localized region of tissue, which is associated with changes in hemoglobin absorption as well as epithelial/stromal fluorescence. Preferably, high resolution devices will be used with wide-field techniques to enable screening that is both fast and effective. The following chapter expands on the role of multimodal optical imaging for early cancer detection.

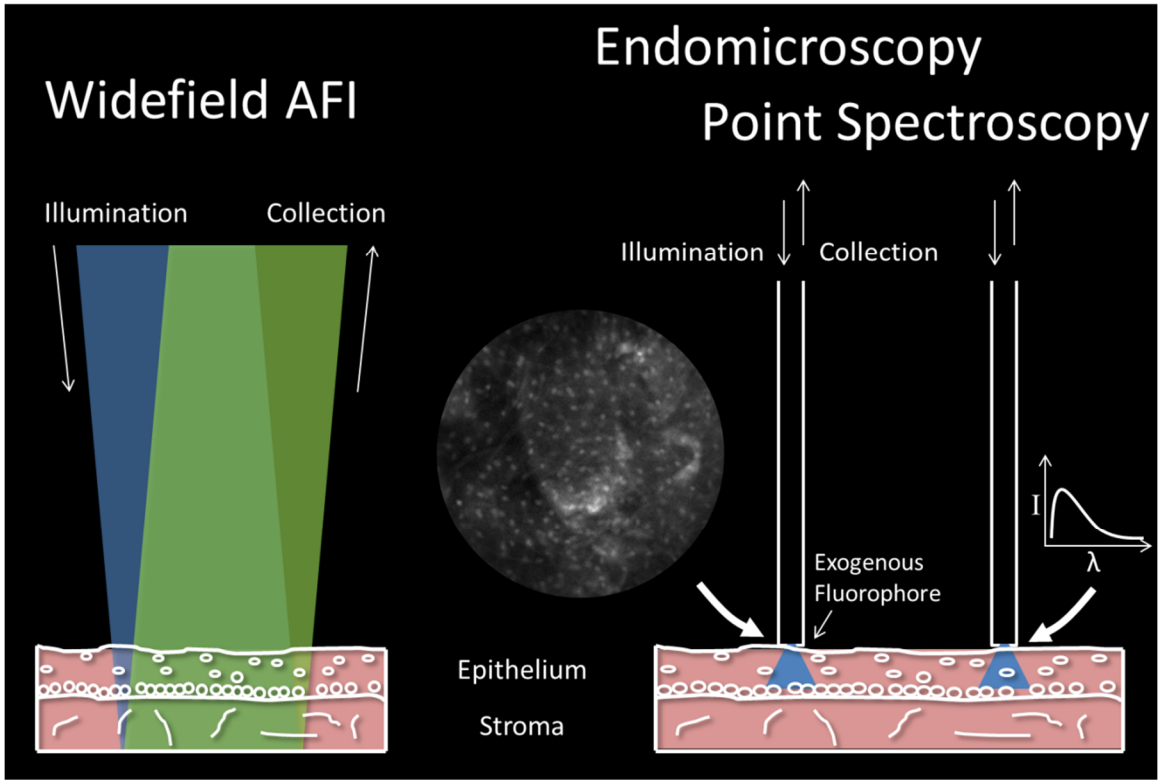

Figure 2-1: Widefield and high resolution optical techniques for cancer detection.

Chapter 3

Emerging roles for multimodal optical imaging in early cancer detection*

*The contents of this chapter have been published in the following journal article: N. Bedard, M. Pierce, A. El-Nagger, S. Anandasabapathy, A. Gillenwater, and R. Richards-Kortum, "Emerging roles for multimodal optical imaging in early cancer detection: a global challenge.," Technol Cancer Res Treat 9, 211-217 (2010).

Medical imaging technologies have become increasingly important in the clinical management of cancer, and now play key roles in cancer screening, diagnosis, staging, and monitoring response to treatment. Standard imaging modalities such as MRI, PET, and CT require significant financial resources and infrastructure, which limits access to these modalities to those patients in high-resource settings. In contrast, optical imaging strategies, with the potential for reduced cost and enhanced portability, are emerging as additional tools to facilitate the early detection and diagnosis of cancer. This chapter presents a vision for an expanding role for optical imaging in global cancer management, including screening, early detection at the point-of-care, biopsy guidance, and real-time

histology. Multi-modal optical imaging – the combination of widefield and high resolution imaging - has the potential to aid in the detection and management of precancer and early cancer for traditionally underserved populations. Several recent widefield and high-resolution optical imaging technologies are described, along with requirements for implementing such devices into lower-resource settings.

3.1. Medical Imaging and Cancer

Medical imaging plays a central role in the detection and diagnosis of cancer. Screening, diagnosis, and staging all rely on the ability of imaging technologies to identify molecular and morphologic alterations associated with the onset and progression of neoplastic disease. Current treatment paradigms also rely heavily on imaging, for image-guided therapy, minimally-invasive surgery, and to monitor treatment response. Computed tomography (CT), ultrasound, and magnetic resonance imaging (MRI) are well-established imaging modalities that can provide *in situ* anatomical data on the size, shape, and location of tumors. Relatively newer technologies such as positron emission tomography (PET) and single-photon-emission CT (SPECT) add the ability to detect and monitor functional activity of tumors, revealing both the location and metabolic activity of disease. Each of these imaging platforms can also take advantage of the growing array of molecularly-targeted contrast agents to detect and monitor distinct biochemical processes involved in neoplastic transformation [17, 18].

While the enhanced capabilities of these imaging systems will continue to play a key role in improving patient care, the financial cost and infrastructure required to establish and maintain them restricts their use largely to regional healthcare centers in

industrialized countries. This is clearly underscored by the disparity in the availability of these technologies. As an example, a 2006 estimate placed the number of MRI machines in the US at around 11,000. Two years later in 2008, the first MRI machine was installed in Malawi, and the system is currently shared with neighboring Mozambique and Zambia, two countries without a single MRI scanner. Even in developing countries with rapidly emerging economies such as India, there are only 0.5 MRI machines per million inhabitants, compared to 37 machines per million persons in the US [19].

Today, more than 70% of the world's cancer deaths occur in these low- to middle-income countries, where 80% of patients present with advanced disease at the time of diagnosis [20, 21]. These figures are unlikely to be affected by a widespread infusion of high-level imaging technology in the foreseeable future. Even in developed countries, the presence of diagnostic imaging technology alone does not equate to widespread access. Patients in the US who are uninsured or who have Medicaid insurance are significantly more likely to be diagnosed with late stage cancer, and have significantly lower survival rates than patients with private insurance [22]. At a time when the global incidence of cancer is rapidly increasing and 47 million Americans lack health insurance [23], there is an urgent need for effective and affordable tools and technologies to facilitate early detection, prevention, and treatment of cancer in low resource settings.

Optical imaging is a new technology which may provide a potential solution to the global need for affordable imaging tools to aid in the early detection and management of cancer. While healthcare providers have traditionally used optical tools such as endoscopes, colposcopes, and surgical microscopes in cancer management, a new generation of instruments is being developed which can detect not just reflected white

light, but additional signals arising from cancer biomarkers, carried in the fluorescence, polarization, and narrowband reflectance of light. These systems are capable of examining tissue over a wide range of spatial scales, with widefield macroscopic imaging typically spanning several square-centimeters, and high-resolution *in vivo* microscopy techniques enabling cellular and subcellular features to be visualized [17, 24, 25]. Optical instrumentation is relatively inexpensive, using mass-fabricated components developed by the telecommunications and consumer electronics industries. A second key factor, which we focus on here, is the recent emergence of multimodal optical imaging systems, simultaneously providing wide-field *and* high-resolution optical imaging, within cost-effective, portable, and even battery-powered formats.

This chapter presents our vision of an expanding role for optical imaging in cancer management, through the example of a dual-resolution portable device that has potential to aid in early cancer detection and management for socioeconomically diverse populations.

3.2. Current Optical Imaging Techniques for Cancer Management

Widefield Optical Imaging: An Emerging Technology for Cancer Screening

Over 80% of malignancies occur in epithelial surfaces, most of which can be directly visualized [26]. Thus, many current procedures for cancer screening begin with visual inspection of the entire tissue surface at risk under white light illumination, often with additional low-power magnification. These techniques can be improved with narrow-band reflectance imaging (NBI) and autofluorescence imaging (AFI) to enhance

visualization of the microvasculature and monitor alterations in epithelial and stromal fluorescence associated with the early development of neoplasia [27]. Figure 3-1 illustrates the application of this technology to improve screening for lung cancer; white light and autofluorescence images acquired with light-induced fluorescence endoscopy

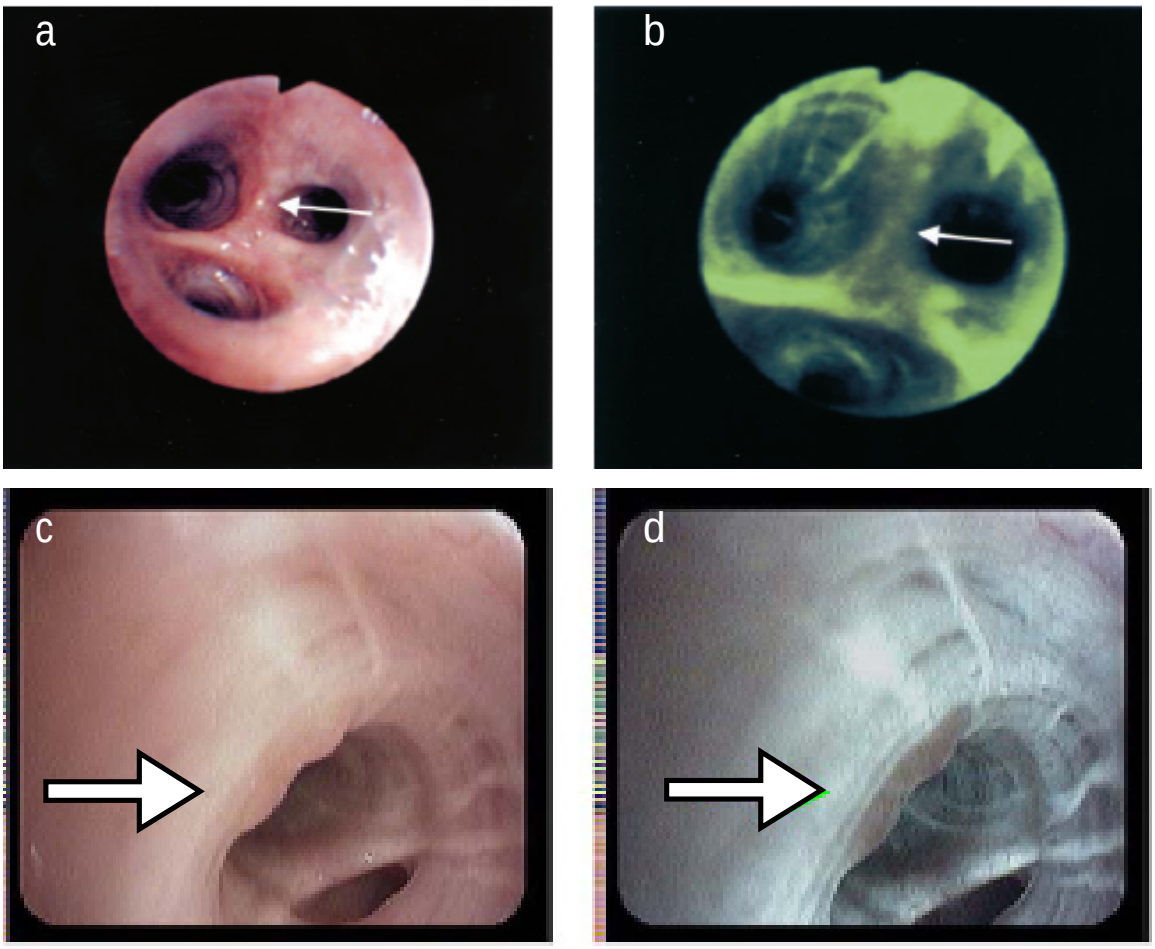

Figure 3-1: These images illustrate the application of light induced fluorescence endoscopy to improve screening for lung cancer with a widefield optical imaging system; white light and autofluorescence images acquired with light-induced fluorescence endoscopy (top, Xillix LIFE; bottom, Pentax 3000) show typical image features associated with atypical cells, with suspicious areas indicated by white arrows. The white light images (A, C) represent the clinician's conventional viewing mode, allowing anatomical inspection at low magnification. Autofluorescence images (B, D) are sensitive to the natural fluorescence of tissue, which originates predominantly from stromal collagen. The development of neoplasia is associated with loss of stromal autofluorescence and this loss of fluorescence intensity can be used to assist clinicians in identifying pre-cancerous and suspicious cancerous lesions (as shown by decreased fluorescence intensity within areas in B, D).

(Xillix LIFE, Pentax 3000) show representative image features associated with atypical cells. The white light images (Figure 3-1a,c) represent the clinician's conventional viewing mode, allowing anatomical inspection at low magnification. Autofluorescence images (Figure 3-1b,d) are sensitive to the natural fluorescence of tissue, which originates predominantly from stromal collagen. When illuminated with blue light, non-neoplastic tissue emits green fluorescent light.

The development of neoplasia is associated with loss of stromal autofluorescence and this loss of fluorescence intensity can be used to assist clinicians in identifying pre-cancerous and suspicious cancerous lesions (as evident in Figure 3-1b,d). This technique has been used in over 1600 patients world-wide; studies support an improved sensitivity of autofluorescence bronchoscopy over white light bronchoscopy alone (80% versus 40%) [28, 29].

Imaging systems based on similar principles have been developed and tested for cancer detection in several other organ sites, including the esophagus, cervix, and oral cavity. In 2008, Curvers *et al.* reported the results of a multicenter study that used white-light endoscopy with the addition of NBI and AFI to detect neoplastic lesions in 84 patients with Barrett's esophagus, a precursor of esophageal cancer [27]. Use of AFI identified 11 patients with early neoplasia in addition to the 16 identified by white-light alone, raising the targeted detection rate from 53% to 90%. These and other encouraging data from pre-clinical studies have led to the development of several commercially-available widefield multi-spectral imaging systems with FDA approval for early cancer detection, including the VELscope (oral), the Trimira-3000 (oral), the Olympus Lucera (GI), and the Xillix LIFE scope (lung). Newer spectral imaging techniques are being

developed to measure other cancer-related biomarkers such as total hemoglobin content and hemoglobin oxygen saturation, as a tool to detect tumor margins *in vivo* during surgery [30].

High-Resolution Optical Imaging: Applications in Early Detection, Margin Detection, and Real-time Histology

In current practice, tissue sites appearing suspicious for disease on visual inspection with white light are typically biopsied, enabling a pathologist to evaluate cellular morphology at the microscopic level. Recently, high-resolution optical techniques have been developed that can image tissue with sub-cellular resolution *in situ*, revealing morphologic indicators of neoplasia such as increased pleomorphism, changes in nuclear size and nuclear density and the presence of abnormal mitotic features, in addition to functional indicators when used in combination with targeted optical contrast agents [25]. A high-resolution confocal endoscope for imaging the mucosal lining of the esophagus and colon was evaluated during *in vivo* clinical studies by Polglase *et al.*, demonstrating the system's ability to visualize microscopic features including goblet cells and columnar epithelial cells, traditionally used by the pathologist in the diagnosis and staging of disease [31]. In Figure 3-2, a confocal microendoscope was used to image excised ovarian tissue after the application of acridine orange [32]. Fluorescence imaging enabled visualization of individual nuclei and the underlying stroma (Figure 3-2a-c). Images from a healthy ovary were characterized by a homogeneous distribution of nuclei, whereas images from carcinoma revealed a disordered tissue structure and variable nuclear size (Figure 3-2a,d). Other more subtle pathologic changes such as

sclerosis and endometriosis were also detectable (Figure 3-2e,f). These optical methods have been adapted for *in vivo* use at several organ sites, with a focus on guiding biopsy site selection to those locations with the highest diagnostic potential. As with the wide-field imaging systems described earlier, several high-resolution optical imaging systems have been commercialized and received FDA approval for cancer detection, including the Lucid confocal microscope, the Mauna Kea fiber-optic system, and the Pentax / Optiscan confocal endoscope.

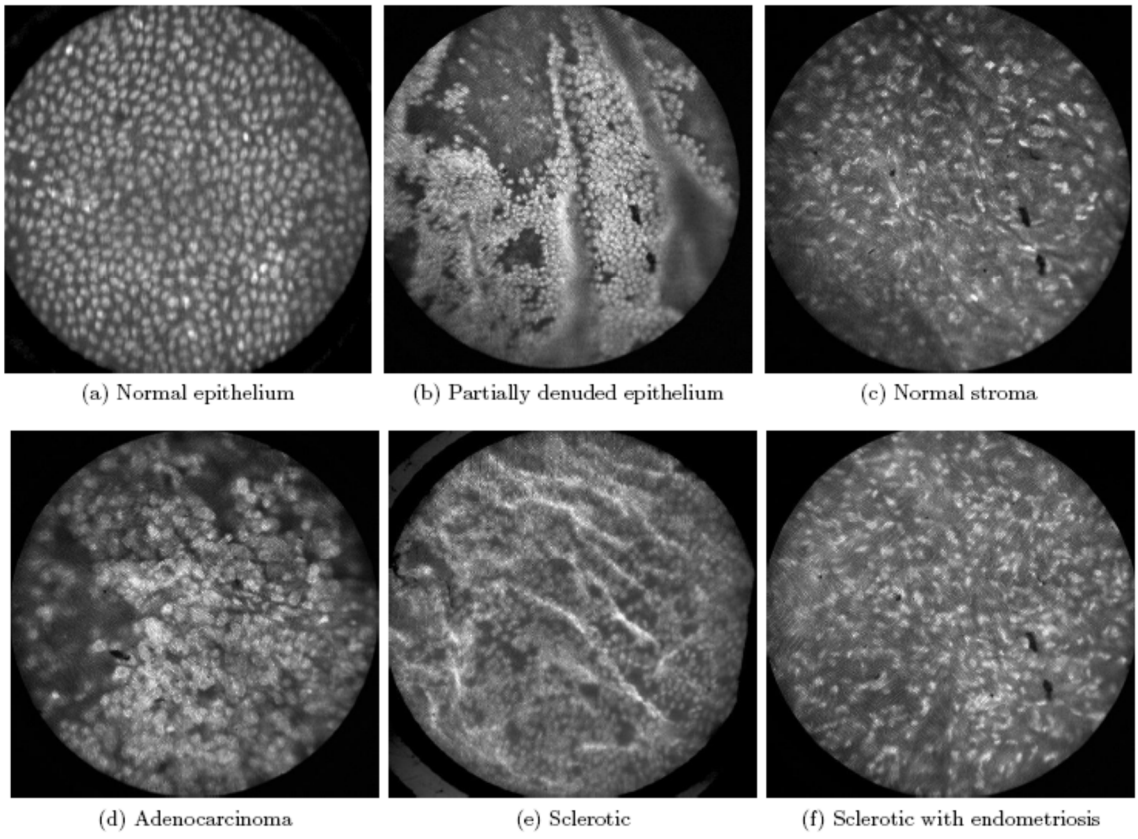

Figure 3-2: High-resolution confocal microendoscope images of excised ovarian tissue after the application of acridine orange. Fluorescence imaging enabled visualization of individual nuclei and the underlying stroma (A-C). Images from a healthy ovary were characterized by a homogeneous distribution of nuclei, whereas images from carcinoma revealed a disordered tissue structure and variable nuclear size (A, D). Other more subtle pathologic changes such as sclerosis and endometriosis were also detectable (E, F).

The same high resolution imaging techniques can potentially address the wider need for histopathology in settings where a pathology laboratory is either not available, less developed, or lacking expertise. Gareau *et al.* demonstrated that high-resolution optical imaging in the form of confocal microscopy can be used for margin evaluation during Mohs surgery for patients with basal cell carcinomas, providing an accurate diagnostic result in a much reduced time of frozen section histopathology [33].

Multimodal Optical Imaging

Each of these widefield and high-resolution systems has recognized strengths and weaknesses. In the same way that radiological imaging modalities have been combined to provide complementary diagnostic information (such as PET-CT, PET-MRI), widefield and high-resolution optical imaging systems have begun to be integrated into single platforms. In a 148-patient clinical study, Lam *et al.* performed high-resolution optical coherence tomography (OCT) imaging at sites initially inspected by widefield autofluorescence bronchoscopy [34]. Following guidance to suspicious sites by widefield imaging, OCT was then used to measure the local epithelial thickness and identify enlarged nuclei, allowing invasive cancer to be distinguished from carcinoma *in situ*, and dysplasia to be distinguished from metaplasia, hyperplasia, and normal tissue. The autofluorescence endoscope described by Curvers *et al.* incorporated the additional use of narrowband reflectance imaging to improve diagnostic specificity in Barrett's esophagus, as supported by a drop in the false positive rate from 81% to 26% [27]. It is likely that comprehensive screening and diagnosis of cancer will require the development

of such multi-modal imaging platforms, with the ability to initially survey large tissue areas at risk to identify abnormal regions with high diagnostic sensitivity. Targeted follow-up of those suspicious sites with high-resolution imaging can then be used to eliminate confounding factors such as inflammation that lead to false positive results, improving the overall specificity of cancer detection.

Portable Optical Systems: Translating Optical Imaging to Low-Resource Settings

While these optical imaging systems continue to demonstrate encouraging performance in clinical studies, they remain primarily a subject of research and validation in large referral hospital settings in industrialized countries. However, by leveraging advances in optoelectronic components, low-power processing hardware, and digital image analysis, these imaging systems have the potential to be successfully adapted and integrated into low-resource settings, addressing the current gap in cancer screening and surveillance strategies in this environment. A few examples of compact, battery-powered optical systems have been demonstrated, including portable colposcopes for cervical cancer screening [35, 36], and a hand-held visual inspection device for the oral cavity [37], each of which require the user to observe the tissue by eye.

We recently developed a battery-powered, portable system, capable of both widefield and high-resolution digital imaging, and have begun clinical studies to compare its performance against large-scale counterparts. The widefield imaging component was previously described by Rahman *et al.*, consisting of a commercially available surgical headlight system modified to include LED illumination for both white light and fluorescence excitation, and a high-sensitivity CCD camera for digital image acquisition

(Figure 3-3a) [38]. This portable screening system weighs only 3 lb and can alternatively be mounted on a camera tripod. The high-resolution imaging capability is provided by epi-illumination of a flexible 1 mm diameter fiber-optic bundle, with the distal end of the fiber placed in contact with the tissue site to be imaged, following topical application of a fluorescent contrast agent. Fluorescent light emitted from the tissue returns through the same fiber and is imaged onto a high-sensitivity CCD camera [39]. This system was engineered into a lightweight (6 lb) and portable package (Figure 3-3b). Both the widefield imager and the high-resolution microendoscope systems connect to a single laptop computer via IEEE-1394 (Firewire) ports, enabling

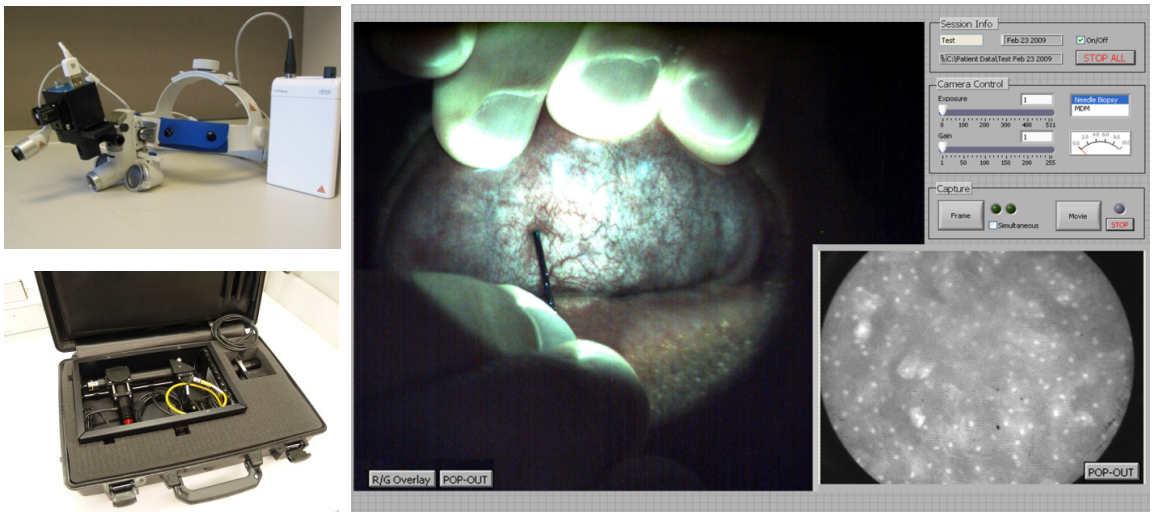

Figure 3-3: Combined portable widefield and high-resolution imaging systems. (A) The portable screening system weighs only 3 lb. (B) High-resolution microendoscope contained in a briefcase. (C) Widefield and high-resolution images of normal human oral mucosa acquired with the multimodal imaging system. In the widefield image (left frame), the green autofluorescence of normal tissue is apparent, as well as the microvascular network. The high-resolution fiber-optic probe can be seen in contact with the mucosal surface, approaching from the base of the widefield frame. The high-resolution image, acquired simultaneously, is displayed in the lower right frame, with the 800 μm diameter field-of-view corresponding to the tissue located beneath the tip of the fiber-optic probe. Following topical application of 0.05% proflavine solution to the probe tip, nuclei appear as discrete bright regions within each epithelial cell.

simultaneous imaging within a LabVIEW-based user interface (Figure 3-3c). The total cost of components for the combined imaging platform was under $10,000.

Figure 3-3c presents widefield and high-resolution images of normal human oral mucosa acquired with the multimodal imaging system. In the widefield image (left frame), the autofluorescence of normal tissue is apparent, as well as the microvascular network. The high-resolution fiber-optic probe can be seen in contact with the mucosal surface, approaching from the base of the widefield frame. The high-resolution image, acquired simultaneously, is displayed in the lower right frame, with the 800 μm diameter field-of-view corresponding to the tissue located beneath the tip of the fiber-optic probe. Following topical application of 0.05% proflavine solution to the probe tip, nuclei appear as discrete bright regions within each epithelial cell. The diagnostic performance of this integrated imaging system is currently being evaluated in pre-clinical studies, in comparison with research-grade optical imaging systems, and against the gold-standard of histopathology.

3.3. The Future of Optical Imaging for Global Cancer Management

Emerging clinical data suggest that optical imaging may play a key role in cancer management from two perspectives. First, optical methods can be used *in vivo* to acquire anatomical and functional images of tissue over a wide range of spatial scales, rapidly surveying large mucosal surfaces at risk to identify suspicious areas, and then interrogating those regions with sub-cellular spatial resolution. This capability offers practical flexibility in diagnostic use, enabling optical methods to be used in areas

ranging from early-stage screening, to supplementing histopathology. Second, technological advances made by the optoelectronics industry have produced high-performance components which can be used to build portable, cost-effective imaging devices. These features are necessary to support the sustainable dissemination of diagnostic imaging tools in remote areas and for traditionally underserved populations.

We contend that these advantages of optical imaging technologies can be used to impact cancer management in several practical ways. The availability of optical imaging devices has the potential to streamline medical procedures, provide guidance to biopsy sites, and expedite margin determination to help reduce procedure costs, and improve surgical outcomes. Cost-effective, portable devices such as the optical systems described here can potentially help fill crucial technological gaps in settings where the infrastructure to support traditional radiological imaging and pathology services available in industrialized countries, are neither available, nor affordable.

Potential Roles and Requirements for Optical Imaging

Expanding Access to Screening and Early Detection

Screening high risk populations and early detection of cancer are critical to prevention, effective treatment and decreased morbidity of several types of malignancies. In low- and medium-resource countries, cancers of the stomach, liver, oral cavity, and cervix are common. Changes in diet and smoking habits are leading to increases in cancers of the lung, breast, esophagus, prostate, and colon [40]. Optical imaging is most applicable to cancers that develop in epithelial mucosal surfaces, due to the limited penetration depth of light. Optical screening methods have been applied to and are

currently the subject of significant research efforts for cancers of the oral cavity, cervix, lung, ovary, breast, esophagus, urinary bladder, skin, and colon (11, 12, 14, 15, 16, 21, 28), and these technologies can potentially be translated to low-resource settings.

Without improved screening programs in these settings, it is likely that most of these cancer patients will continue to be diagnosed at late stages when limited treatment options exist. For instance, in Africa there is an overwhelming shortage of expertise for the operation and maintenance of medical equipment to deliver radiation therapy, and as a result, radiation treatment is only available to approximately 20% of the patients who need it [19]. Early diagnosis can reduce the burden on these limited resources by enabling simpler treatments to be provided for patients with early-stage disease. In this respect, cervical cancer screening can serve as a positive model for prioritizing early detection of other cancers in developing countries. It has been shown that screening women just once for cervical cancer and its precursors at age 35 can reduce the lifetime risk of developing cervical cancer by 25-36% [41]. When effective and economically viable treatment (cryosurgery in the case of cervical pre-cancer) can be administered, access to even minimal screening can clearly have a considerable benefit to an at-risk population.

Clinical studies using widefield optical imaging have shown that inexpensive optical systems can be used for early detection of cancer in the oral cavity, with the VELscope specifically targeting the dentist's office as a site for routine screening [37]. In low-resource settings where healthcare providers are unlikely to have specific expertise in cancer detection, it is particularly important to provide practitioners with objective tools to guide diagnosis. Most imaging devices require subjective evaluation,

but current research on image processing techniques enable optical devices with digital image capture to allow for objective assessment for pathologic abnormalities. For example, Roblyer *et al.* recently demonstrated a simple technique to detect and delineate oral neoplasia based on quantitative analysis of autofluorescence images [42]. In this study, autofluorescence images at 405 nm excitation were acquired with a color CCD camera. Using linear discriminant analysis, a classifier was developed to distinguish neoplastic and normal regions of interest based on the ratio of red-to-green pixel intensities, resulting in 100% sensitivity and 91.4% specificity in a validation set. Objective analysis techniques can provide a repeatable way to determine the threshold for demarcating suspicious lesions, while also lessening the need for extensive user training. In primary care settings, optical imaging devices could offer health care providers effective screening tools, which can assist in identification of cancer at the earliest stages. Indeed, maintaining and expanding access to early screening is becoming increasingly important given the growing shift of poor and underinsured people towards suburban and rural areas, away from major metropolitan areas where most healthcare services are concentrated [43].

Guiding Treatment through Real-Time Biopsy and Histology

Optical imaging technologies can also be used to help clinicians in low-resource areas to diagnose and treat early malignancies. When a suspicious lesion is identified, the current practice in most developed countries is to perform an invasive biopsy to obtain tissue for histopathologic analysis. The ability to perform a biopsy is crucial for accurate diagnosis, but requires considerable physical infrastructure, personnel, and economic

resources. High-resolution optical imaging can provide an alternative means of evaluating cellular morphology when histo- and cytopathology facilities are unavailable. Even in well-equipped centers, the ability of optical imaging to guide the clinician to sample the most appropriate sites may significantly reduce cost and improve the diagnostic value of biopsies obtained from the patient [44].

Although results from current optical imaging technologies are promising, there are still several hurdles to overcome before these devices can be translated into low-resource clinical settings. First, better needs assessment studies are required to more effectively delineate design requirements and guide the development of appropriate technology for use in developing countries. Such considerations include developing robust battery-powered devices for sites where electric power may be unreliable, designing devices which require minimal user expertise for settings where the availability of highly trained practitioners may be limited, and developing low-cost image contrast agents which can be stored safely for long periods in environments with potentially extreme temperatures and humidity levels. Quality control of devices is also important in the developing world, to ensure that instruments can remain calibrated and functional over time in settings without trained technicians. And finally, researchers and technology developers must overcome the relative lack of funding sources that enable non-profit and for-profit institutions to develop devices for low-resource settings and to carry out necessary field studies and translation of technology in the absence of traditional market incentives.

Cancer is projected to become the world's leading cause of death by 2030, with the burden of disease shifting further towards medically underserved populations in

industrialized countries and the developing world [26]. New approaches are required across the spectrum of cancer management, in prevention, diagnosis, treatment, education and care. If developed and tested appropriately, optical imaging technologies can play an important role in several aspects, from providing objective diagnostic screening at the community healthcare level, to enabling pathology guidance in the clinical setting. Importantly, by delivering these technical capabilities within cost-effective platforms, the impact on public health can be magnified through expanding patient access to previously unreachable healthcare systems.

Acknowledgements

This work was supported by National Institutes of Health Grants R01 EB007594, R01 CA103830, and R01 CA124319.

Chapter 4

Expanding the field-of-view of endomicroscopes: video mosaicing*

*The contents of this chapter are being prepared for submission as the following manuscript: N. Bedard, T. Quang, R. Richards-Kortum, and T. Tkaczyk, "Real-time in vivo video mosaicing with a high-resolution microendoscope," Biomed Opt Exp (2012).

As discussed in Chapter 3, microendoscopy allows clinicians to view *in vivo* subcellular features in real-time and can be used for applications such as biopsy screening, point-of-care diagnostics, and disease progression studies. Although microendoscopes have excellent image quality, their field-of-view is inherently limited by the small size of the distal end, which can make it difficult for the user to navigate the tissue and obtain an accurate diagnosis. Video mosaicing has emerged as an effective technique to increase the acquired image size, but most implementations are performed post-procedure, thus diminishing the benefit of real-time tissue examination. In this

chapter we present an algorithm for real-time video mosaicing using a portable low-cost high-resolution microendoscope. We present execution times for each stage of the algorithm and show results from *ex vivo* and *in vivo* tissue samples. Video mosaics are also compared to images from a benchtop confocal microscope as well as histopathology.

4.1. Introduction

Histopathological examination of excised tissue is the standard of care for the diagnosis of epithelial cancers. During this procedure pathologists examine cellular features such as nuclear size, nuclear-to-cytoplasmic ratio, and architectural alterations. Microendoscopy is a type of optical imaging that allows clinicians to view these features *in vivo* at subcellular resolution, effectively bringing the microscope to the patient. These non-invasive devices can (1) be used to screen biopsy sites in order to reduce the number of biopsies taken, (2) function as point-of-care diagnostic tools during surgical procedures, or (3) to monitor disease progression throughout longitudinal *in vivo* studies [45]. Although microendoscopes can have excellent resolution and light efficiency, their field-of-view (FOV) is inherently limited by the size of the probe's distal end. In most microendoscopes the FOV is < 1 mm^2, which is comparable to the field of a 40X microscope objective. This "tunnel vision" can make it difficult for users to obtain a broad sense of tissue morphology [46] and result in sampling error when imaging a heterogeneous tumor [47] .

Video mosaicing has been demonstrated as an effective tool for increasing the FOV acquired by microendoscopy. This technique stitches together consecutive video frames acquired as the probe is scanned over the tissue, thus creating a 2 – 30 times larger high-resolution image. Several papers have discussed development and clinical application of off-line video mosaicing using commercial confocal microendoscopes [48-50]. These methods combine the frames of a saved video using non-rigid deformation algorithms and template matching. Although these approaches can account for tissue stretching and motion artifacts, they are too computationally intensive for video-rate implementation and are carried out post-procedure. Therefore the clinician does not have the benefit of live evaluation of a large FOV. Another approach called real-time video mosaicing computes a simpler rigid registration in order to build the mosaic as each frame is acquired. This provides the user immediate feedback about broad tissue morphology, aids in maintaining probe stability, and helps create a better video for additional off-line processing. The concept was discussed for a commercial confocal system in proceedings [51] and was briefly mentioned in [52]. Unfortunately, neither of these publications provides a thorough description of a real-time video mosaicing algorithm.

In this chapter we present an algorithm and initial results for real-time *in vivo* video mosaicing. The technique is implemented on an inexpensive high-resolution microendoscope (HRME). Compared to commercial microendoscopes that can cost > $50,000, the HRME (< $5,000) enables access to a greater number of researchers and clinicians. The algorithm is a three step process that includes: fiber bundle pattern

removal, image registration, and insertion into a mosaic. Mosaic results are compared to benchtop confocal imaging as well as histopathology. To the best of our knowledge, this is the first publication to provide a complete description and histopathology comparison of real-time video mosaicing using a microendoscope.

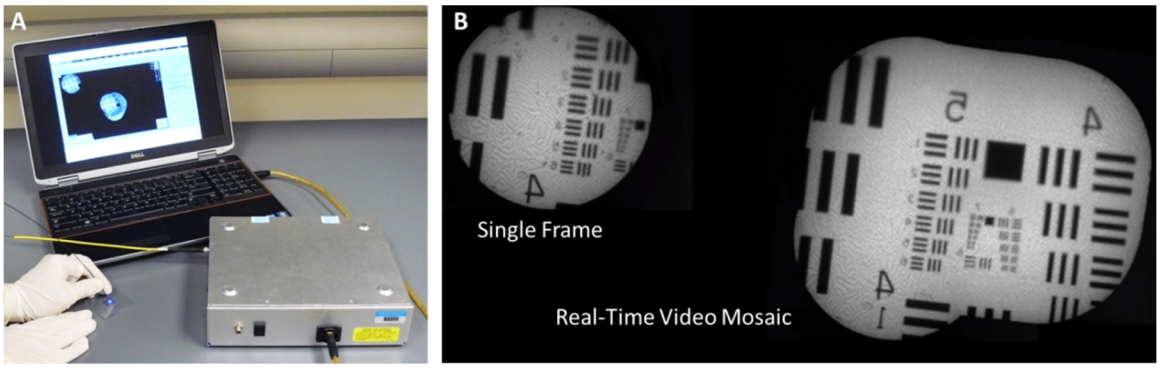

Figure 4-1: (A) The high-resolution microendoscope (HRME) is a portable fluorescence imaging device that provides in vivo subcellular detail with a field-of-view of <1 mm. (B) Real-time video mosaicing increases the field-of-view.

4.2. Methods

4.2.1. High-resolution microendoscope (HRME)

The system that we modified for real-time video mosaicing was previously used in several *in vivo* tissue studies [53, 54]. It is well-suited for animal experiments and clinical applications because it is small, portable, battery-powered, and interfaces with a standard laptop computer (see Figure 4-1A). Although the system is thoroughly described in [55], we provide a brief description of the device here.

The HRME is a widefield epi-fluorescence fiber-bundle microendoscope. It uses a 5W 455 nm light emitting diode (LED) and lenses to provide Koehler illumination at the proximal face of a 30,000-element coherent fiber bundle. The tissue at the distal end of the fiber bundle is labeled with the fluorescent dye proflavine, which binds to DNA and has a peak emission of 515 nm. Emitted light exiting the proximal end of the fiber bundle passes through a dichroic filter and a longpass filter. It is then imaged onto a CCD using a 10X objective and tube lens. Images are acquired at a rate of 11 frames per second (FPS) at 16-bit digitization. Camera settings, image display, and file saving are controlled with custom LabVIEW software. Figure 4-2 (left) shows a raw image of nonkeratinized stratified squamous epithelium acquired by the device. Nuclei appear as bright circles throughout the image and individual fibers within the fiber bundle can be seen.

4.2.2. Fiber pattern rejection

The first step to implement video mosaicing is to remove the fiber bundle pattern from HRME images. This is necessary because the fixed spatial frequencies produced by the bundle structure hinder the subsequent image registration algorithm. For real-time video mosaicing a fast, accurate, and memory efficient method is necessary. Ideally, this step should run much faster than the HRME's nominal operational speed of 11 FPS. A few publications discuss methods to remove the bundle pattern while preserving image content, including: spectral filtering in the frequency domain [56], median filtering in the spatial domain [57], or spatial interpolation [58]. We developed a custom spatial interpolation algorithm because none of these methods were tailored for real-time

execution. Based on the nearest-neighbor lookup table method suggested in [58], our approach (1) preserves all intensity information of the sample image and (2) requires minimal computation time and memory.

The nearest-neighbor interpolation algorithm reconstructs an image based on pixel intensities at regional maxima. As shown in Figure 4-2 (right, "Raw Image"), fiber cores appear as regional maxima within the images due to the Gaussian intensity profile that they create on the detector. The pixel values at the center of these regional maxima best represent the intensity of the underlying object; therefore we use only these values to reconstruct a fiber-less image. First, fiber center pixels **f** are determined using the Matlab regional maxima function *imregionalmax.m* described in [59] (see Figure 4-2 "Fiber Locations"). Next, for each image pixel location $\mathbf{p} = (x_p, y_p)$, an enclosing triangle of fibers cores **f** is defined as $\mathbf{f}_i = (x_i, y_i),\ i = 1, 2, 3$ with distances $d(\mathbf{f}_i)$ [58]:

$$\begin{pmatrix} d(\mathbf{f_1}) \\ d(\mathbf{f_2}) \\ d(\mathbf{f_3}) \end{pmatrix} = \begin{pmatrix} x_1 & x_2 & x_3 \\ y_1 & y_2 & y_3 \\ 1 & 1 & 1 \end{pmatrix}^{-1} \begin{pmatrix} x_p \\ y_p \\ 1 \end{pmatrix} . \quad (1)$$

The intensity of **p** is then chosen by selecting the nearest fiber $\mathbf{f_n}$:

$$I(\mathbf{p}) = I(\mathbf{f_n}) . \quad (2)$$

The Matlab functions *griddata.m* and *TriScatteredInterp.m* are used to compute the Voronoi tessellation (see Figure 4-2 "Nearest-Neighbor Tessellation"). For real-time implementation, we assume that the fiber bundle pattern remains fixed within a sequence of images. Therefore, the tessellation is computed only once at the beginning of the procedure to determine a lookup table of fiber core reference coordinates. The lookup

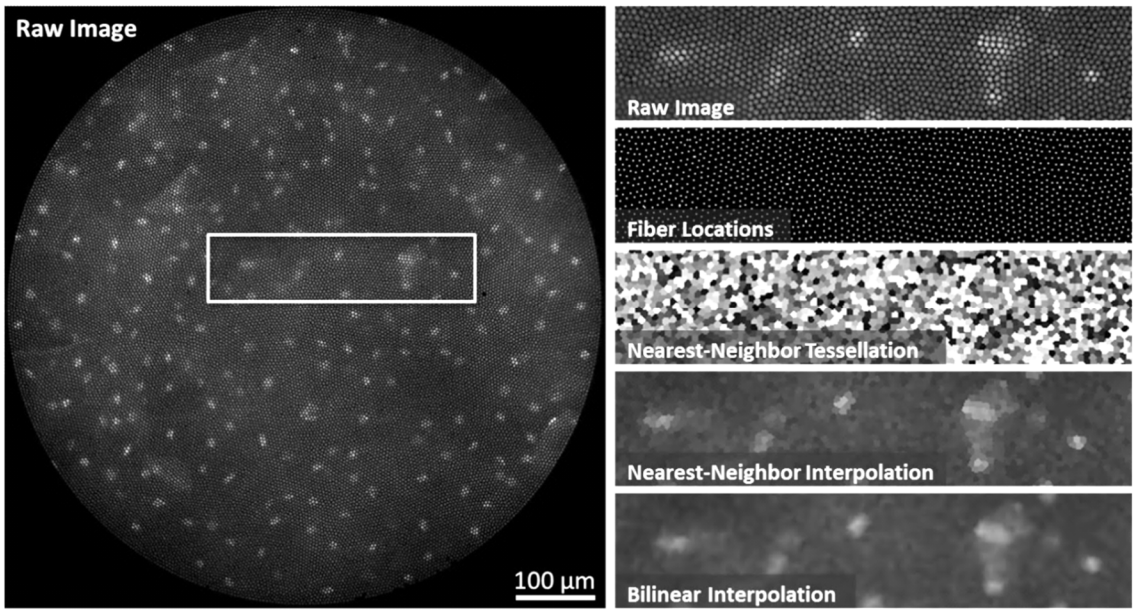

Figure 4-2: Fiber pattern removal. (Left) The raw HRME image shows squamous epithelial cells in the oral cavity. Nuclei are labeled with 0.01% Proflavine. The intensity information from the sample is "pixelated" by the 30,000-element fiber bundle. (Right) The fiber pixelation pattern is removed using two-dimensional interpolation. First, the fiber center locations are identified using a regional maxima function. A Voronoi tessellation is then constructed from these points in order to determine the nearest-neighbor fiber pixel for every non-fiber pixel. A lookup table is determined from this tessellation and is used to reconstruct fiber-less HRME images in real-time. Other interpolation methods, such as bilinear interpolation, can be used but have longer computation times.

table is calculated from an image of a uniform fluorescent slide (Fluor-Ref Green, Ted Pella). Subsequent HRME image are then divided by this "calibration" image to normalize the fiber bundle intensity response. In addition, given that fibers are spaced approximately 5 pixels apart, we found that downsampling the lookup table by a factor of 2 – 3 also reduces processing time while maintaining image quality. Applying the lookup table to raw a 1.3 megapixel HRME image takes 0.8 ms on our laptop computer (Intel i7-2720QM), as shown in Table 1. The interpolated and downsampled result is

approximately 375 x 375 pixels. Figure 4-2 (“Nearest-Neighbor Interpolation”) shows our fast interpolation method removes the fiber pattern while preserving image edges and contrast.

4.2.3. Frame registration

The registration algorithm determines the best translational offset between two consecutive video frames and calculates an error for their fit. Before registration, a rectangular region of interest is cropped from the circular FOV of processed HRME images. This prevents registration errors caused by fiber bundle edges. Time and memory constraints for registration are the same as for the interpolation algorithm. For this reason, we chose to implement the fast registration algorithm presented in [60], which performs an optimized cross correlation using discrete Fourier transforms (DFTs). The cross correlation of two images *f(x,y)* and *g(x,y)* is given by:

$$r_{fg}(x_i, y_i) = \sum_{u,v} F(u,v)G^*(u,v)exp\left[i2\pi\left(\frac{ux_i}{M} + \frac{vy_i}{N}\right)\right], \qquad (3)$$

where N and M are the image dimensions, uppercase letters represent the DFT, and (*) denotes complex conjugation. The approach to finding the cross-correlation peak is to (i) compute the product *F(u,v)G*(u,v)*, (ii) take the inverse FFT to obtain the cross correlation, and (iii) locate its peak [60]. Error of registration fit is given by the normalized root-mean-square error (NRMSE). On average we found the registration algorithm is executed in 12.2 ms (see Table 1).

4.2.4. Frame insertion

Registered HRME frames are inserted into a large zero-value image called a canvas. The canvas size is selected by the user and is typically 1 to 7 MP, which is 7 to 50 times larger than a downsampled HRME frame. The first frame in a video sequence is copied to the center of the canvas. Subsequent frames are inserted into the canvas at an offset determined by the registration algorithm. We tested two real-time insertion strategies: (i) pixel maxima and (ii) dead leaves.

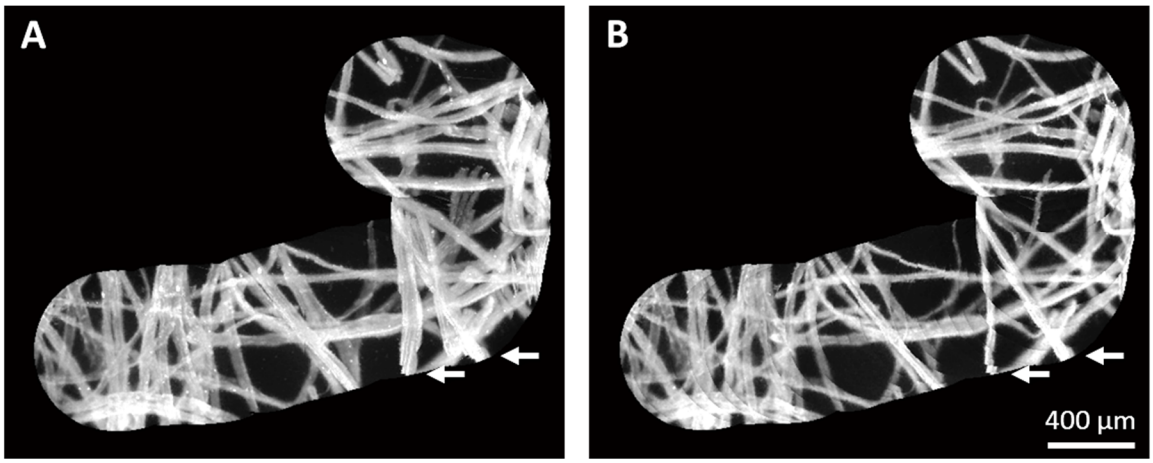

Figure 4-3: The HRME was translated over fluorescently-labeled lens paper to build a mosaic. (A) When video frames are inserted into the mosaic using the pixel maxima approach, frame boundaries are smooth, but disturbed fibers appear blurred as shown by the arrows. (B) When the dead leaves approach is used, blurring does not occur, but frame boundaries can become noticeable. The dead leaves approach is preferred for tissue imaging because probe movement significantly deforms the tissue.

The pixel maxima approach inserts the maximum intensity value for each overlapping pixel of the newest frame and current mosaic. This strategy works well for more rigid tissue such as epidermis, but results in a motion-blurred mosaic when used on

deformable tissue or targets with free-moving debris. For our application it is important to preserve size and separation of features such as nuclei, so we typically use the dead leaves approach [51], which simply replaces overlapping regions with the new frame. Figure 4-3 shows mosaicing results from fluorescently-labeled lens paper using each of these techniques. Although individual frame boundaries can become apparent when using the dead leaves approach, spatial features within the image maintain their size. To reduce frame boundary visibility when the probe is moving slowly, we only insert frames that have moved at least one tenth of a FOV from the last inserted frame.

4.2.5. Error handling and file saving

Registration errors can occur for several reasons. First, registration errors can result from motion blurred images. This is prevented by selecting a low camera exposure (< 10 ms) and by translating the probe slowly across the tissue. Slow translation also ensures that consecutive frames have overlapping spatial features to register. We found registration works well when consecutive frames have at least 75 percent overlap, which corresponds to a maximum velocity of 2.75 mm/s for a 1 mm HRME probe imaging at 11 FPS. Registration errors can also occur when there is little spatial information (such as in uniform gray images) or when there is loose debris. The NRMSE is used to determine if a registration has occurred. Frames with NRMSE error above 0.5 were considered misregistered. In general, we often found that small spatial discontinuities from misregistered frames did not significantly degrade the overall quality of the mosaic (see Figure 4-4D). Therefore, instead of restarting the mosaic after a registration error, the

misregistered frames can alternatively be highlighted and inserted into the current mosaic. As an indicator of the probe moving too quickly, we also chose to highlight frames that overlap less than 75% with the previous frame.

Although the canvas is displayed in real-time, it is impractical to save every frame of the reconstructed mosaic because of the large canvas size. Instead, we allow the user to save snapshots of the mosaic or save a movie of the raw camera data. Mosaic snapshots are saved as 16-bit .png images and movies are saved as two 8-bit .avi videos, which contain the high and low bits of 16-bit frames.

4.3. Results

All steps of the video mosaicing procedure were implemented and benchmarked in a real-time LabVIEW graphical user interface (GUI) on a standard laptop computer (Intel i7-2720QM). A summary of the computational time requirements for our real-time video mosaicing algorithm is shown in Table 4-1. The first row shows the execution time with no mosaicing, which represents time to read the image buffer and display the image. Times for fiber rejection and frame registration remain constant because these are only dependent on the raw image size. However, frame insertion time is dependent on the total empty mosaic size; therefore, the results are shown for several canvas sizes. In all cases the execution time of the mosaicing GUI is faster than the frame rate of the camera (which has a maximum speed of 11 FPS or 91 ms/frame).

Table 4-1: Time requirements for the video mosaicing algorithm.

Mosaic Size (pixels)	Fiber Pattern Rejection (ms)	Frame Registration (ms)	Frame Insertion (ms)	Total, incl. all GUI functions (ms)
No Mosaicing	-	-	-	49.5
1120 x 770	1.9	18.1	9.2	64.5
1600 x 1100	1.9	18.1	10.6	65.8
2080 x 1430	1.9	18.1	12.3	66.5
2400 x 1650	1.9	18.1	13.3	67.5
3200 x 2200	1.9	18.1	17.1	71.4

Real-time video mosaicing was tested on several *ex vivo* and *in vivo* tissue specimens. All data collection followed IRB approved protocols (Rice University 11-119E and MD Anderson Cancer Center PA11-0570). Figure 4-4 shows video mosaics obtained *in vivo* from the (A) lower lip and (B) skin of a normal volunteer, which demonstrates the algorithm performs well on different cell types. In these examples video mosaicing increased the FOV 3-10 times. Our microendoscopy mosaicing results reveal similar morphological features, such as hair strands and keratin sheaths, as a skin mosaic obtained from a commercial benchtop confocal microscope (Figure 4-4C). In Figure 4-4D we present video mosaicing results from an *ex vivo* cervical "loop electrosurgical excision procedure" (LEEP) specimen. The HRME probe was scanned from normal squamous tissue to abnormal columnar tissue (shown by the white arrow), which in this case represents the border of diseased tissue. Determining this boundary is more difficult with the limited FOV of a single HRME frame, but is clearly defined in the mosaic result. Figure 4-4E shows a histology section from the same boundary region. Throughout

imaging experiments real-time mosaicing provided immediate feedback about probe stability and velocity, which is important when additional offline processing is desired.

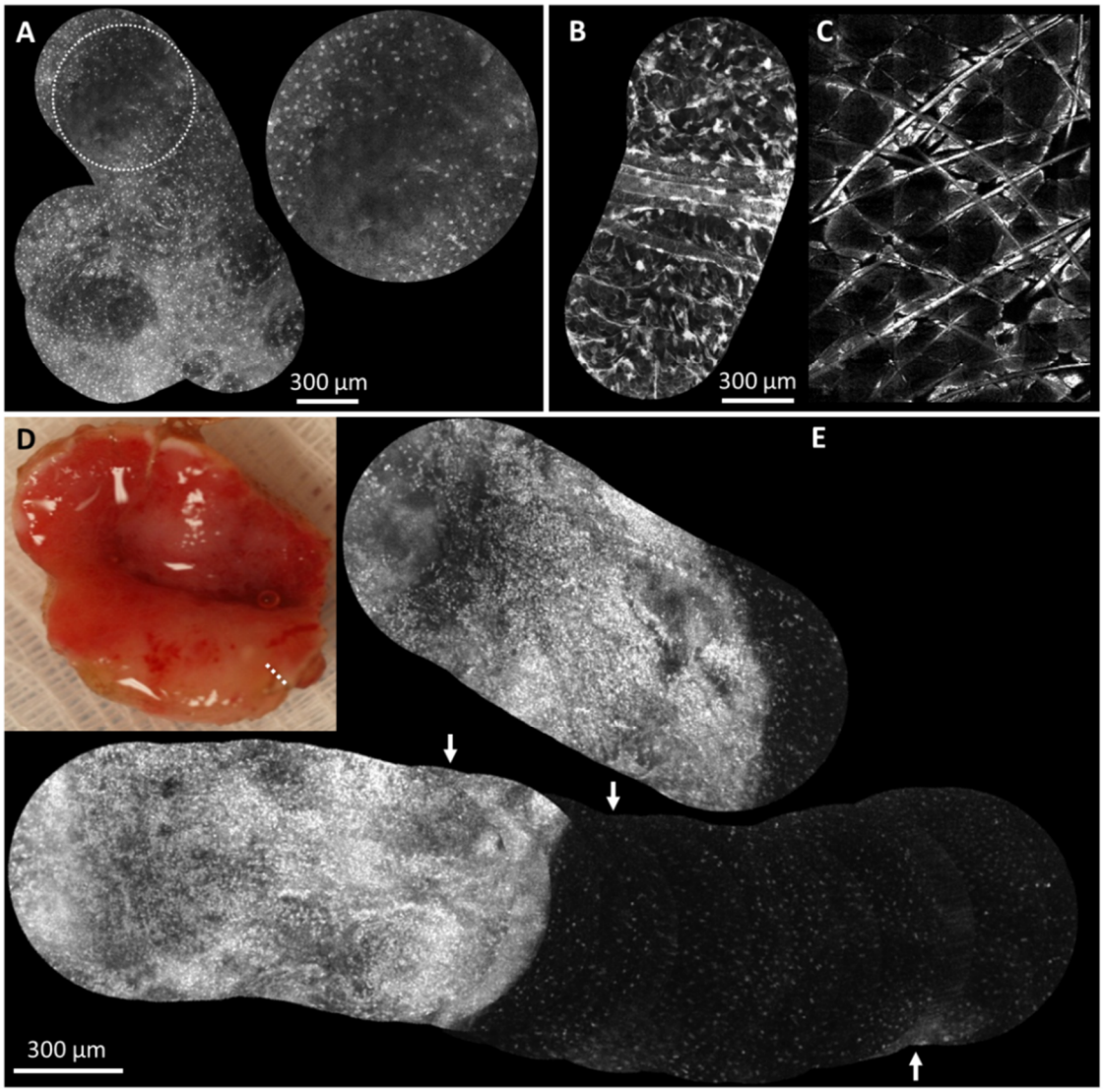

Figure 4-4: Real-time video mosaics from (A) normal in vivo oral tissue, (B) normal in vivo epidermis, and (D) cancerous ex vivo cervical tissue. These results show that the algorithm correctly aligns and combines morphological features of several cells types and anatomical locations. In (A) the distribution of normal squamous epithelial cells is seen in the gingiva and in (B) features such as hair and keratin sheaths are visible. An image mosaic (C) from a benchtop confocal microscope obtained during the same imaging session reveals similar morphologic features as (B). The normal/abnormal junction of ex vivo cervical tissue is shown (D), where the white dotted line indicates the path of two mosaics. The bottom mosaic in (D) shows that it can be useful to display a large mosaic even with several misregistered/blurred frames (white arrows). Histopathology for the cervical tissue normal/abnormal junction is shown in (E).

4.4. Discussion

In this chapter we describe a complete algorithm for real-time video mosaicing using a portable low-cost high-resolution microendoscope. The algorithm is executed on the laptop computer's CPU well within the nominal frame rate of the camera. Speed could be further improved with the use of GPU programming, which can take advantage of parallel architecture and massive multithreaded data processing. While our technique provides accurate mosaics in many imaging applications, as shown with *ex vivo* and *in vivo* samples, there are several inherent limitations to the technique. There must be (1) spatial features within consecutive images, (2) spatial overlap between consecutive images, (3) minimal free-moving debris, and (4) minimal tissue deformation. These requirements could be prohibitive for some endoscopic cases, such as deep tissue where it may be difficult to slide the probe across the tissue or locations with significant debris.

The solution to these limitations could be to use a two-step mosaicing strategy which involves (1) real-time mosaicing for live image acquisition and (2) post-procedural mosaicing for higher accuracy reconstruction. With post-procedural mosaicing there is no strict time requirement, which allows for techniques such as non-rigid image registration and template matching. These algorithms can overcome the limitations of real-time mosaicing because they can selectively ignore potential debris, deform images before registration, register images based on their best fit within an entire mosaic, and blend overlapping images.

Our current work on video mosaicing provides a live picture of broad tissue morphology (> 5 mm^2) using a < 1 mm diameter microendoscope probe. Future work aims to implement post-procedural mosaicing with the HRME and to develop algorithms to automatically quantify features such as nuclear-to-cytoplasmic ratio and nuclei spacing within mosaics. These new techniques will then be used to test the diagnostic value of HRME video mosaicing for several cancer types in multi-center clinical trials.

Acknowledgements

This work was supported by R01A124319 and R01EB007594.

Chapter 5

Increasing lateral resolution of endomicroscopes: snapshot spectrally encoded fluorescence imaging*

*The contents of this chapter were submitted to a journal as the following manuscript: N. Bedard, and T. Tkaczyk, "Snapshot spectrally encoded fluorescence imaging through a fiber bundle endomicroscope," Journal of biomedical optics (2012).

Another drawback of current configurations for endomicroscopes is that they have either limited spatial resolution or require a scanning mechanism at the distal end of the fiber, which can slow imaging speed and increase the probe size. We present a novel configuration that provides high contrast 350 x 350 pixel images at 7.2 frames per

second, without the need for mechanical scanning at the proximal or distal end of the fiber. The device is tested in fluorescence mode and can resolve 1.5 μm features of a high-resolution 1951 USAF target.

5.1. Introduction

Endomicroscopy is an important tool for minimally invasive diagnosis and surgery as well as *in vivo* cellular research in animal models. Small and flexible fiber optic endomicroscopes with < 1 mm outer diameter have been built by utilizing optical fibers that transmit an image to a light detector outside of the body. Although fibers enable a small distal probe size and microscopic field-of-view, the image quality and/or frame rate is reduced as a consequence of the fiber-dependent optical system.

Several configurations for fiber optic endomicroscopes have been shown [45]. A common implementation uses a coherent bundle of optical fibers as an image guide. Some confocal and multi-photon fiber bundle systems illuminate one fiber at a time with a pair of raster-scanning mirrors while a point-detector such as a photo-multiplier tube (PMT) detects returning light [61-63]. Alternatively, a two-dimensional detector array can be used to capture an image in a single exposure. This configuration can have reduced cost, size, and optical complexity [53, 54]. In addition, it can take advantage of modern scientific-grade camera technologies such as sCMOS, EMCCD, or back-thinned sensors that provide higher speed, greater quantum efficiency, lower noise, and more sampling than with a scanning-type system [64]. When using a fiber bundle, however, the

quantity of optical fibers that can be packed into the bundle (usually ~5000 to 30,000 fibers) limits the number of spatial samples, and therefore limits the resolution of images being displayed [65].

Some endomicroscopes avoid this limitation by using a single optical fiber coupled to a two-axis mechanical scanner at the sample plane. High-speed scanning systems are difficult to miniaturize, therefore these systems sacrifice frame rate and probe size for improved image quality [66, 67]. Another single fiber technique, known as spectrally encoded endoscopy (SEE), replaces mechanical scanning in one dimension with a prism and a broadband light source in order to create a line of spectrally dispersed light on the sample [68, 69]. Spectrally encoded spatial information can be detected with a line-spectrometer at the proximal end of the fiber, which reduces the size and complexity of the distal system. The technology, however, still requires one axis of mechanical scanning and is difficult to implement in fluorescence imaging mode due to the Stokes shift of fluorescent contrast agents [70].

In this chapter, we present a novel endomicroscope configuration that combines the benefits of using a fiber bundle with the increased sampling of spectral encoding. To the best of our knowledge, this is the first demonstration of increasing lateral resolution in a fiber bundle endomicroscope without the need for moving parts in the system. The configuration is well suited for miniaturization because no electronics or mechanics are required at the distal end.

5.2. Methods

The concept that we call snapshot spectrally encoded endomicroscopy (SSEE) is illustrated in a fluorescence imaging configuration in Figure 5-1A. The setup uses an optical system at the distal end of the *N*-element fiber bundle in order to sample the fluorescent object at different spatial offsets. Figure 5-1B shows spatial offsets are from lateral chromatic shift induced by dispersion of a prism. The fiber bundle samples the dispersed image at spatial offsets that correspond to different emission wavelengths. Once spatial information is spectrally encoded into the fiber bundle, a hyperspectral camera captures the offset spectral images at the proximal bundle face. Spectral images are combined into a single high-resolution image using a custom reconstruction algorithm. This series of steps registers the spectral images that have been offset by dispersion, determines the intensity information contained at each fiber core within the spectral images, and then combines all of the sampling information into a single image. The algorithm includes (1) fiber bundle pattern removal (2) image registration and (3) combination of spectral images. Using this reconstruction procedure, the *N* spatial samples from each of the *M* spectral image are combined into a single image with *N* x *M* spatial samples (see Figure 5-2). The increase in sampling improves the image resolution without the need for any scanning mechanism in the system.

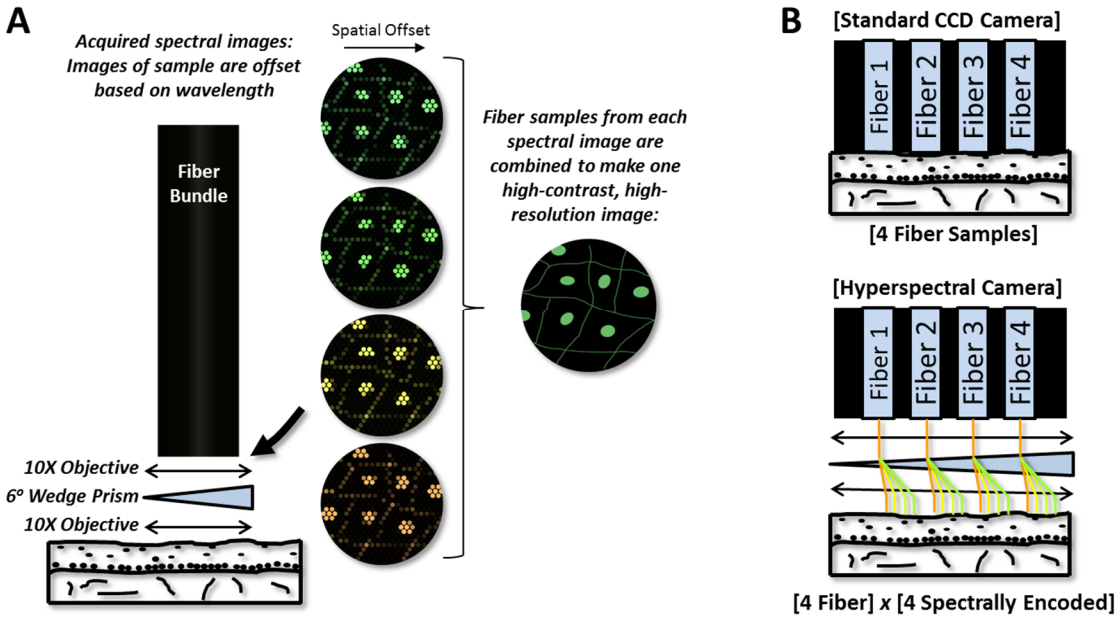

Figure 5-1: Snapshot spectrally encoded endoscopy concept. (A) A prism and lenses are attached to the distal end of a coherent fiber bundle. The image of the sample is dispersed over the face of the bundle, which causes the discrete fibers to sample the image at slightly different offsets. Using a reconstruction algorithm, the fiber samples from each wavelength are combined to produce one image with higher contrast and resolution. (B) In a traditional fiber bundle imaging system, the number of spatial samples is limited by the amount of fibers within the bundle. Our configuration uses dispersion to overcome this sampling limitation. A hyperspectral camera captures the encoded images.

Our previous studies used a traditional fiber bundle endomicroscope configuration to detect size and distribution of cell nuclei within potentially cancerous tissue [53, 54]. In the proof-of-concept system presented here, we aimed to improve visibility of subcellular features using snapshot spectral encoding. The fluorophore proflavine is used to stain nuclei and has an emission full-width half-maximum (FWHM) over the range 515 – 570 nm. In order to increase fiber bundle sampling of the fluorescent object, we chose to match the dispersion range of the emission spectrum to a distance comparable to

the fiber spacing (see Figure 5-1B). This was achieved with two infinity-corrected 10X Olympus objectives mounted in an afocal 4-f imaging configuration with a 6^{o} wedge prism placed in between. Excitation and emission light were separated with a FITC filter set. The system also included a Mercury arc lamp that delivered excitation light through the 6,000-element S-Type Fujikura fiber bundle. A snapshot hyperspectral camera called the Image Mapping Spectrometer (IMS) was used for image detection [71]. This detector was selected because it collects all spatial-spectral information in a single camera exposure and has high light efficiency; therefore it can detect low fluorescence signals and does not suffer from motion artifacts of scanning-type hyperspectral cameras. It has also been used in other endoscope configurations [72]. The IMS acquires 350 x 350 spatial x 20 spectral samples within the range 515 – 570 nm, at 7.2 frames per second (FPS) and 12-bit digitization. Thus, datacubes contain ~6,000 fiber x 20 spectral-encoded measurements, which correspond to 120,000 unique spatial samples; this improvement in sampling is comparable to increasing a 70 x 70 pixel image to a 346 x 346 pixel image.

The system is calibrated with a high-resolution 1951 USAF resolution target (Edmund Optics) backed with a Fluor-Ref green fluorescent slide (Ted Pella). After recording a datacube of the resolution target, the calibration starts by removing the fiber bundle pattern from each spectral image. This step is required because the fiber bundle pattern would otherwise interfere with registration of spectral images. The pattern is removed by implementing the interpolation method described in [58]. This method first identifies the pixel at the center of each fiber core, because these pixels best represent intensity values from the object. Pixel locations are determined using the Matlab regional

maxima function *imregionalmax.m* described in [59]. Next, pixels around identified fiber cores are filled using a fast two-dimensional linear interpolation [58]. The result of interpolation for one spectral image is shown within Figure 5-2A.

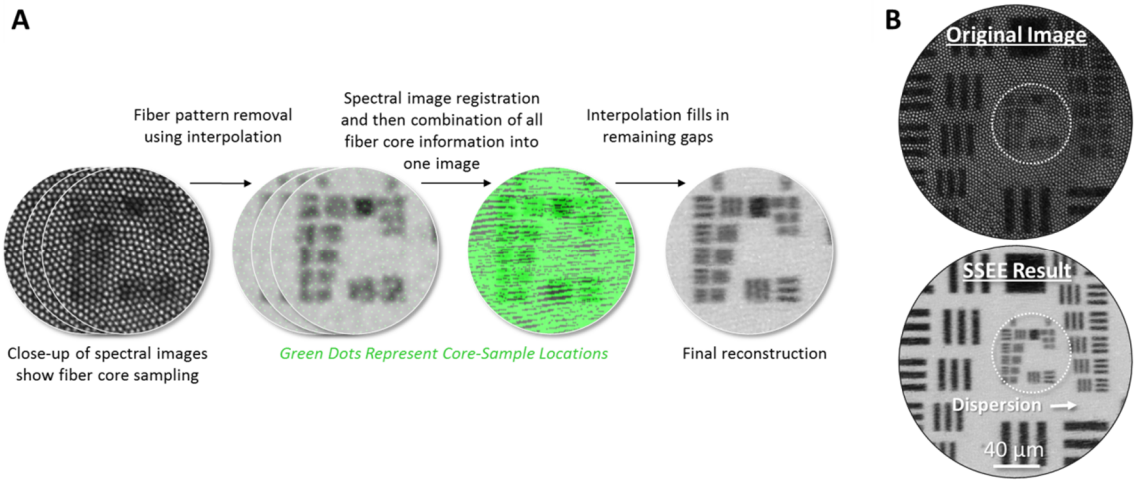

Figure 5-2: SSEE calibration procedure. (A) A datacube of a high resolution 1951 USAF target is acquired. The fiber bundle pattern is removed from each spectral image using interpolation based on fiber core centers. Spectral images are then registered. All spectral images are combined by taking the maximum fiber core intensity at each image coordinate. Effectively, void spaces between fibers in one spectral image are filled with fiber core intensity from other spectral images. Any remaining void spaces are filled with interpolation. (B) The results of SSEE show improved resolution and contrast compared to a fiber bundle image without spectral encoding.

Interpolated spectral images are then registered. The purpose of registration is to determine the horizontal and vertical subpixel spatial offset of each spectral image. The magnitude/direction is dependent on the dispersion introduced by the prism. Images with fiber pattern removed are intensity normalized and then registered with the FFT

algorithm described in [60]. Next, core locations from each coregistered spectral image are combined into a single image. This process essentially fills void spaces between fibers core in an image with information from fiber cores of other spectral images. Intensity values at all core locations are combined using a maxima function,

$$I_{all}(\mathbf{p}) = max\{ I_{\lambda=1}(\mathbf{f}), I_{\lambda=2}(\mathbf{f}), \ldots , I_{\lambda=M}(\mathbf{f})\} \ . \qquad (1)$$

where I_{all} is the image containing all fiber core information from M spectral images I_{λ}. Finally, any remaining void space is filled using the previously described interpolation method.

5.3. Results

Figure 5-2B shows the SSEE calibration result compared to the fiber bundle endomicroscope with no spectral encoding. An increase in resolution is apparent from the zoomed sections. Group 8 Element 3 (1.5 μm/line) can be partially resolved for the SSEE result, whereas the bundle system with no spectral encoding resolves up to Group 7 Element 3 lines (3.1 μm/line). The SSEE image also has increased contrast. The achievable resolution is dependent on the performance of the distal optics, the pseudo-regular spacing of fibers within the bundle, the reconstruction algorithm, and the pixel quantity on the detector.

After the calibration, all subsequent spectral images taken with the SSEE are combined using the same fiber locations and spatial offsets determined in the calibration procedure. Figure 5-3 shows images of (A) lens paper and (B) *in vivo* epithelial cells from the lower lip of a normal volunteer acquired at 7.2 FPS, with and without snapshot spectral encoding. SSEE images contain higher contrast, and details such as nuclear shape and cell membranes are more clearly visualized.

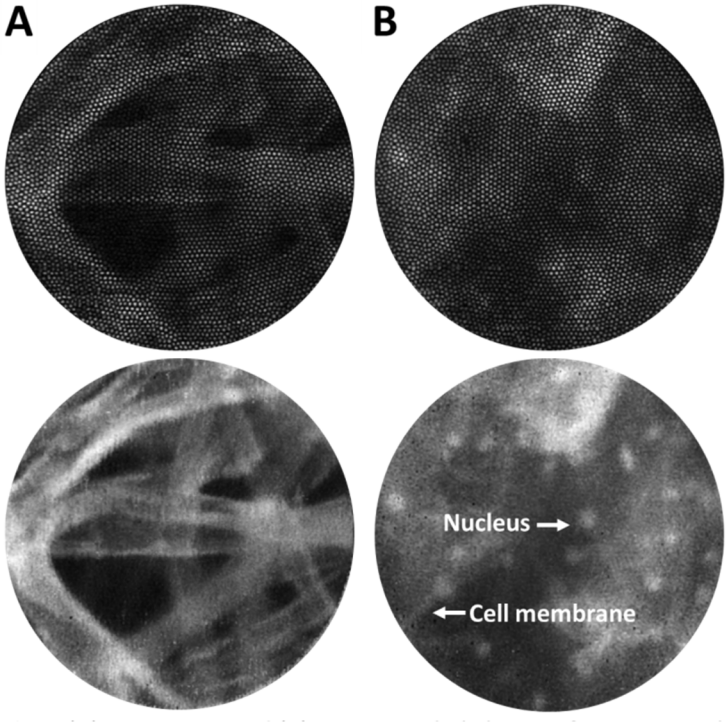

Figure 5-3: (A) Lens paper and (B) *in vivo* epithelial tissue from a normal volunteer's lower lip stained with proflavine. Snapshot spectrally encoded images have higher contrast and resolution, which increases visibility of details such as cell nuclei and membranes.

5.4. Discussion

This report describes a novel configuration for a microendoscope device that can be used to obtain high quality images with no scanning mechanism required at the proximal or distal end. Implementation of the modality has only recently become possible

due to advances in real-time, high-throughput snapshot hyper- and multi-spectral imaging technology. Other distal optics with different types of lateral chromatic distortion can be used to offset spatial sampling, such as holographic diffraction gratings, or GRIN lenses that have inherent radial lateral chromatic aberration [73]. Future work aims to improve imaging performance and decrease the size of distal optics using in-house techniques for fabricating miniature optics [74].

Acknowledgements

This work was supported by R01A124319.

Chapter 6

Improving depth-sectioning and background rejection of endomicroscopes: confocal and structured illumination

As shown in Chapters 3, 4 and 5, microendoscopes allow clinicians to view *in vivo* subcellular features in real-time, which can enable point-of-care diagnosis of dysplasia and cancer. While imaging studies have shown high sensitivity for diagnosing epithelial cancers, there are some tissue sites and conditions where it is difficult to visualize and quantify diagnostic features. In these cases a device with axial response of < 50 μm is typically needed to view features obscured by tissue debris and/or reject out-of-focus background signal. Commercial confocal microendoscopes with excellent axial response are available, but are often cost-prohibitive for many researchers and clinicians.

In this chapter, we present two low-cost (< $10,000), compact, and user-friendly endomicroscope systems with < 50 µm axial response. These devices also serve as a platform for our custom high-NA microendoscope objectives, which provide greater lateral resolution and the ability to image beneath the tissue surface.

6.1. Introduction

Microendoscopes allow clinicians to view *in vivo* subcellular features in real-time, which can enable point-of-care cancer detection of dysplasia and cancer [45]. In our research setting, we use a device called the High Resolution Microendoscope (HRME) to inspect epithelial tissues for precancer. The HRME is a fluorescence imaging device that uses the contrast agent proflavine to label DNA molecules [53, 55]. When acquiring images of stained epithelial tissue, proflavine causes nuclei to appear as bright circles throughout the field-of-view (FOV). Using imaging processing algorithms, we can quantify features such as nuclear-to-cytoplasmic ratio and nuclear separation in order to estimate disease probability. While studies have shown the HRME's ability to detect oral epithelial cancers [54], there are some tissue sites and conditions where it is difficult to visualize and quantify nuclear features.

The HRME has been proven as an effective tool for detecting epithelial cancers in the oral cavity, because several conditions are met: (1) most tissue is non-keratinized; (2) the stratified squamous epithelium cell type contains relatively large nuclei; and (3) proflavine is lightly sprayed or swabbed onto the tissue. However, the HRME does not

perform as well in other conditions. For example, it cannot accurately diagnose highly keratinized tissue because keratinocytes nonspecifically uptake proflavine. Fluorescing keratin sheaths often saturate the detector and prevent imaging of underlying nucleated cells, which makes it difficult to quantify nuclear features indicative of cancer. In tissue types other than stratified squamous epithelium, such as glandular epithelium, cells can become smaller and more crowded. Sometimes the cells become smaller than the HRME can laterally resolve; or they can become crowded in the axial direction, which increases background and reduces image contrast. These effects make it difficult to quantify nuclear features. Finally, in many *ex vivo* imaging protocols, the tissue is submerged in proflavine rather than sprayed/swabbed. While this procedure is intended to provide uniform labeling for supplemental widefield imaging, it has the consequence of adding significant fluorescent background to HRME images. Overall, there are several circumstances where bright features in the foreground (keratin) or background (cells or excess proflavine) prevent successful quantification of nuclear features within HRME images.

In this chapter, we present strategies to address current imaging limitations. We describe and implement two HRME modifications to improve depth sectioning, contrast, and background rejection. In order to facilitate translation into clinical studies, the solutions are compact, low-cost and user-friendly. Results for the original HRME system and our modified systems are compared with standard testing targets as well as *ex vivo* and *in vivo* specimens. Finally, we use these devices to image with a custom high-NA microendoscope objective.

6.2. Methods

Our solution to decrease unwanted foreground/background signal in HRME images is to improve axial response. Axial response is a measure of both axial resolution and the ability to reject light from outside the focal plane. A system with small axial response is able to reject fluorescence emitted from out-of-focus planes, which effectively decreases background and increases contrast when imaging thick specimens. Additionally, small axial response allows a microendoscope to image axial sections beneath the tissue surface, also known as depth sectioning. The current HRME system has an axial response of several millimeters because there is no mechanism for depth sectioning. Our previous studies have shown the ideal axial response for imaging glandular tissue is < 30 µm. Another study showed that a single axial section 50 µm below the tissue surface can be used to delineate normal, dysplastic, and cancerous tissue [75]. In this section we describe two modalities that are used to improve axial response in our endomicroscope studies: structured illumination (SI) and confocal microscopy. We provide the background for each of these techniques as well as details of our implementation.

6.2.1. Confocal HRME

Confocal microscopy is a common technique used to collect thin optical sections of a tissue sample. It works by scanning a diffraction-limited point of light throughout the focal plane of the sample, while detecting returning light through a pinhole aperture

placed at a conjugate image plane [62]. This method blocks out-of-focus light and can have axial response < 1 µm. Instead of using an LED and CCD detector as in the HRME, it requires mechanical scanners, a coherent laser source, and a high speed point-detector such as a photomultiplier tube (PMT). Although confocal endomicroscopy has been demonstrated on several fiber-bundle systems with promising clinical results [48, 61, 62], current commercial systems are often too expensive for many researchers and clinicians. In this work we developed a confocal fluorescence fiber bundle endomicroscope that is compact, low-cost, and user-friendly.

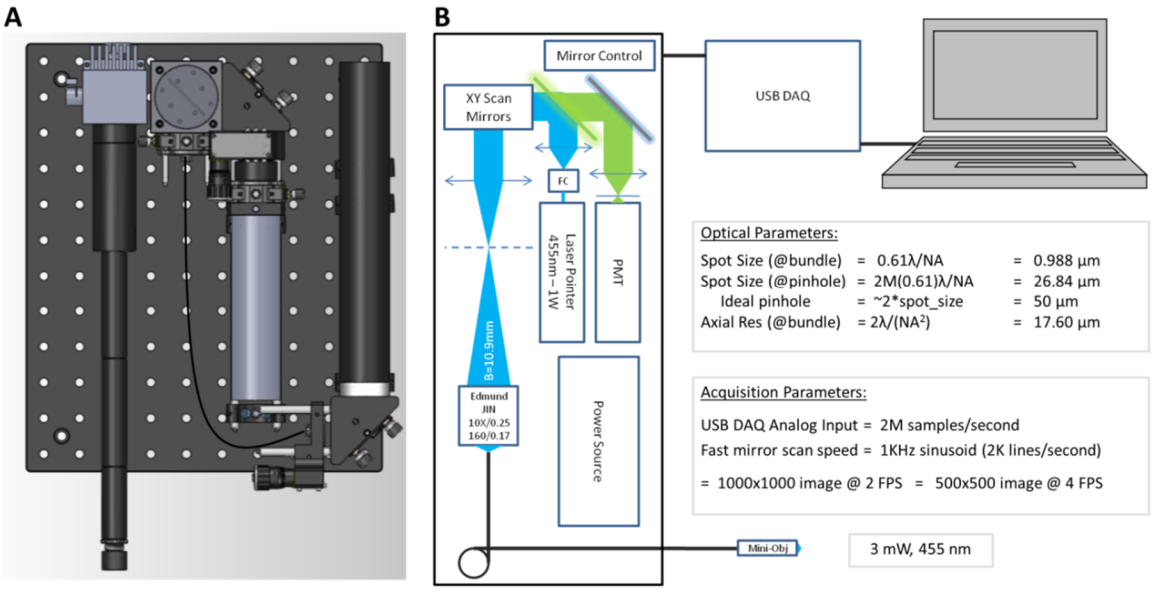

Figure 6-1: A drawing of the confocal HRME is shown in (A). A schematic of the device as well as optical/acquisition calculations are shown in (B).

We were able to create a compact low-cost device, comparable to the current HRME systems by: (1) creating custom-designed plastic optomechanics with the use of a

rapid prototyping machine, (2) using consumer grade optics, (3) using miniature scanning galvanometer mirrors, (4) utilizing a high-power handheld laser pointer, and (5) synchronizing all hardware/signal control with a USB device. The cost of the complete system is less than $10,000. Figure 6-1 shows a CAD drawing and schematic for our device. The size of the confocal device compared to the HRME is shown in Figure 6-2.

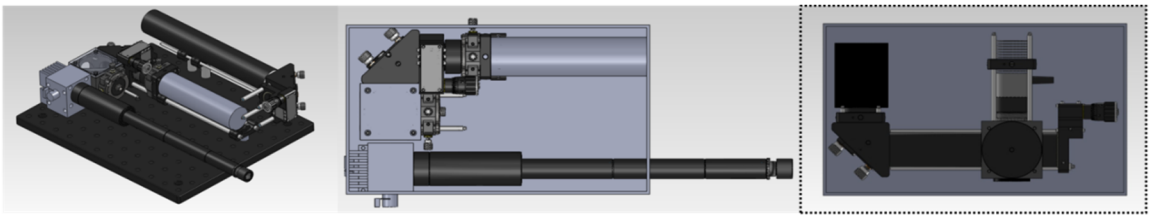

Figure 6-2: Drawings of the HRME (right) and confocal-HRME are shown. The overall dimension of the devices are comparable.

The optical train of the device starts with the handheld laser pointer (Wicked Lasers Arctic III). Using consumer optomechanics (Thorlabs) the laser output beam (1 W 455 nm) is coupled into a single mode optical fiber. This acts as a spatial filter that creates a diffraction limited point of excitation light. Filtered laser light is then collimated and redirected with a dichroic mirror (Semrock). Next, the collimated beam of light is raster scanned over the proximal face of the fiber bundle using two synchronized closed loop galvanometers (Cambridge Technologies), a scan lens, and a finite-conjugate 10X objective (Edmund Optics). Emitted light returning from the fiber bundle passes through the same scanning optics, the dichroic mirror, and is focused onto a pinhole. A photomultiplier tube (Hamamatsu) placed behind the pinhole converts collected photons into an analog voltage signal, which is read by the USB data acquisition device (NI USB-

6363). Finally, a custom LabVIEW program transforms the signal into an image and displays the result in real-time on a laptop computer. The software also provides user controls for file saving, PMT gain, imaging speed, and frame size.

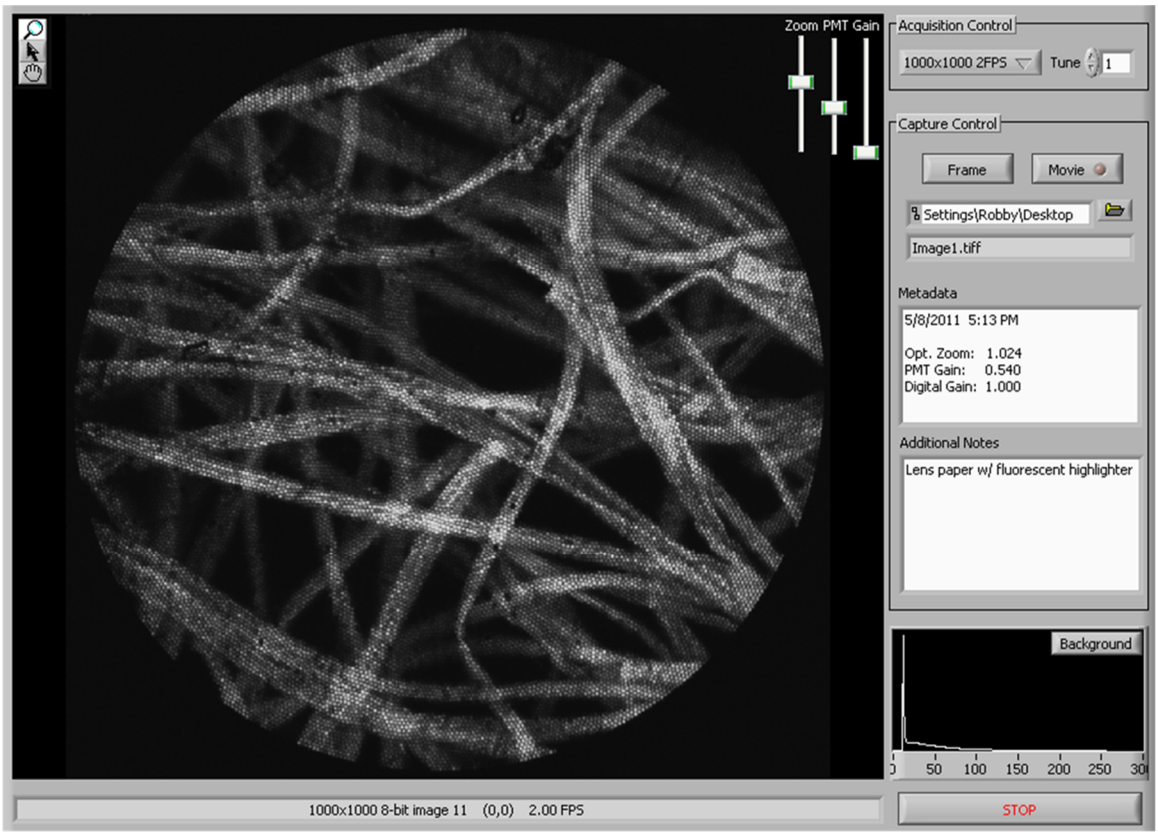

Figure 6-3: The custom software for the confocal HRME.

A key to our device's small size and simplicity is complete optomechanical synchronization through one electronic component. While other scanning systems can require separate cards for the frame grabber, timing electronics, and scanning signals, we use a single USB data acquisition device for all signal operations. This component can acquire 2 million samples per second on one input channel and can send 2.86 million

samples per second on four output channels. We use two output channels to control the raster position of the two scanning galvanometers (see Figure 6-3) and another output channel to control the gain (sensitivity) of the PMT. Using the same timing clock, we read in the PMT voltage for each point within the scan. An image is then reconstructed by plotting consecutive PMT values at the respective x-y scan coordinates. The frame rate of the device is inherently limited by the maximum velocity of the scanning mirrors. In our optical configuration the x-scan mirror can raster scan at a rate of 1 kHz, which corresponds to 2000 forward/backward lines per second. Therefore, we could record a 1000 x 1000 image at 2 frames per second (FPS), a 500 x 500 image at 4 FPS, or a 250 x 250 image at 8 FPS. In order to stretch this limitation, we developed a custom scanning method that scans only the circular area of the fiber bundle. This is accomplished by circle modulating the x-scan, as shown in Figure 6-4. The method increases sampling at

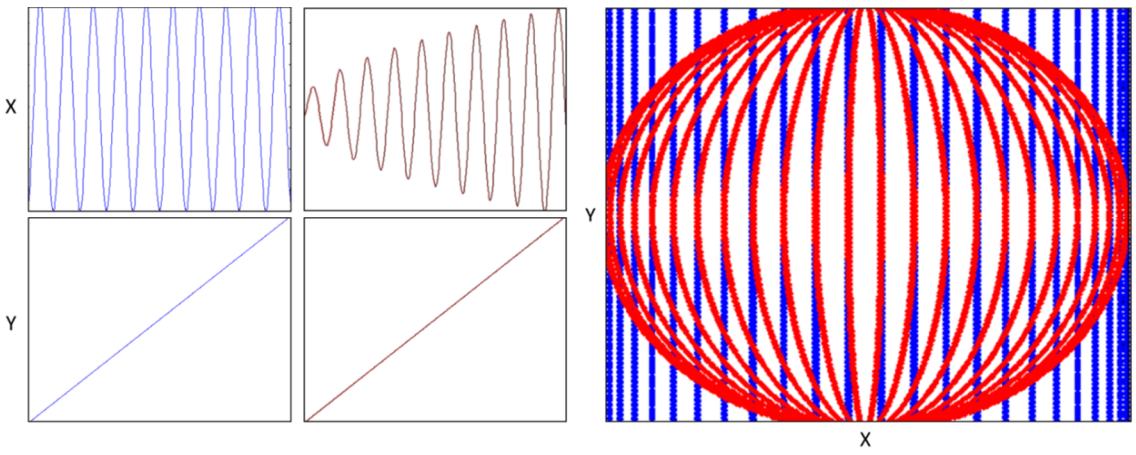

Figure 6-4: A standard raster scan is shown in blue. A circle-modulated x-scan (red) is used so that the laser only scans the fiber bundle surface. Reduced dwell time increases sampling/resolution and light efficiency. Reduced scan amplitude at the top and bottom of the FOV also allows the mirror to run faster, which increases frame rate.

the edges of the fiber bundle, increases dwell time and light collection, and reduces the average amplitude of the scan. By reducing stress on the fast x-scan mirror, we are able to increase imaging rate to 500 x 500 at 5 FPS or 250 x 250 at 10 FPS. Our custom software then uses a high-speed interpolation algorithm to create an image from the circular scan pattern, as shown in Figure 6-5.

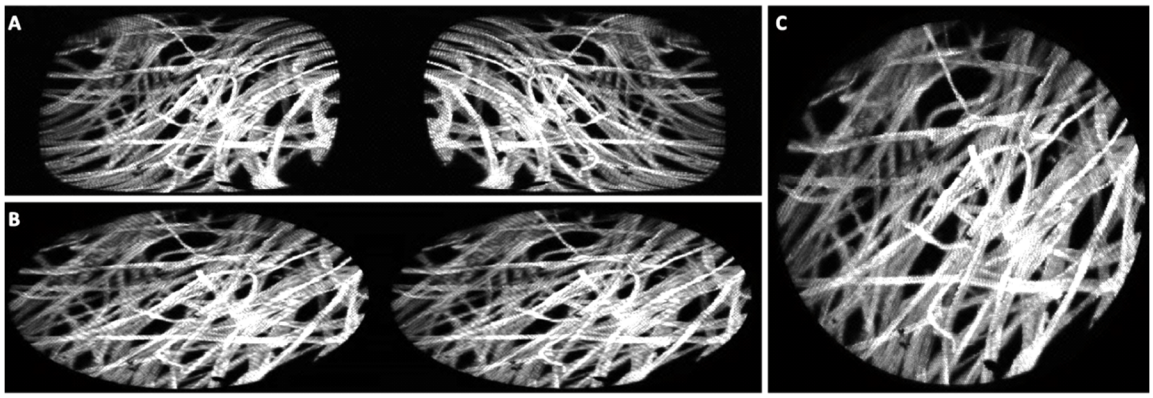

Figure 6-5: Raw data is read into an using a USB DAQ. The one dimensional array is reshaped into a two-dimensional image, which represents the concatenated forward and backward scan of the circle-modulated raster scanning mirrors (A). The image is then resampled to reconstruct linear sampling coordinates of the sample (B). Finally, the two images are interleaved to form the true image (C). The final image is reconstructed in real-time using the custom LabVIEW interface.

The expected optical and acquisition parameters for our system is shown in Figure 6-1 (right). Lateral and axial resolution is dependent on the objective NA and emission wavelength. In our system the theoretical lateral resolution is < 1 µm at the proximal face of the fiber bundle, but is typically limited by the chosen sampling configuration. For example, a 1 mm^2 object sampled by 500 x 500 points will have a lateral resolution of 4 µm according to the Nyquist sampling theorem. This is just enough to resolve the fiber

bundle pattern, which has 3 – 4 µm fiber spacing. The theoretical axial response is 18 µm. By translating a mirror through the focal plane of the objective lens, we determined the full-width half-maximum axial response of the system to be 25 µm, which is also a common experimental approximation for axial resolution. Using a fiber bundle with a distal high-NA miniature objective improves this value.

6.2.2. Structured Illumination HRME

Another method for improving axial response is structured illumination (SI). This technique works by imaging a known sinusoidal pattern onto the focal plane. Using a reconstruction algorithm, it extracts spatial frequency information from the modulated image in order to reject out-of-focus light. Conventional SI requires frequency-modulated images of the sample at three phase positions [76]. The method has been demonstrated in commercial microscopes, in fiber-bundle microendoscope systems, and used for clinical imaging [77]. The benefit of this technique for our application is that it uses most of the same hardware as the current HRME system, including the CCD camera and LED illumination. Possible disadvantages of the technique are (1) possible grid pattern artifacts when moving the quickly over the tissue and (2) low dynamic range and high noise when there is significant background signal or in thick specimens [78].

We were able to create a compact and user-friendly structured illumination microendoscope by (1) using the current compact HRME optical setup, (2) utilizing a small high-precision motorized translation stage, and (3) implementing hardware/software synchronization in a custom LabVIEW interface. Similar to the price

of the confocal endomicroscope system, the structured illumination HRME costs < $10,000. A schematic for the device is shown in Figure 6-6.

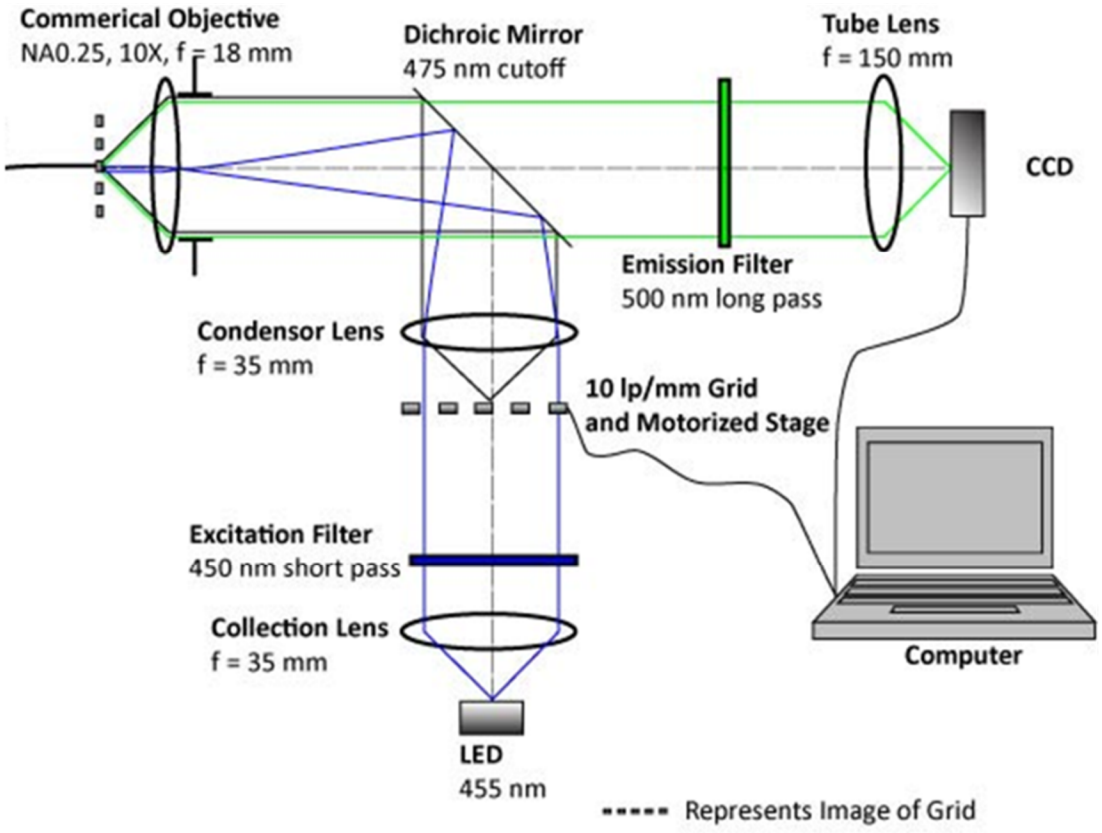

Figure 6-6: The optical train of the structured illumination HRME system. Drawing courtesy of Matt Kyrish.

Our structured illumination setup adds only a 10 lp/mm grid (Thorlabs), a condenser lens, and a motorized stage (Zaber) to the existing HRME setup. Using a custom LabVIEW program we synchronize grid movement and image acquisition, display the sectioned image, and provide user controls for exposure, gain, and file saving. The final size of the system is comparable to the original HRME dimensions. Expected

lateral resolution is equal to that of the original HRME (< 1 μm), whereas the axial response is dependent on the grid frequency. In our configuration, we expect an axial response of ~ 50 μm. Imaging speed is limited by the maximum frame rate of the camera, which is 11 FPS. We found the device performs best at 7.5 FPS, because this allows more settling time between motorized stage positions. Although the sectioned images are displayed with a lag of two frames, our real-time algorithm displays sectioned images at the frame rate of the camera.

6.3. Results

In this section we show imaging results from the confocal, structured illumination, and original HRME systems. Results are shown for standard optical testing targets such as lens paper, as well as *ex vivo* and *in vivo* tissue specimens. We also provide direct comparisons between systems and compare our results to commercial benchtop confocal devices. All samples were stained with 0.01% proflavine and imaged according to IRB protocols (Rice 11-119E and 08-95E).

6.3.1. Confocal Imaging

Figure 6-7 shows images of oral mucosa using the confocal microendoscope system without the fiber bundle attached. These images provide a baseline for imaging performance, because the pixelation effect from the fiber bundle will reduce object sampling and degrade image quality. Cell membranes and nuclei are clearly visible

throughout the field-of-view. A wide FOV of 2 mm^2 was selected in order to indicate the maximum area that the system can image. This FOV is much larger than the < 1 mm^2 FOV needed to image the fiber bundle.

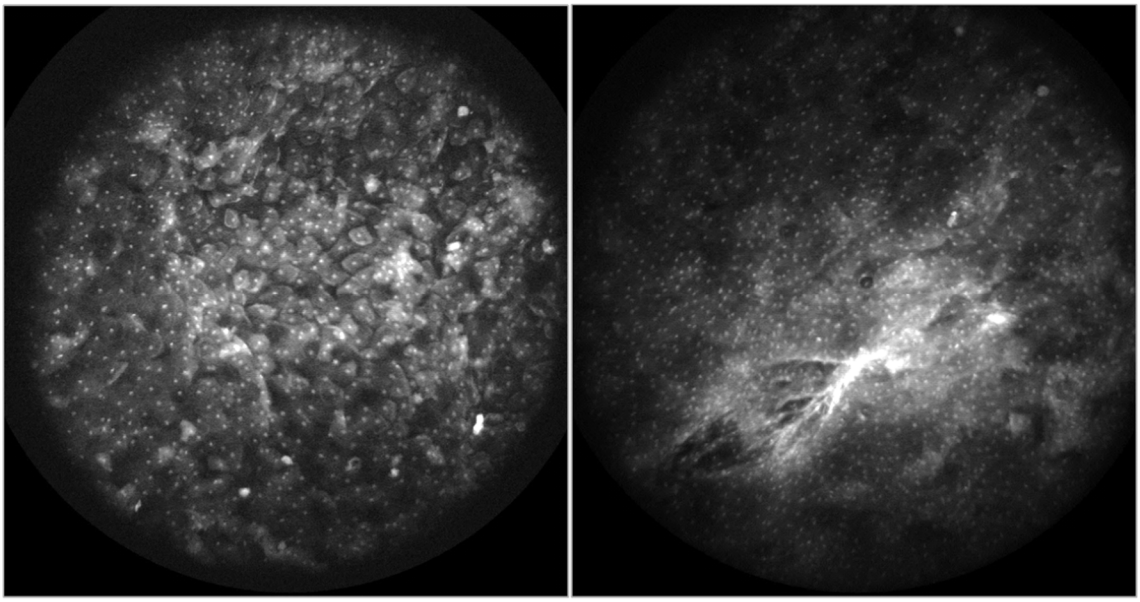

Figure 6-7: The imaging performance of the confocal HRME with no fiber bundle in place. (A) and (B) are images of stratified squamous cells from the lower lip of a normal volunteer labeled with proflavine.

After attaching the fiber bundle, the confocal HRME system was compared to the original HRME system and a commercial benchtop confocal system using an *ex vivo* mouse tongue specimen. Figure 6-8A/B are images acquired from the same field-of-view in the specimen. The confocal system has approximately 9X greater Michelson contrast than the original HRME image. Increased contrast allows cellular morphology and nuclei to be more easily visualized. Figure 6-8C shows an image from the same tissue specimen

obtained with a commercial confocal system, which further demonstrates the effect of increased lateral and axial resolution/response.

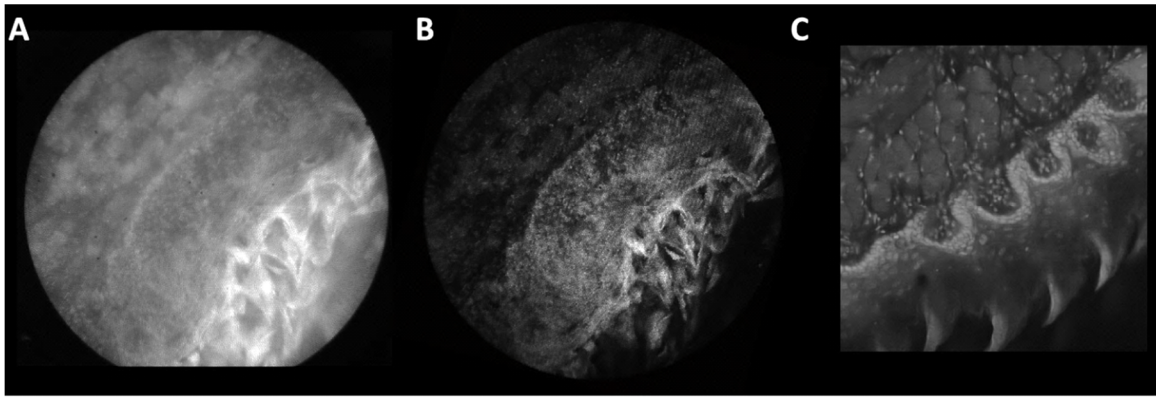

Figure 6-8: Epithelium tissue from an *ex vivo* mouse tongue specimen was labeled with proflavine and imaged with a (A) conventional HRME, (B) confocal HRME, and (C) commercial benchtop confocal microscope. The background in the conventional HRME image makes is difficult to visualize subcellular features. The confocal images have ~9x higher contrast.

Finally, confocal fluorescence images were acquired *in vivo* from the lower lip of a normal volunteer. Images were obtained at 6 FPS and 500 x 500 sampling. Results shown in Figure 6-9 indicate that resolution, imaging speed, and signal intensities are adequate for visualizing proflavine-stained nuclei *in vivo*. In addition, we found low background signal throughout our imaging experiments, which means there is improved axial response in thick tissue specimens compared to the HRME. Overall, *ex vivo* and *in vivo* imaging results suggest that our compact, low-cost technique for improving axial response in the HRME is a promising solution.

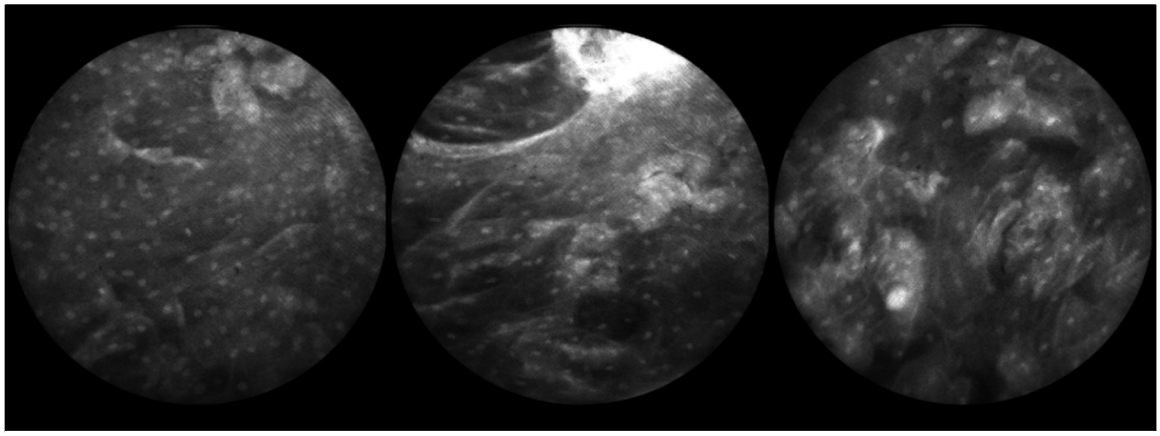

Figure 6-9: Confocal microendoscope images from *in vivo* oral mucosa of a normal volunteer obtained with the system operating at 6 frames per second. Cells nuclei, membranes, and tissue architecture is clearly visualized.

6.3.2. Structured Illumination Imaging

Figure 6-10 shows imaging results from *ex vivo* breast tissue. Results from the original HRME, structured illumination HRME, and a benchtop commercial confocal microscope (Lucid VivaScope 2500) were compared. We included images from the commercial confocal device to demonstrate the imaging quality that pathologist typically require for detecting cellular features indicative of cancer. It can be challenging to quantify cellular features in breast tissue using the original HRME because cells are small and crowded, and a high background signal is present (see Figure 6-10A). For example, the top row of Figure 6-10 shows images of a breast lobule, which contains small compact cells arranged in a glandular structure. These features are lost within the background signal of the original HRME, because there is no mechanism to block out-of-focus light. Using devices with smaller axial response significantly reduces background signal and increases image contrast, which increases visibility of the glands and other

features. Figure 6-10 (bottom row) shows an example of cancerous breast tissue. In this case and throughout our entire breast imaging experiment, we found improved axial response always increased visibility of cellular features. This is important for improved cancer detection by a pathologist or through automatic quantitative methods.

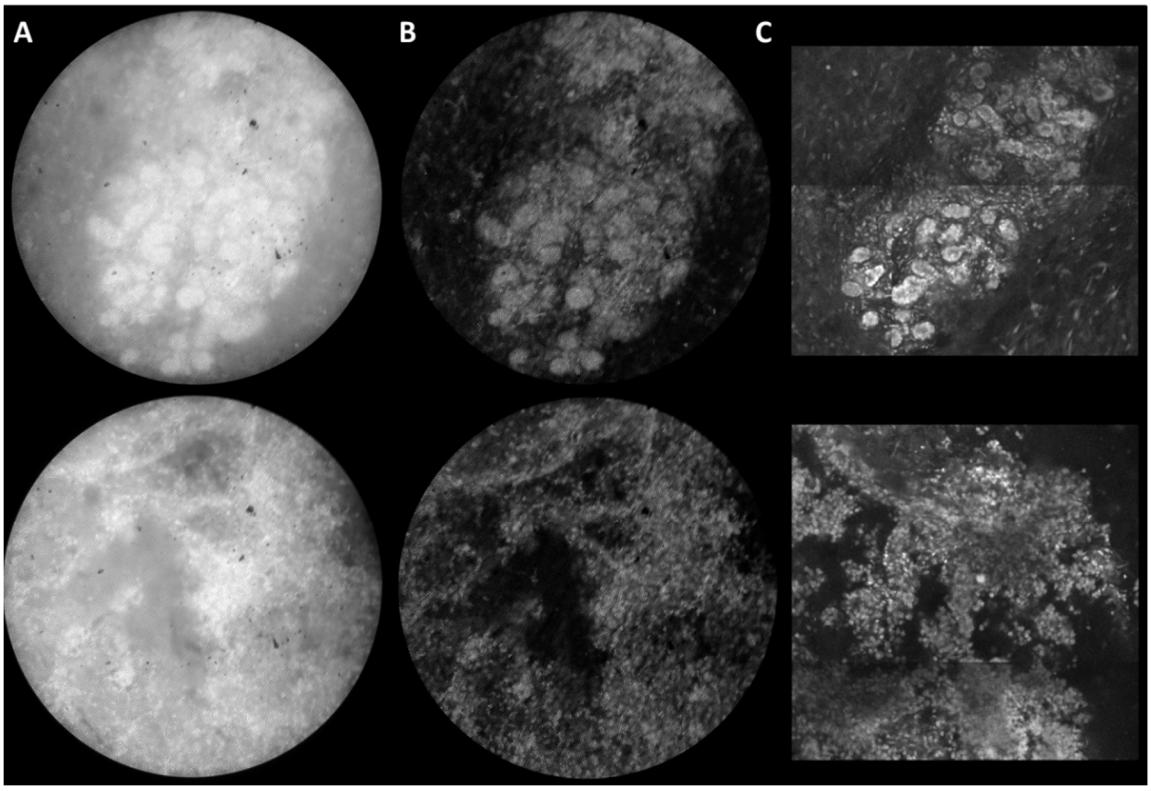

Figure 6-10: Images of *ex vivo* breast tissue using (A) the original HRME, (B) the structured illumination HRME, and (C) a commercial benchtop confocal microscope. The top row shows images tissue from a lobule, which has small crowded nuclei and distinct glandular morphology. The bottom row shows images obtained from a tumor specimen, which has small crowded nuclei with disorganized morphology. In both specimens the original HRME has high background signal and low contrast compared to the structured illumination HRME and commercial confocal microscope. The devices with increased axial resolution can more clearly visualize cellular features, which can provide a more accurate diagnosis. Images acquired by Matt Kyrish and Jessica Dobbs.

6.3.3. Confocal/SI Comparison

Finally, imaging results from the original, structured illumination, and confocal HRME were compared using fluorescently-labeled lens paper. We developed a convenient qualitative test that could be performed in our lab setting with all three devices. First, the distal end of a fiber bundle was placed in contact with lens paper using a translation stage. The proximal end was then attached to the HRME system and images were acquired, as shown in Figure 6-11A (top row). Next the proximal end was unattached and then coupled to the structured illumination system for imaging, as shown in Figure 6-11B. The same procedure was repeated for the confocal system in Figure 6-11C. Using this procedure, the same FOV was imaged with each system, which allows direct comparison between modalities. Results show significant background reduction for both the structured illumination and confocal systems. In these images the structured illumination system also has higher contrast. For some specimens it is useful to image with higher lateral resolution by using a custom-made 3X miniature objective attached at the distal end of the fiber bundle. The additional optics can reduce the FOV and decrease light throughput. Therefore, we also compared imaging performance when using a 3X miniature objective. Figure 6-11 (bottom row) shows these results, which also demonstrate improved background rejection in the structured illumination and confocal systems. In these images the confocal HRME has higher contrast and less noise, because of the high power laser and high sensitivity PMT used in the system.

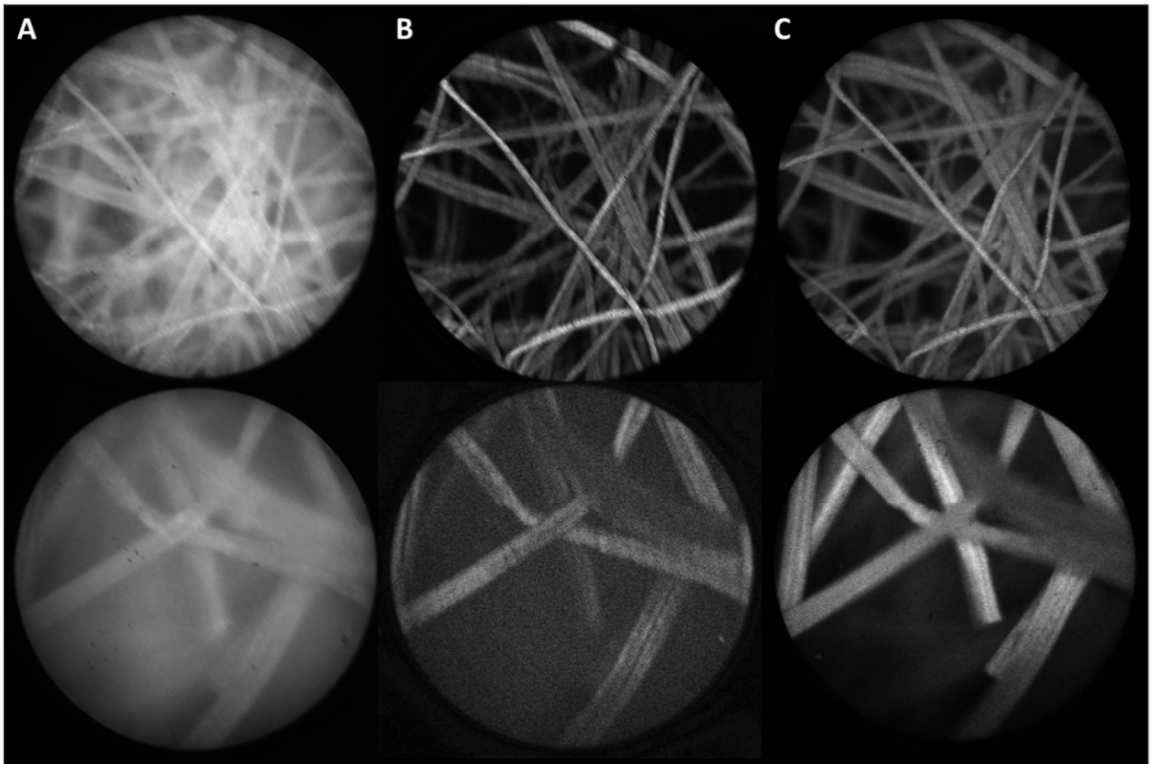

Figure 6-11: Fluorescently-labeled paper was imaged with the (A) conventional HRME, (B) structured illumination HRME, and (C) confocal HRME. The top images show the performance of the system with no lens at the distal end; the bottom images were taken through a custom 3X microendoscope objective.

6.4. Discussion

In this chapter we presented compact, low-cost implementations of traditional structured illumination and confocal microendoscopes. Both systems exhibit improved axial response compared to the HRME used in our current clinical studies. They are an order of magnitude less expensive than commercial devices with comparable imaging specifications. In the future we will expand testing of custom-made high-NA

microendoscope lenses. A custom distal lens will enable imaging below the tissue surface, closer to the basement membrane where epithelial cancers originate. This will allow earlier detection of cancer. When imaging through a distal objective, our HRME systems with improved axial response will be essential for blocking foreground intensity at the tissue surface. We believe these systems will become valuable tools for investigating the effectiveness of microendoscopy for diagnosing dysplasia and cancer at the point-of-care.

Acknowledgements

This work was supported by R01A124319 and R01EB007594.

Chapter 7

Image mapping spectrometry: calibration and characterization*

*The contents of this chapter were submitted to a journal as the following manuscript: N. Bedard, N. Hagen, L. Gao, and T. Tkaczyk, "Image mapping spectrometry: calibration and characterization," Optical Engineering (2012).

While high resolution endomicroscopy is important to visualize subcellular morphology, a modality called spectral imaging can provide information about the biochemical properties of tissue that a traditional camera cannot detect. In this chapter the operational principle, calibration, and testing of a spectral imaging device is described. In chapter 8 we discuss how this device is modified for widefield clinical imaging. The technique, called Image Mapping Spectrometry (IMS), is a spectral imaging technology that simultaneously captures spatial and spectral information about an object in real-time. Here we present the calibration procedure for the IMS as well as the first detailed

evaluation of system performance. We correlate optical components and device calibration to performance metrics such as: light throughput, scattered light, distortion, spectral image coregistration, and spatial/spectral resolution. Spectral sensitivity and motion artifacts are also evaluated with a dynamic biological experiment. Results are important to any potential users/developers of an IMS instrument and to anyone who may wish to compare the IMS to other imaging spectrometers.

7.1. Introduction

Hyperspectral imaging (HSI) is utilized throughout the fields of astronomy [79], remote sensing [80], food science [81], and biotechnology [82]. By collecting both spatial and spectral information about an object, it provides a full three-dimensional distribution, called a hyperspectral datacube. Linear unmixing or other spectral analysis algorithms can use this spatial-spectral dataset in order to identify concentrations of chemicals within a scene. [83]. Traditional hyperspectral imagers implement a temporal scanning technique to sequentially collect the hyperspectral datacube by either point-scanning, line-scanning, or wavelength-scanning [84]. These systems include pushbroom, whiskbroom, liquid-crystal tunable filter (LCTF), and acousto-optic tunable filter (AOTF) imaging spectrometers. More recently, a class of hyperspectral imagers has come forward that collects the entire datacube simultaneously. Some examples of such systems are the Computed Tomographic Imaging Spectrometer (CTIS) and the Coded Aperture Snapshot Spectral Imager (CASSI) [85-87]. These “snapshot” instruments

incorporate specialized components to distribute an object's three-dimensional spatial-spectral information onto a two-dimensional focal plane array. A transformation is then used to reconstruct the three-dimensional hyperspectral datacube from the two-dimensional image recorded on an image sensor.

Another class of hyperspectral imaging systems provides all spatial-spectral information on a single or multiple CCD image sensors with a one-to-one correspondence between datacube voxels and detector pixels. There are three major modalities in this group: Image Slicers [88], field splitting by fibers [89] or lenslet arrays [90], and Image Mapping Spectrometers (IMS) [91-93]. By collecting information simultaneously, while utilizing simple datacube remapping algorithms, these systems add several powerful capabilities to hyperspectral imaging, including: faster data collection and image reconstruction, higher light-throughput, less motion artifacts, and real-time spectral unmixing. These features enable applications that require the ability to distinguish objects with similar spectral properties at high temporal resolution. Of particular interest is an IMS system that demonstrates high spatial sampling of 355 x 350 over 41 wavelengths, using a single large format CCD image sensor. It also provides high light throughput of above 50%. In the field of bioscience, the IMS has been used to investigate cellular dynamics with multiple fluorescent biomarkers [94], to perform real-time brain imaging [95], and for endoscopic imaging of oral mucosa [72].

While previous publications presented datacubes and experimental results that show IMS' basic performance [72, 91-95], a detailed discussion of system calibration and

characterization of its operational limits has not yet been published. In Section 2, this chapter sites the current literature related to IMS calibration and hardware performance. In Section 3 an improved spatial-spectral calibration procedure is presented for the IMS. This new method is necessary to account for imperfections in raw detector data. Section 4 describes a suite of tests developed to measure optical performance of the IMS after calibration. The measured performance metrics are linked to imperfections in optical components/assembly as well as system calibration. The tests can readily be applied to other microscope-coupled hyperspectral devices (Image Slicers, pinhole systems, etc.). In Section 5, motion artifacts and spectral linear unmixing of the IMS are tested with a real-time biological experiment. The results of the performance tests provide the first benchmark for IMS technology. Potential users/designers of IMS instruments can draw also from the tests and analyses in order to design experimental setups, evaluate their systems, or compare to other imaging spectrometers.

7.2. Background

The detailed principle of the IMS system operation was first described in [92]. It is useful to briefly describe how the IMS operates in order to discuss calibration requirements and relate performance results to hardware components. Here we limit the discussion to focus on the principle/component impact on imaging performance.

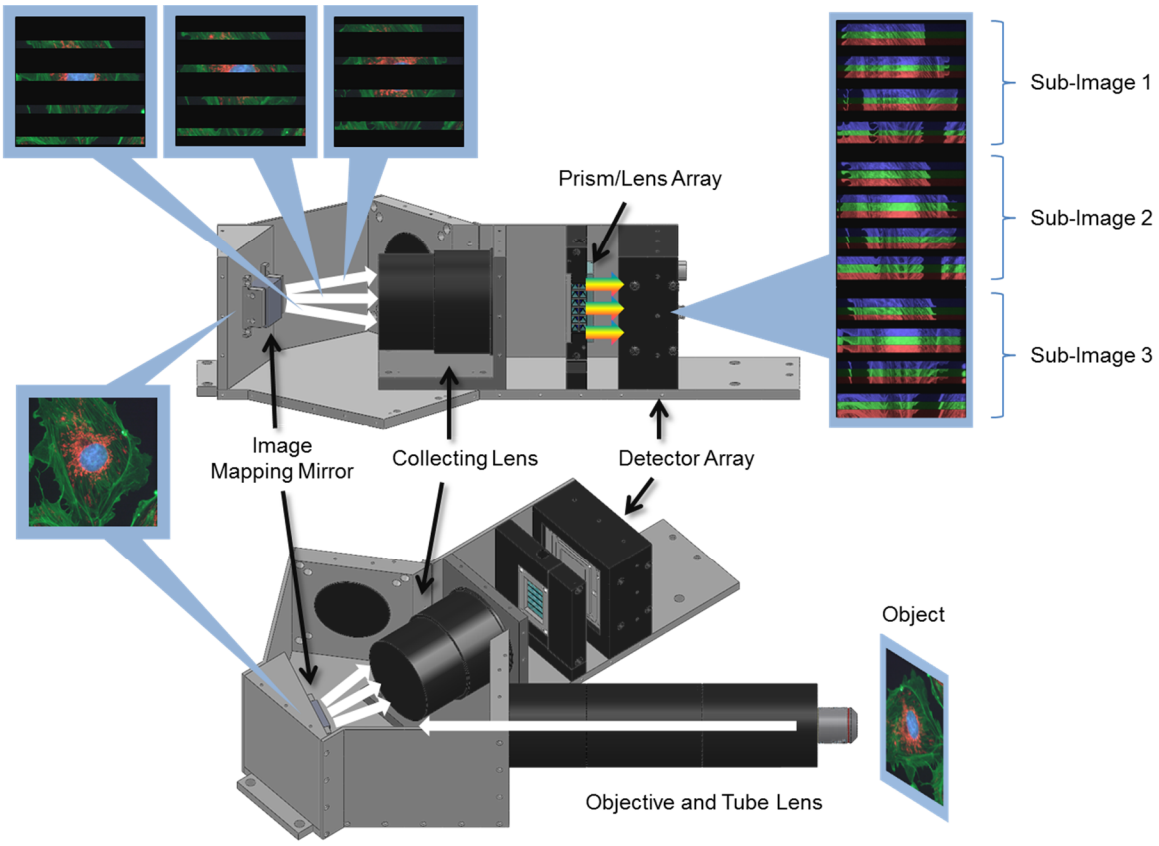

Figure 7-1: The operating principle of the IMS system.

The IMS breaks an image into zones to create void regions. This is accomplished through a specially designed mirror and an array of re-imaging systems. The image zones are then dispersed and spatial-spectral information from the object is recorded on a CCD image sensor. The essential component is the "image mapping mirror" also called an image mapper. The component is placed in the image plane of fore optics and in its simplest form is a faceted mirror composed of many reflective long strips. The facets of

the mirror have different two-dimensional tilt angles that reflect image zones into different directions. Figure 7-1 shows a schematic of the IMS system that contains a simplified mirror with only twelve facets. The image mapping mirror used in the evaluated system has 355 facets.

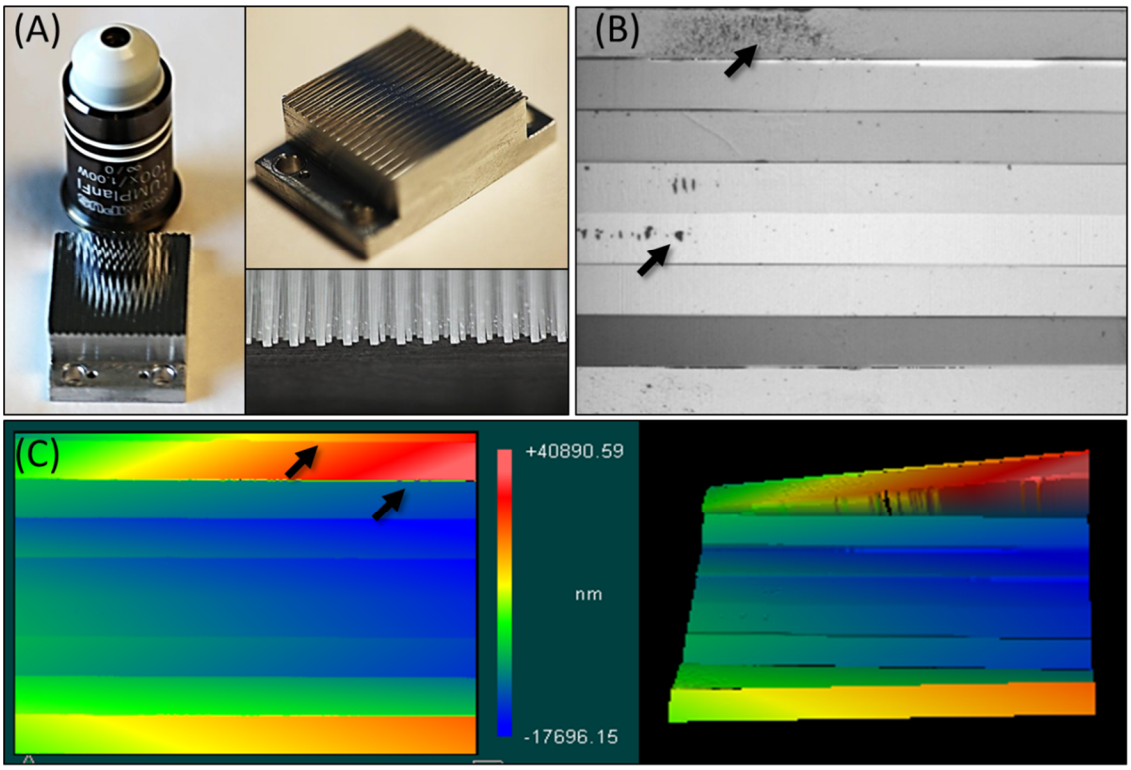

Figure 7-2: (A) The image mapping mirror is composed of 350 reflective facets that are 65 µm x 25 mm long, each with a two-dimensional tilt angle to redirect image zones. (B) A close-up image of eight mirror facets with roughness and debris indicated. (C) White light interferometry data shows roughness on facets as well as edge artifacts.

For the purposes of this publication the authors will not analyze optical design and tolerance analysis since this topic was already discussed in [72, 91]. We will focus here on evaluation of performance of the system "as is," which may help potential

users/builders characterize their systems. The image mapping mirror design, fabrication, and optical characterization was discussed in [93]. The authors showed that the fabrication process results in imperfections within mirror facets, such as surface form error, roughness, and width variations (as shown in Figure 7-2). Since the facets lie at an intermediate image plane, these imperfections produce artifacts in the collected data. In this chapter we discuss how these imperfections affect reconstructed datacubes.

The sliced and dispersed raw IMS image is not “human readable” and must be remapped in order to reconstruct a spatial-spectral datacube. A basic, proof-of-concept mapping calibration procedure was presented in [91]. This approach did not account for: monochromatic and polychromatic distortions, defocus, or clipping within the optical train of the system. The reconstruction of datacubes using this previous calibration method produced datacubes with lateral chromatic aberration and spatial misalignments.

7.3. Calibration

The calibration procedure discussed here has not been published, but it has been used to calibrate the systems described in our previous publications [64, 72, 94, 95]. In order to clarify the calibration procedure, we will first briefly describe the raw data from the IMS evaluated in this chapter. Our experimental system contains an image mapping mirror with 355 mirror facets that redirect image zones into twenty-four different sub-images on the detector (corresponding to four vertical and six horizontal facet tilt angles). Redirected lines from the object are separated by 41 pixels, which allows for 41 pixel

spectral sampling. Figure 7-3 shows false-colored raw data from the IMS. The data in Figure 7-3a/b is recorded from an empty microscope stage lit with Koehler illumination from a halogen lamp. A neutral density filter and a daylight filter were used to match the spectral density of the lamp to the sensitivity of the CCD, which created a uniform detector signal over the broad spectrum. The spectral range was limited to 470 - 670 nm using a bandpass filter in order to prevent overlap of dispersed light between adjacent facets. Figure 7-3c shows a subsection of the IMS's CCD imaging a pinhole illuminated with 470 – 670 nm light; here one pixel of spatial information and 41 pixels of dispersed spectral information are recorded. Figure 7-3d is the raw data from a pinhole illuminated with narrowband 550/1 nm light.

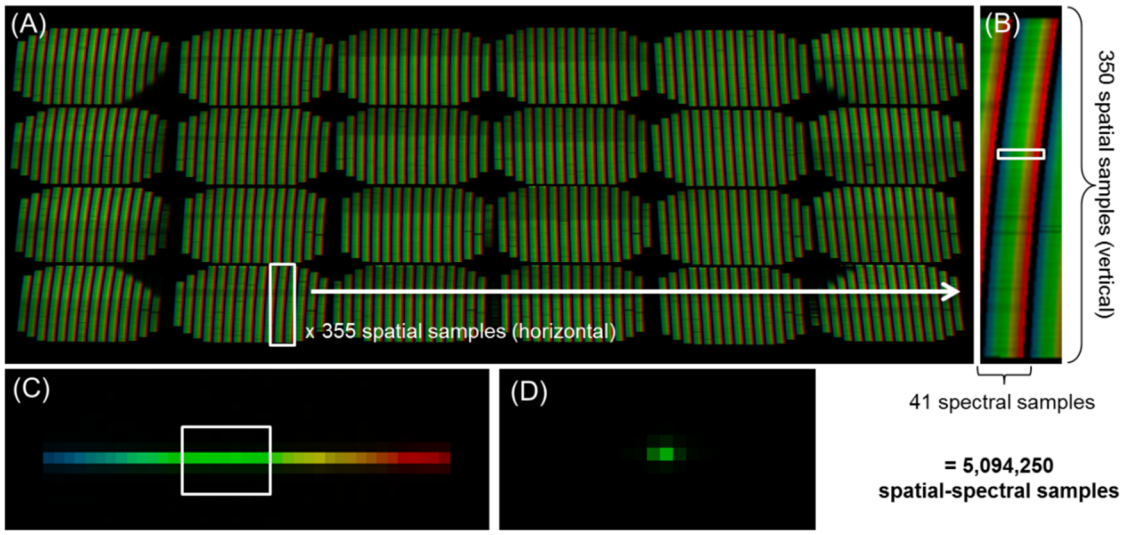

Figure 7-3: The IMS detector response to different spatial and spectral samples. (A) Detector response to uniform sample illuminated with white light (false-colored to illustrate spectral content). (B) Close-up of one dispersed facet image, which corresponds to the spatial-spectral information of one line in the object. (C) Response to spatial point-source (i.e. a pinhole) illuminated with white light. (D) Response to a spatial point-source illuminated with narrowband (550/1 nm) light.

We primarily use the IMS to image thin microscope samples with negligible depth information, therefore our calibration establishes a one-to-one correspondence between each voxel in the hyperspectral datacube (x, y, λ) and a pixel location on the CCD camera (u, v) [91]. The complete calibration procedure consists of three steps: (1) Remapping with the transformation lookup table $(x, y, \lambda) = T^{-1}\{(u, v)\}$, (2) Flat-field correction, and (3) Spectral sensitivity correction.

The goal of the mapping calibration step is to determine $(x, y, \lambda) = T^{-1}\{(u, v)\}$. T^{-1} is effectively a lookup table that is the same size as the datacube, which contains a subpixel detector value at each index. In order to determine T^{-1}, the forward mapping T is found first by sequentially illuminating integer coordinates (x, y, λ) throughout the datacube while analyzing the detector (u, v) response. Once we establish the relationship T from scene to detector, we can apply the reverse mapping T^{-1} or "remapping" to transform raw detector data into a datacube. The procedure works by scanning a spatial pattern (e. g. a pinhole) illuminated with four narrowband filters throughout the field of view (FOV) of the IMS system at (x, y, λ) object coordinates. Each position of the spatial pattern provides a point image in a region on the detector (Figure 7-3d/4a). The subpixel center position (u, v) of the point image is determined with a peak-finding algorithm [59]. Forward mapping and reverse mapping are conceptually illustrated in Figure 7-4. Parameters used during the calibration procedure are shown in Table 7-1. Remapping the datacube c using the lookup table is implemented in real-time using bicubic interpolation [96] of raw detector data. Section 4D evaluates the accuracy of remapping.

$$c = interp2(raw, lookup) \quad (1)$$

Flat-field correction is also performed in order to account for intensity variations in the raw image. The procedure starts by recording a datacube *i* from an empty microscope stage lit with halogen lamp Koehler illumination. All subsequent datacubes *c* acquired by the IMS are divided by the datacube acquired with Koehler illumination.

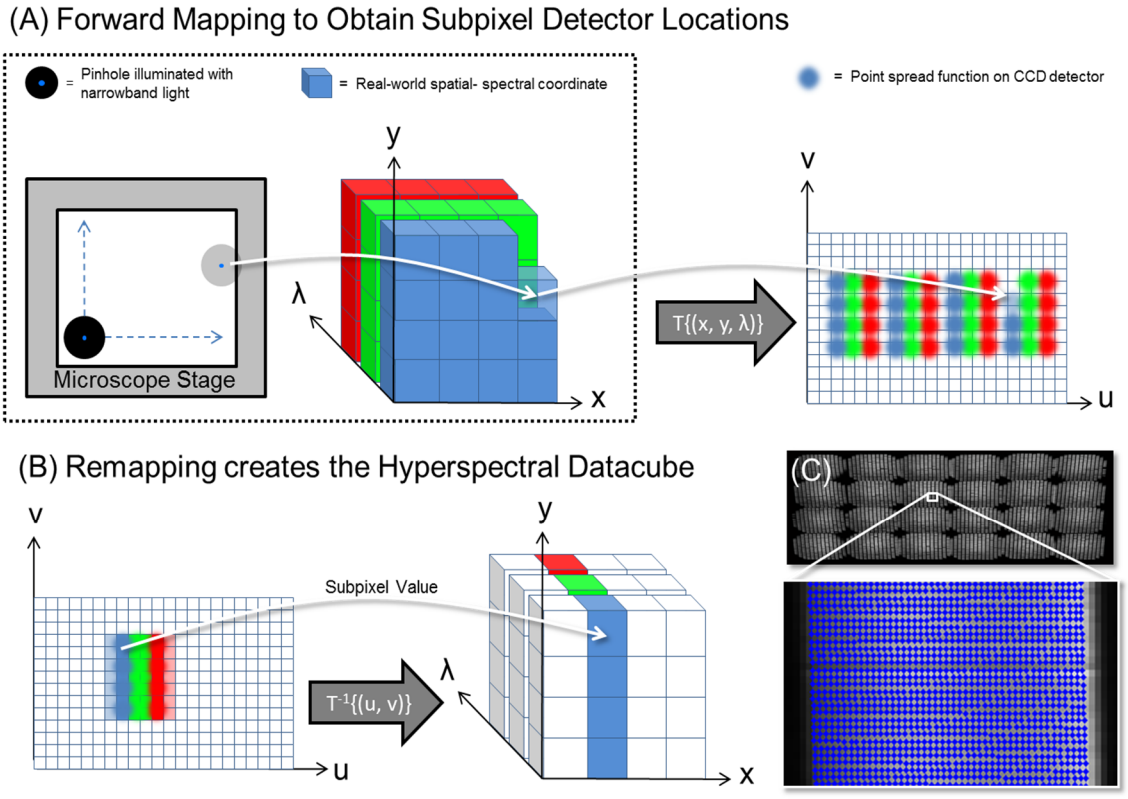

Figure 7-4: Sequential experimental calibration procedure. (A) Each element of object space (x, y, λ) can be illuminated sequentially with a spatial-spectral point source while recording the detector (u, v) response. The forward mapping of object coordinates to detector space describes $T\{(x, y, \lambda)\} \rightarrow (u, v)$. (B) Applying the remapping $T^{-1}\{(u, v)\} \rightarrow (x, y, \lambda)$ allows the object datacube to be accurately reconstructed from raw data. (C) Subpixel coordinates obtained from the mapping calibration are overlaid on raw detector data.

This normalizes the response of every datacube voxel. Next, the spectral sensitivity is corrected. Each of the N spectral images λ within the datacube is multiplied with a correction factor s to match the corresponding intensity of the halogen lamp spectrum, as determined by a calibrated point spectrometer. The final datacube *final* includes both flat-field and spectral correction of the raw detector data [97].

$$final_{\lambda=1:N} = (c./i)_{\lambda=1:N} .* s_{\lambda=1:N} \quad (2)$$

Table 7-1: Calibration parameters and settings for the evaluated IMS system.

Calibration Parameter	Value
Microscope Objective, IMS Relay Objective	5X, 2.5X
Image Mapper Dimensions	~23.4 mm x 26 mm, 65 µm facets
Slit Size, Slit Size after Magnification	5 µm x 5 mm, 62.5 µm x 62.5 mm
Spatial Samples Perpendicular, Parallel to Facets (x, y)	667, 120
Motorized Stage Step Size (x, y)	3 µm, 16 µm
Spectral Samples (x, y)	1 (determines facet order), 4 (determines dispersion)
Total Images Recorded, Total Disk Space Compressed	1147 images, ~100 MB

7.4. IMS Evaluation Tests

There are no established standards for performance evaluation of snapshot hyperspectral imagers. For that reason, in order to assess the hyperspectral datacubes obtained from the calibrated IMS, we developed a suite of tests to measure different metrics of data quality. We decided to evaluate three categories of IMS data quality: intensity parameters, mapping errors, and overall performance. Intensity parameters are

inherent to the hardware of the system and are evaluated with tests for intensity variation, light throughput, and scattered light. Mapping errors are dependent on the accuracy of the calibration lookup table and are evaluated with tests for geometric error, image stretch, and spectral image coregistration. Overall optical performance tests include spatial resolution, spectral resolution, and spectral accuracy/variability. While some of the tests are specific to the IMS instrument, many of the procedures can also be used to measure performance of other hyperspectral imaging techniques. The IMS specific tests are indicated with asterisks in Table 7-2. Each section below summarizes the algorithm used for the test and the results found for the calibrated IMS.

Table 7-2: Measured Parameters of the IMS Camera. Tests without an asterisk (*) can also be used to evaluate other hyperspectral imagers.

Intensity Parameters	Mapping Errors	Overall Performance
Intensity Variation*	Geometric Error	Spectral Accuracy/Variability
Light Throughput*	Stretch	Spectral Resolution
Scattered Light	Coregistration	Spatial Resolution

During testing the IMS system was coupled to the side port of a Zeiss Axio Observer inverted microscope. Two spatial targets were used: a Ronchi ruling rotated at 0^o, 45^o, and 90^o, and a high-resolution 1951 USAF resolution target. Several narrowband and plastic transmission filters were used to evaluate spectral performance. All remapped datacubes were obtained according to the calibration procedures described previously.

A. Intensity Variation

Ideally, the intensity of reflected light collected from the image mapping mirror should be constant. In reality, the uniformity of the detector image is affected by: the image mapper quality [93], the re-imaging optical train, and the CCD response. It is important to measure variations in the raw detector image because they correspond to loss in dynamic range. For example, if one facet image or a portion of a facet image is less intense than another, then this area will have lower signal-to-noise ratio and dynamic range. During calibration, flat-field correction was used to aesthetically compensate nonuniformities in the datacube [97].

To assess the amount of total system non-uniformity, Koehler illumination was used in transmission mode with a halogen lamp to uniformly irradiate an empty microscope stage. Figure 7-5a shows raw data from the IMS obtained with this setup. Facet images do not have a constant intensity value within or between facets. Figure 7-5b shows the optical components that most likely contribute to these intensity variations in the data. For example, imperfection in mapper fabrication causes debris and roughness on facets, which create localized decreases in image intensity. Light that is clipped by the collecting objective creates regions of missing information in the corner sub-images. Also, prism/lens array alignment can cause defocus of facet images, which reduces intensity. These artifacts affect other important metrics of datacube quality in addition to intensity variation. For example, defocus of a facet image will cause blur in

the direction of spectral dispersion, which reduces spectral resolution, as discussed in Section 4F. Figure 7-5c reveals a close-up reconstruction of nine uniformly-illuminated facet images in the image mapping mirror. Contrast has been enhanced to highlight the overall change in intensity that can be seen on each reconstructed line.

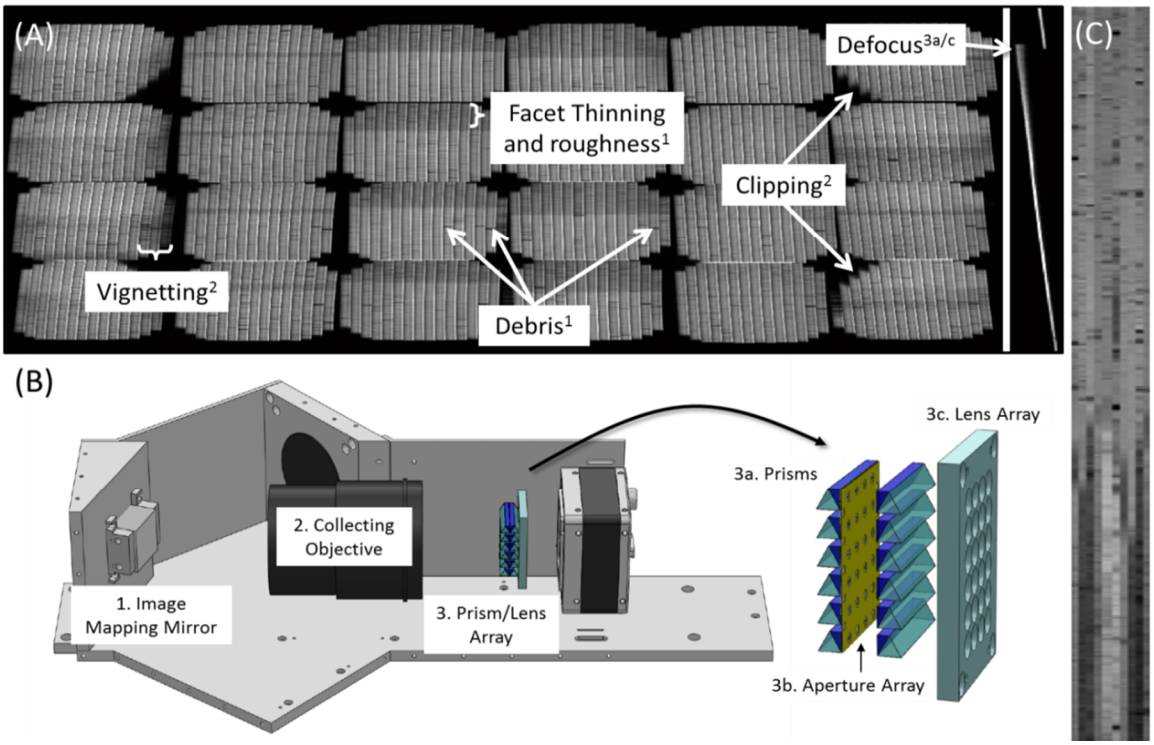

Figure 7-5: (A) Left: A flat-field broadband image from the IMS with varying facet image intensity. Right: A close-up of a flat-field narrowband facet image from the IMS, showing defocus of the facet. These design, fabrication and assembly limitations cause intensity variations in the raw data. The superscript number corresponds to the system component in (B) which causes the problem. (C) A contrast-stretched image of nine facets after remapping shows overall and localized facet image non-uniformities. These flaws also translate to reduced resolution, missing data and/or geometric errors in the remapped datacube.

A Matlab script was written to quantify variation of facet image intensities on the detector, which is an overall measure of image mapper variations, vignetting, clipping,

prism/lens array affects, as well as reconstruction. To quantify the uniformity of intensity within facet images, the relative standard deviation (%RSD) was calculated for each facet image in the panchromatic flat-field datacube. The %RSD of intensity within facets ranged from 2.6 to 26%, which indicated that some facets have significant internal non-uniformities. On average, there was an 11% RSD of intensity within a facet. Comparing the mean intensities between all facets, there was an 8.6% RSD between facets (the value was calculated as an average irradiance for each facet). This suggests that localized variations in facet reflectivity have a more significant effect on image non-uniformity than overall facet-to-facet variation.

B. Light Throughput

The next test for the IMS system was to measure optical efficiency of our system, defined as the ratio of light entering the system to light recorded on the detector. To examine throughput of the IMS, an iris was placed at the sample plane of a microscope and illuminated with narrowband light at three wavelengths. By moving the IMS's CCD detector, light levels were captured at three locations in the system: at the side port of the microscope, at the mapping mirror, and at the IMS detector plane. The light intensity and integration time were kept constant throughout the experiment, such that the CCD was below saturation at each location; also, the extent of the field was limited so that the entire sample was captured on the CCD. Light intensity at each location was determined by summing all pixels on the CCD after a background subtraction.

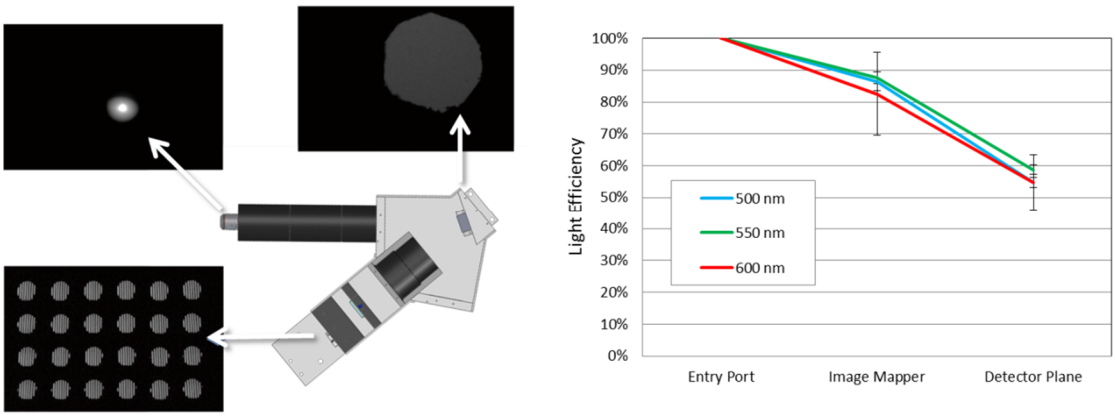

Figure 7-6: Light throughput test. (Left) The three locations that light was measured using a large-format CCD. (Right) A graph of the overall intensity at each location, plotted for three different wavelengths.

Figure 7-6a illustrates the experimental setup and example imaging results from one wavelength test. Complete results are graphed in Figure 7-6b. We measured the relay arm to have 89% throughput, which includes an objective, tube lens, and spectral filters. The redirecting and dispersing optics of the system are ~65% light efficient, which corresponds to a total light efficiency of 58%.

C. Scattered Light

Scattered light is defined as any light that reaches the detector other than defined by the optical system design. In general, scattered light originates from diffuse reflection and back-reflection off optical surfaces. As light passes through a surface a small amount of scatter occurs that can appear as background in the image, thus reducing contrast and signal-to-noise ratio. Devices with a large number of elements such as the IMS can be more prone to effects related to scattered light. In the IMS, light from the sample passes more than twenty surfaces, including the image mapper, prism array, and lens array. To

assess whether this significantly affects image quality, scattered light was measured in an IMS datacube as well as in a digital image from a standard scientific grade CCD camera (Qimaging Retiga EXi) placed at the microscope side port.

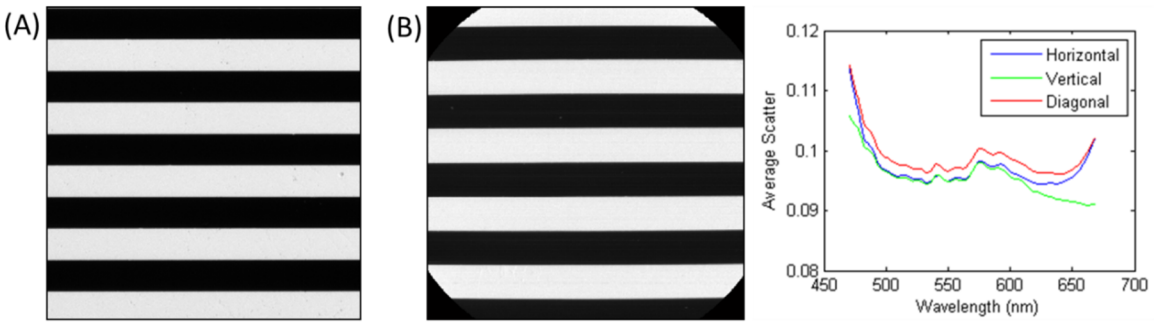

Figure 7-7: (A) An image of a Ronchi ruling acquired with a standard CCD camera placed at the side port of a microscope. After background subtraction and flat-fielding, the signal to background ratio was measured to estimate scatter. (B) A similar procedure was repeated for each spectral image of three IMS datacubes; the results are graphed on the right.

In order to measure scattered light, an approximation was made about the Ronchi ruling images: the center of the dark regions should be exactly zero (although, in reality the contrast is not exactly 100% at this spatial frequency - therefore this is a conservative approach for the measurement). Any loss of contrast within dark regions of the Ronchi images were assumed to be from scattered light. For the IMS data, each of the Ronchi ruling datacubes (0^o, 45^o, 90^o) were first flat-field corrected according to the calibration procedure and then background-subtracted to reduce the effect of dark current. Each spectral image was segmented into three groups: a “high” group that contained pixels with normalized intensity greater than 0.75, a “low” group normalized intensity less than

0.25, and other. Next, the sum of low intensity regions was calculated and divided by the high intensity regions. The resulting “mean scatter” value was found for each spectral image independently to produce a vector of scatter vs. wavelength (see Figure 7-7). The average scattered light over all wavelengths and all Ronchi ruling orientations was 9.79%. The same procedure was repeated for flat-field, background, and Ronchi ruling images acquired with the standard CCD camera placed at the side port of the microscope. In this case, we measured the mean scatter to be 6.81%. This suggests the microscope system and/or the Ronchi ruling is responsible for the majority of scatter. Therefore, the IMS recorded spectral images with approximately 3% more scattered light than measured by the standard CCD.

D. Geometric Error and Stretch

The geometric error distortion causes straight lines in object space to appear curved in the image. Although curvature of facet images is apparent in the raw IMS data (see Figure 7-3), the mapping calibration procedure should correct this aberration in the datacube remapping. However, several factors could leave geometric errors in the datacube, such as noise in the calibration data and damaged/missing facet images. In the Ronchi ruling datacubes, these factors could result in distortion-like geometric errors that cause the bar features to appear curved.

To test the amount of distortion-like geometric error, the corrected 45^{o} datacube was analyzed. First, a Sobel edge filter was used to identify the edges of bar features in the panchromatic image. For each edge a line was fit and then the coefficient of

determination $R^2$was calculated (see Figure 7-8 left). The average R^2 value for the eleven detected edges was 0.999, which indicated that there is minimal distortion in reconstructed IMS images.

Figure 7-8: (Left) The geometric error test was used to look for distortion-like curvature in the image as well as jagged edges. The blue lines represent the edge of the bar feature and the red is the first-order fitted line. (Right) The width of bar features were calculated for panchromatic images of the horizontal and vertical Ronchi ruling.

We also checked for any difference in magnification between the x- and y-directions of the datacube. Such an anamorphic magnification can stem from errors in the mapping calibration. To check for this error, estimates for the widths of the Ronchi ruling bars in the two orthogonal directions were calculated. First, the datacubes were aligned to the vertical axis. A stretch factor was defined as the normalized ratio between the two measured widths *w*,

$$stretch = \frac{w_{\perp} - w_{\parallel}}{\max\{w_{\perp}, w_{\parallel}\}} \quad (3)$$

The widths were measured in integer pixel units. In the case of the data shown here, the width estimation for both the 0^o and 90^o rulings were 40 pixels, therefore the measured stretch was 0%.

E. Coregistration Test

To further assess the accuracy of datacube reconstruction, another test was developed to measure the spatial coregistration of spectral images. Problems with spatial coregistration of spectral images could be a result of inaccurate mapping calibration or strong chromatic aberration in the system. Taking the flat-fielded Ronchi ruling datacubes, each spectral image was converted to a binary image using a threshold. The overlap between every thresholded spectral image with every other thresholded spectral image was then calculated by summing pixels at each spatial position. A perfect registration was achieved by registering a given spectral image with itself, and this was used as a normalization of the result to give a “percentage" coregistration. Since this was calculated between every pair of spectral images, the result was a matrix.

Figure 7-9 shows the three coregistration matrices obtained from the test and their mean coregistration values. The three matrices correspond to the 0^o, 45^o, and 90^o Ronchi images. Diagonal elements were set to zero and the log of the percentage registration was taken in order to improve visibility of off-diagonal elements. A perfect coregistration of spectral images within a datacube would result in a matrix of zeros. The linear features (dark/bright horizontal and vertical lines seen Figure 7-9a) in the matrices of measured datacubes indicated that the coregistration was lower or higher for some wavelengths

relative to others; or in some cases they revealed individual spectral images that had prominent mapping errors over a few spatial lines. The quantitative result of this test was the mean of all off-diagonal elements, which showed greater than 99% spatial coregistration of all spectral images.

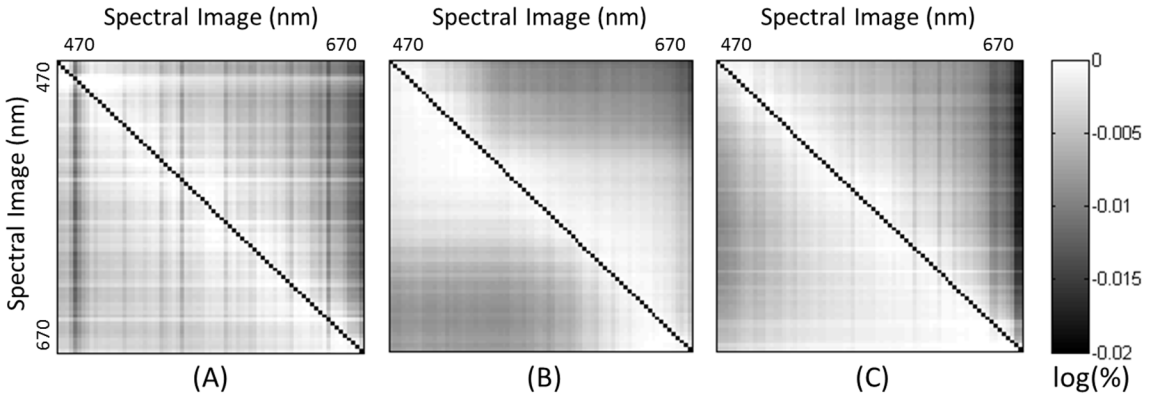

Figure 7-9: Coregistration evaluation results (log scale) indicate the coregistration of spectral images within perpendicular (A), diagonal (B), and parallel (C) Ronchi ruling datacubes. The diagonal elements have been zeroed out to improve visibility of off-diagonal elements. Average coregistration for these datacubes are 99.62, 99.58, and 99.58%, respectively.

F. Spectral Resolution

Spectral resolution is the minimum difference between two wavelengths that a device can distinguish. The spectral resolution of the IMS is influenced by the dispersive properties of prisms/lens array in the system and the pixel sampling. It can be roughly estimated by dividing the spectral range by the number of resolvable bands in the IMS. Our system is designed to sample 200 nm over 25 spectral bands, which results in an

average spectral resolution of 8 nm [91]. The spectral resolution of the IMS, however, varies nonlinearly with wavelength due to nonlinear dispersion of the prisms. It also depends on accurate calibration mapping. Therefore it is important to measure this parameter for several wavelengths throughout the spectral range.

A method for estimating spectral resolution is to measure an object with spectral features smaller than the resolution limit of the system (i. e. a monochromatic source or a lamp with sharp spectral peaks). The convolution of the object with the system response will yield a result which approximates the smallest resolvable feature, measured as the full-width half-maximum (FWHM) of the point spread function (PSF) [98]. To measure spectral resolution in the IMS, several 1-nm FWHM spectral filters were used to illuminate an empty microscope stage. Spectral resolution was tested at five wavelengths: 488.0, 514.5, 532.0, 589.6, and 632.8 nm.

Figure 7-10a shows a matrix of the measured spectral resolution for the 488.0 nm filter over the field of view, which reveals how resolution varies throughout the field. Periodic variation was most likely influenced by defocus of facet images; for detail please see in Figure 7-5a. The hardware error that contributes most to this effect is misalignment/tilt of prisms or lenslets within the array. Figure 7-10b shows the representative spectral response to each filter. The green line represents data from the IMS and the blue line is a spline fit to the IMS data, which was used to estimate the FWHM of the PSF. Figure 7-10c reports the measured and theoretical spectral resolution for each wavelength.

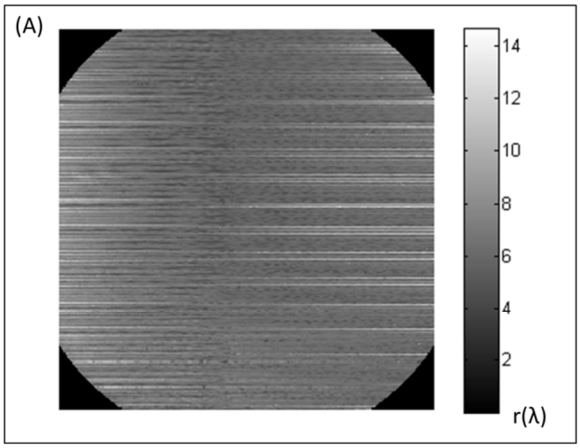

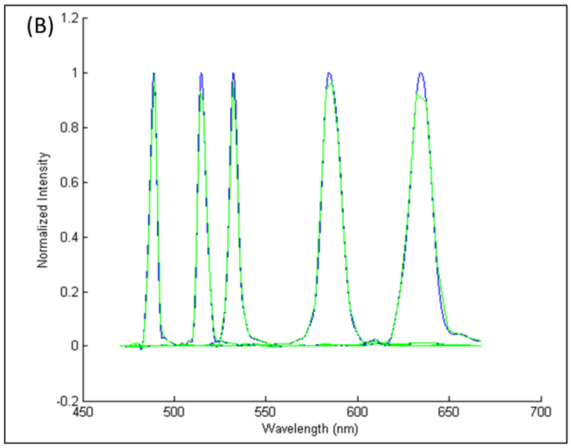

(C)

Wavelength (nm)	*Median*	*Mean ± Standard Deviation*		*Theoretical*
488.0	6.2300	6.4832	± 1.2335	6.2642
514 .5	7.0260	7.5112	± 1.7797	6.9064
532 .0	7.8040	8.4279	± 2.0454	7.8751
589.1	12.601	13.587	± 3.0289	12.166
632.8	15.640	16.430	± 3.4789	15.551

(D)

Mean ± Standard Deviation	
487.8280	± 0.6419
514.9549	± 0.6674
532.1498	± 0.7099
587.4076	± 1.3183
634.4975	± 1.6175

Figure 7-10: (A) The spectral resolution throughout the image shown at 488 nm; grayscale intensity (r) indicates the FWHM of the IMS spectral response. (B) The spectral response at spatial point (150, 150) to each spectral filter; green indicates raw data and blue is the fitted spline. (C) Statistics for spectral resolution at all spatial points in the image. (D) Statistics for spectral accuracy and variability in the image.

G. Spectral Accuracy and Variability

Spectral accuracy and variability were first assessed with the five narrowband filters used for spectral resolution tests. The peak location of the fitted spline curve was calculated for each point in the image. Figure 7-10d reports the measured center wavelength of each filter and the standard deviation for these values throughout all IMS spectra. The mean value of IMS spectra falls within 0.1 to 1.7 nm of the nominal peak wavelength for each filter.

The accuracy and precision of IMS spectra were also measured using five standard plastic transmission filters (Roscolux) and an Ocean Optics Spectrometer (OOS USB-4000). Each filter was placed in the illumination path of the microscope and the transmission spectrum was measured with the IMS and OOS. Each spectrum was divided by the spectrum of the halogen lamp to yield percent transmission. Figure 7-11 shows the results of three spectral measurements. There was low variability throughout the IMS spectra, with standard deviation 0.5 – 4.5%. IMS spectra closely matched the OOS in the shorter wavelength, but had up to 15% error in the red. The discrepancy is a result of decreased spectral resolution found in the longer wavelengths. Similar behavior is described in other hyperspectral imaging systems and there is clearly known methodology for correcting this type of error [99, 100]. The exact correction includes extensive deconvolution procedures, which are out of the scope of this chapter. The level of error is acceptable for the relative spectral measurements required in our current applications [94, 95].

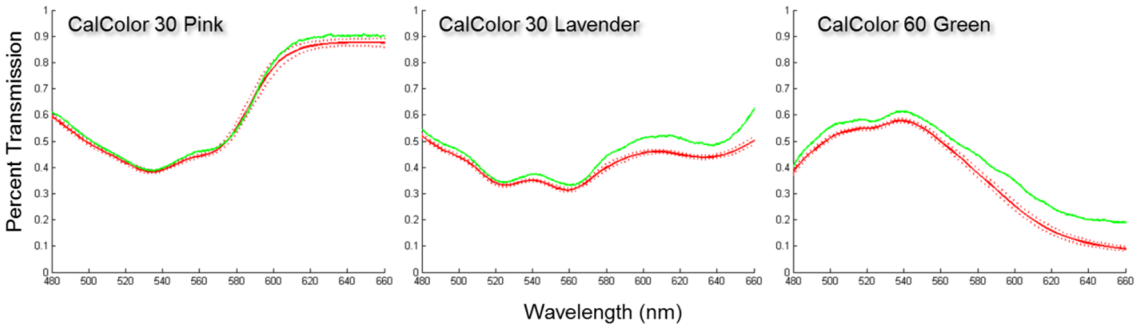

Figure 7-11: Transmission spectra of Roscolux© plastic filters acquired with the IMS and an Ocean Optics Spectrometer. The green line indicates the Ocean Optics Spectrometer results. The red line indicates the mean of IMS spectra at all spatial points with dashes indicating standard deviation.

H. Spatial Resolution, Field of View, and Sampling

The IMS differs from most imaging systems because the image mapping mirror, which exists in an intermediate image plane, redirects image strips to separate locations on the detector. The system therefore inherently samples the x- and y-direction differently. In the *x*-direction, the image is sampled by the discrete number of facets in the image mapper. These facets are projected onto separate locations on the pixel detector, where they are sampled in the *y*-direction by connected pixels. The remapping calibration then determines subpixel intensity values based on these whole pixels using bicubic interpolation. The first goal of this test was to measure the effective spatial sampling of the IMS.

By design, there are 355 (facets) x ~350 samples over the image plane of the IMS datacube. Aberrations introduced by reimaging the image mapping mirror onto the detector can reduce the effective *y*-sampling to below 350 pixels. Also, an accurate mapping calibration is necessary to sample facet images at the correct locations and sampling rate. By analyzing lookup table data, it was found that facets were sampled by a mean of 340.81 +/- 1.21 vertical pixels, which corresponds to 0.97 reconstruction samples/pixel. Therefore, the effective spatial sampling of the IMS is 355 x ~341 integer pixel samples, while the image size is slightly oversampled to 355 x 350 after the mapping calibration.

Given a fixed number of spatial samples, the spatial resolution and FOV of the IMS are primarily dependent on the relay lenses chosen to image the object onto the

image mapper. Depending on the desired application, the spatial samples could be used either to maintain a high spatial resolution with small FOV or to acquire a large FOV with low spatial resolution. Diffraction limited performance of the IMS was already discussed in [92, 93]. Here we present results for qualitative assessment of imaging performance and contrast using a high-resolution 1951 USAF target. The object plane of the IMS was positioned at the Zeiss microscope side port image, which has an NA of 0.01875. A 5X relay objective was used to match two IMS facets to each side port image airy disk diameter. Figure 7-12 shows a panchromatic image of the target acquired with the 5X relay objective and a 40X/0.75NA microscope objective. The Group 9 Element 3 bars are 0.78 µm wide and clearly resolved.

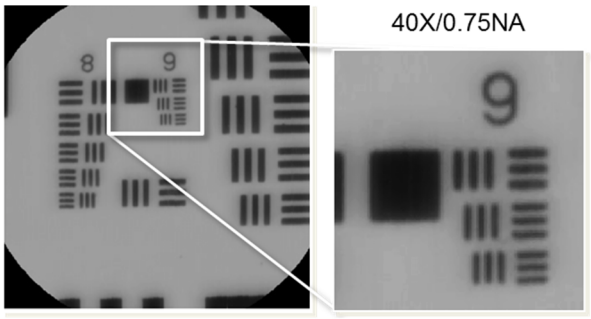

Figure 7-12: The IMS coupled to a microscope was used to image a high-resolution 1951 USAF target. Panchromatic images are shown. Group 9 Element 3 is 0.78 µm wide.

7.5. Motion Artifacts and Spectral Linear Unmixing

The tests shown thus far in this chapter were used to evaluate the performance limits of the IMS. With an understanding of these limits, experiments can be designed for applications that require a fast and dense spatial/spectral dataset. The IMS system has two powerful capabilities that make it useful for demanding spectral imaging applications: (1)

the ability to distinguish objects with similar spectral features, and (2) the ability to record dynamic processes. Here we provide a final qualitative test that evaluates these capabilities.

The IMS was used to measure oxygen saturation *in vivo* during an arterial finger occlusion experiment, following a Rice University IRB-approved normal volunteer protocol. This application particularly benefits from the snapshot capability of IMS because: (1) fast, non-scanning data collection is less susceptible to motion artifacts; and (2) dynamic changes in tissue oxygenation can be recorded and displayed in real-time. With the IMS coupled to a commercial camera lens, images were collected images at 7.2 frames per second and 100 ms exposure of a hand illuminated with a white LED (Thorlabs MCWHL2). At the beginning of the experiment one of the fingers underwent total arterial occlusion using a rubber tourniquet. After one minute the tourniquet was removed and arterial circulation continued. Figure 7-13 presents spectral imaging results from five different time points. The true color images show the occluded finger becoming slightly pale, then reddish and swollen after blood circulation continued. The "ROI Spectra" shows absorption spectra at each time point, which contain characteristic hemoglobin peaks between 500 – 600 nm. Spectra obtained from a region before and after the occlusion were considered deoxy-hemoglobin (Hb) and oxy-hemoglobin (HbO_2) reference spectra, respectively. These spectra contain only slight differences and cannot be quantitatively distinguished with a standard color camera. The IMS, however, can easily differentiate the spectra.

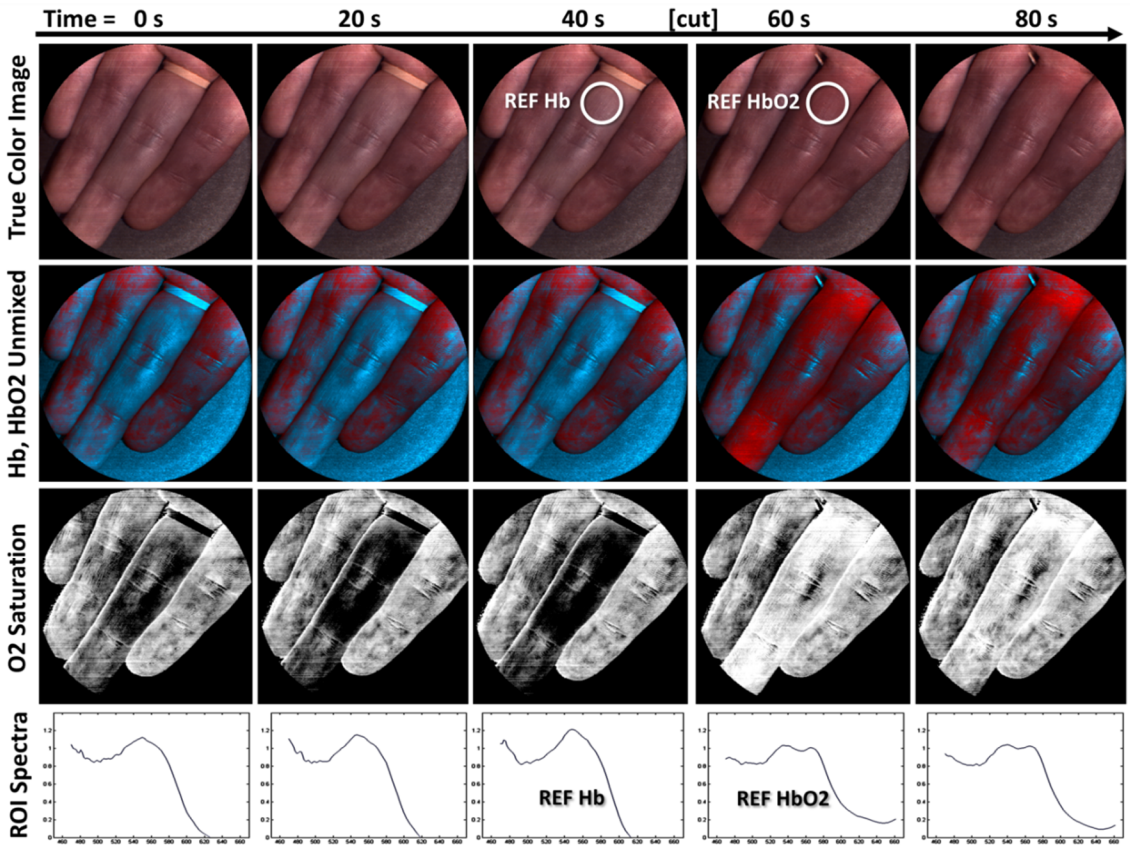

Figure 7-13: To demonstrate the spectral unmixing capability of the IMS for a dynamic application, an arterial finger occlusion experiment was performed. The true color images show the occluded finger becomes pale after 40s without blood flow and then swells with oxygenated blood after the occlusion is removed. Using reference spectra from before and after the occlusion, spectrally unmixed images were created to show distribution of deoxy-hemoglobin (blue) and oxy-hemoglobin (red). Finally, the ratio $HbO_2/(Hb+HbO_2)$ was calculated for each pixel to reveal relative oxygen saturation in the sample.

Using hemoglobin reference spectra, spectrally unmixed images were created to show the relative distribution of Hb and HbO_2 in the hand. Reference [83] describes in general how this linear unmixing is performed. The "Unmixed" images depict maps of the relative reference spectra throughout the experiment. Finally, the Hb and HbO_2

unmixed images were used to visualize relative oxygen saturation in the tissue, defined as:

$$O_2\ Saturation = \frac{[HbO_2]}{[HbO_2]+[Hb]} \quad (4)$$

These images significantly increase contrast between oxygenated and deoxygenated tissue. Such dynamic measurements can be used to determine vascular function during ischemia and reactive hyperemia [101].

Throughout the experiment, movement of the hand had no significant impact on imaging performance. The snapshot nature of the IMS system resulted in images with traditional motion blur seen in standard CCD images, while maintaining coregistered spectral images and accurate spectra, as can be seen in the supplemental movie. Qualitative analyses of results also indicate spectral linear unmixing accurately determined the weighting of reference spectra throughout the experiment. Therefore, this test suggests that the calibrated IMS system is capable of measuring distributions of reference spectra during a dynamic experiment.

7.6. Discussion

This chapter presents the first spatial-spectral calibration and characterization of an Image Mapping Spectrometer. Radiometric tests indicate that the IMS has high optical throughput (~58%) and negligible scattered light. Geometric calibration results show minimal distortion/stretch and high coregistration, which indicates the raw two-

dimensional detector data is accurately remapped to a datacube. Spectral characterization reveals ~6 nm spectral resolution in the blue wavelength region up to ~16 nm in the red. Although broadband spectral tests show up to 15% error in the red wavelength-region, testing with narrowband light indicates spectral bins are accurate to < 2 nm. A high-resolution 1951 USAF target was used to show image quality of the IMS. Finally, an arterial occlusion experiment demonstrated qualitative dynamic imaging performance and spectral unmixing capability. With this new information, a set of specifications now exists to compare this IMS to future IMS devices. These specifications, as well as the description of the tests used to obtain them, is particularly beneficial for end-users to evaluate their systems and design appropriate experiments. Moreover, this work allows for comparison to different hyperspectral imaging modalities.

Although the evaluation tests here address several aspects of datacube quality, the list is not exhaustive. Future work will implement deconvolution techniques to improve spectral calibration. Finally, the optical design, assembly, and fabrication can be improved as more advanced manufacturing procedures become feasible. As hyperspectral imaging hardware, calibration, and data analysis technologies progress, exciting new applications will become possible.

Acknowledgements

The authors would like to thank the NIH for their funding support of this project through R01A124319 and R21EB009186. We would also like to thank Robert Kester and Michal Pawlowski for many useful discussions.

Chapter 8

Multi-modal snapshot spectral imaging for early diagnosis of oral cancer: A pilot study

Oral cancer is a significant global health problem, ranking as the sixth most common cancer worldwide. Optical imaging and spectroscopy have emerged as effective tools for detecting malignant changes associated with oral cancer disease progression. While clinical studies have demonstrated high sensitivity and specificity for early disease detection, current devices either interrogate a small tissue region or have reduced performance for challenging benign conditions such as inflammation, lichen planus, and

hyperkeratosis. To address these clinical challenges, we developed a new optical modality that combines the large field-of-view of widefield imaging with the diagnostic strength of spectroscopy. The portable device is capable of streaming true-color images at 7.2 frames per second and recording both autofluorescence and reflectance spectral datacubes in < 1 second. We describe initial data from the device obtained from normal volunteers and an oral cancer clinical trial.

8.1. Introduction

Oral cancer is a significant global health problem. In the US alone, around 40,000 people will be diagnosed with oral cancer this year and 8,000 will die from the disease. That amount equals approximately one death for every hour of every day. More than half of the individuals diagnosed with oral cancer will die within five years, because it is typically discovered in a later stage when treatment is less effective. Unfortunately, these numbers have not improved for decades.

Although the need for early diagnosis is clear, there are many factors that contribute to delay. The standard screening practice for oral cancer is visual inspection and palpation. During this procedure, clinicians check for abnormal lesions such as leukoplakia and erythroplakia, which appear as white and red patches in the oral cavity [105]. These lesions can be confused with benign conditions such as lichen planus, inflammation, and hyperkeratosis. Therefore, localized oral cancer may appear benign to a physician and could remain unsuspicious until an advanced stage. Lesions that are

suspicious should be biopsied to determine disease status, but the invasiveness of the procedure could lead to hesitation that prolongs diagnosis. Biopsies also take time to process and examine, adding to patient stress and prolonging the time to diagnosis. In addition, the small tissue region being sampled by a biopsy may not represent the highest pathological grade of a heterogeneous tumor [106].

Screening with optical imaging and spectroscopy has the potential to address these clinical challenges. Morphological and biochemical changes occur during cancer progression and these alterations can be detected with non-invasive optical devices. For example, epithelial cancers cause breakdown of stromal collagen as well as changes in NADH/FAD [107]. These alterations can be identified within autofluorescence spectra of the tissue. Cancer also disturbs the vasculature and metabolic activity within the tissue microenvironment, which can affect autofluorescence and reflectance spectra. Several clinical studies have used point spectrometers to detect these changes in autofluorescence and reflectance. These studies found that spectral shape, intensity, and peak can be used to classify oral cavity lesions with 94% sensitivity and 90% specificity [108, 109]. Although point devices can provide an accurate diagnosis, their small sampling area makes it is difficult to screen the entire oral cavity for disease.

Another modality called widefield autofluorescence imaging can screen several centimeters of tissue at one time. When excited with blue light, normal tissue emits a pale green color that can be detected visually or with an image detector array. Dysplastic and cancerous regions that have reduced autofluorescence appear darker [110]. A widefield autofluorescence device called the Velscope is now FDA approved as an aid for oral

cancer detection [105, 111-113]. While the effectiveness of widefield autofluorescence imaging shows great potential for early detection of oral cancers, acquiring additional spectral information may increase specificity when imaging difficult or benign lesions.

An ideal approach for early cancer diagnostics could be to combine widefield imaging with spectral acquisition. This can be accomplished with spectral imaging, which is a new optical modality that collects a full set of spatial and spectral information. A full spatial-spectral "datacube" could enable screening of a large field of view with the added diagnostic strength of spectral information. For example, in reflectance mode, oxy- and deoxy-hemoglobin peaks can be visualized, which enables imaging of vascular activity and oxygen saturation *in vivo* over the entire tissue region [101]. These peaks cannot be distinguished using a conventional three-color CCD. Similarly, autofluorescence changes associated with cancer progression can be better visualized with a full spectrum [109].

Spectral imaging for cancer diagnostics is a relatively new field. Most current imaging spectrometers require a scanning mechanism to sequentially collect spatial and spectral data, which can be time consuming and impractical for some applications. For instance, clinical imaging spectrometers have been built that utilize liquid-crystal tunable filters to collect one spectral image at a time on a CCD sensor [114]. With long exposure times for each spectral image, this acquisition process results in motion blur that reduces accuracy of spatial/spectral features in the datacube.

In this chapter we present a new type of clinical imaging spectrometer that captures all spatial and spectral data simultaneously with high light throughput. The

device can collect data in either autofluorescence or reflectance modes in order to acquire different morphological and biochemical alterations associated with cancer progression. Multimodal datacubes with 350 x 350 spatial x 42 spectral samples are acquired in reflectance and autofluorescence mode with an acquisition time of < 1 second. We assess the diagnostic value of the multimodal device with a pilot study of eleven oral cancer patients. Spectral images and spectra are shown for several normal and abnormal regions and preliminary analysis is presented.

8.2. Methods

Instrumentation

We built a custom multimodal snapshot imaging spectrometer based on a research instrument called the Image Mapping Spectrometer (IMS). The IMS has been used for live cell microscopy [94], animal imaging [95], ophthalmology [115], and endoscopy [72], but never for a multi-patient clinical study. An ideal clinical research device is compact, portable, rugged, non-invasive, and user-friendly. To modify the IMS for these clinical requirements, we mounted the device to a portable tripod, attached a consumer-grade camera lens for wide-field imaging, and developed a software-controlled illumination and acquisition system, as shown in Figure 8-1.

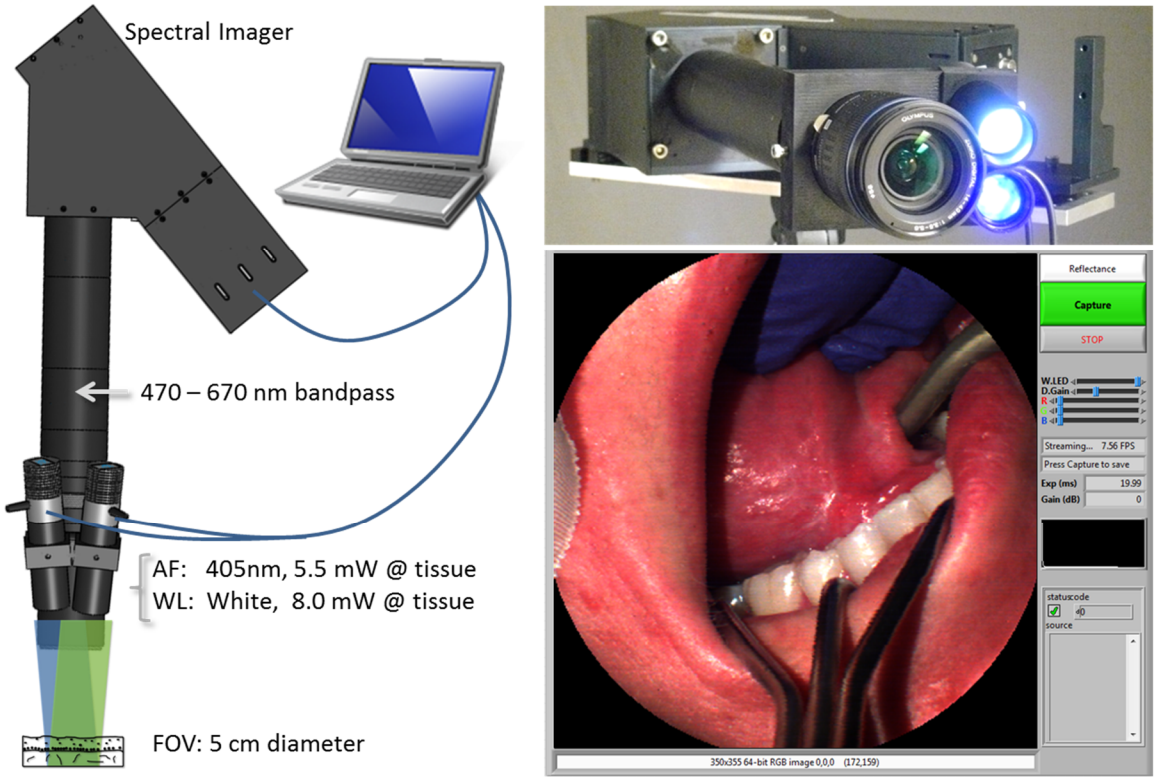

Figure 8-1: The clinical snapshot spectral imager has two mounted LEDs for autofluorescence and reflectance imaging. The device collects 350 x 350 spatial x 42 spectral points simultaneously and is controlled with custom LabVIEW software on a laptop computer.

Although the operational principle and performance of the IMS was previously described [71, 91], we provide a brief list of specifications in Table 8-1. The device is capable of recording 350 x 350 spatial x 42 spectral samples simultaneously at a frame rate up to 7.2 frames per second (FPS). A 3X zoom lens was attached to the existing distal optics of the IMS to obtain a FOV of 3 – 5 cm within the oral cavity. The spectral range was limited to 471 - 667 nm by a bandpass filter placed behind the camera lens. These wavelengths were selected because they contain spectral peaks of autofluorescence

emission (i.e. collagen, NADH, FAD) and reflectance features (i.e. oxy- and deoxy-hemoglobin). To provide reflectance and autofluorescence excitation of the tissue, we used two high-power light emitting diodes (LEDs). A 10W 405nm blue LED was selected for autofluorescence excitation, as this wavelength has been shown to significantly increase contrast of normal/abnormal lesions [110]. A 5W broadband white LED was selected for reflectance imaging. LED intensity was controlled with a USB data acquisition device.

Table 8-1: Specifications for the snapshot imaging spectrometer.

Parameter	Specification
Field of View	~5 cm diameter
Working Distance	10 - 20 cm (adjustable zoom lens)
Spatial Sampling	350 x 355 pixels
Spatial Resolution	~200 µm
Spectral Range	471 – 667 nm
Spectral Sampling	42 pixels
Spectral Resolution	6 – 16 nm
Frame Rate	Up to 7.2 FPS
Pixel Size	7.4 x 14.8 μm^2
Bit Depth	12 bit
Blue LED	405 nm, 10W, 5.5 mW @ tissue
White LED	broadband, 5W, 8 mW @ tissue

The illumination system, camera acquisition, and image display were synchronized using a custom LabVIEW interface. Shown in Figure 8-1, this program allows the user to switch between autofluorescence and reflectance imaging modes, adjust LED intensity, change display gain and color balance, and save datacubes. A real-

time true-color representation of the datacube is also displayed. In order to match execution speed of image display with the 7.2 FPS frame rate of the camera, we chose to display a true-color representation of the datacube using only 3 spectral images. In other words the entire datacube is not used for real-time RGB display, but rather a subset of one spectral image from each of the red, green, and blue wavelength regions. However, the entire datacube is recorded when the user saves an image. The complete acquisition sequence (1) records the reflectance datacube and RGB image, (2) turns the white LED off and blue LED on, (3) increases camera exposure and gain, and (4) records the autofluorescence datacube and RGB image. This automated procedure, which saves a total of 42 x 2 spectral images, takes approximately 1 second.

Calibration

The raw data from the IMS device is a single encoded camera frame that contains all spatial and spectral information. Frame data must be reconstructed into a datacube using a geometric and spatial calibration procedure. Calibration of the device was performed according to the procedure in [71]. In addition, small defects within the optical train of the IMS can make the device less sensitive at localized areas of the datacube. Therefore, the device was flat-field corrected in reflectance mode using a certified reflectance standard (Spectralon) illuminated with a tungsten lamp. The spectra of the tungsten lamp was recorded with a point spectrometer and used to normalize the IMS spectra.

Pilot Clinical Study

The device was first tested on normal volunteers at Rice University under IRB protocol 11-218E entitled "Noninvasive Method for Reflectance and Fluorescence Spectral Imaging of Oral Cavity and Skin in Normal Volunteers Based on the Image Mapping Spectrometer." Clinical images were acquired under Rice University protocol 07-62F and MD Anderson Cancer Center protocol 2006-0673 entitled "Oral Tumor Margin Detection Using Optical Spectroscopy." All tissue was illuminated with settings below safety guidelines for UV and VIS-IR exposure.

Patients having abnormal tissue resected from the oral cavity were considered eligible for the study. Data was collected from consenting patients using several optical devices: (1) the multimodal snapshot imaging spectrometer, (2) a standard widefield autofluorescence camera, and (3) a point spectroscopy device. When possible, data was collected from the lesions as well as a normal tissue site based on clinical impression. After data collection, biopsies were obtained from the lesion and normal site for pathological examination.

8.3. Results

Device Characterization

Although the snapshot imaging spectrometer was thoroughly characterized for other applications [71], we evaluated the device for spatial resolution, color balance, and excitation light rejection. Using a 1951 USAF resolution target we found the device could

resolve 200 µm features. A Macbeth ColorChecker chart was used to qualitatively assess color balance of reconstructed true-color datacube images. Rejection of excitation light was verified with a quartz disc, which showed less than 1:10 fluorescence ratio compared to the autofluorescence of normal tissue.

We also measured the time to acquire a sequence of reflectance and autofluorescence datacubes. This metric is important because movement of the patient, clinician, or researcher during a long acquisition can cause motion blur or misregistration of spectral images. The device was set to capture reflectance and autofluorescence datacubes at 100 ms and 500 ms exposure, respectively. It took approximately 300 ms to adjust camera exposure/gain settings and to change white/blue LED intensities. Therefore the total time to collect all multimodal spectral datacubes was < 1 second. Spectral images within each datacube had > 99% coregistration, but sometimes a small spatial shift occurred between sequential reflectance/autofluorescence acquisitions.

Oral Cavity Imaging Results

Data was collected from normal volunteers and eleven patients using the snapshot imaging spectrometer. Reflectance datacubes were acquired with an exposure setting of 100 ms and gain of 0 dB. Autofluorescence datacubes were acquired with an exposure setting of 500 ms and a gain of 20 dB. Figure 8-2 shows reflectance datacube spectral images from the lower lip of a normal volunteer. A plot of absorbance of the tissue reveals characteristics oxy-hemoglobin peaks. In addition, vascularity patterns can be visualized at different depths corresponding to wavelength. This effect is caused by the

dependence of wavelength on light penetration depth into tissue, which is primarily effected by the absorption properties of water.

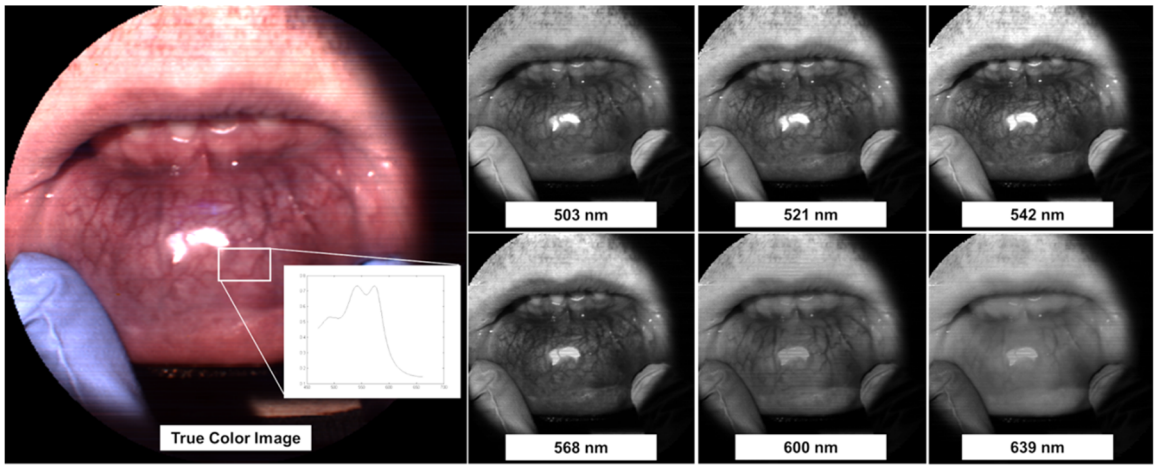

Figure 8-2: Reflectance spectral images from the lower lip show vasculature at different depths.

Figure 8-3 shows images from an abnormal tissue site from a patient. Figure 8-3A/B are true-color images that were reconstructed from the reflectance and autofluorescence datacubes, respectively. Figure 8-3C is an image from the standard widefield autofluorescence camera, which reveals similar autofluorescence as the snapshot imaging spectrometer. Figure 8-3D shows a suspicious region determined by calculating the red/green ratio of the true-color datacube reconstruction.

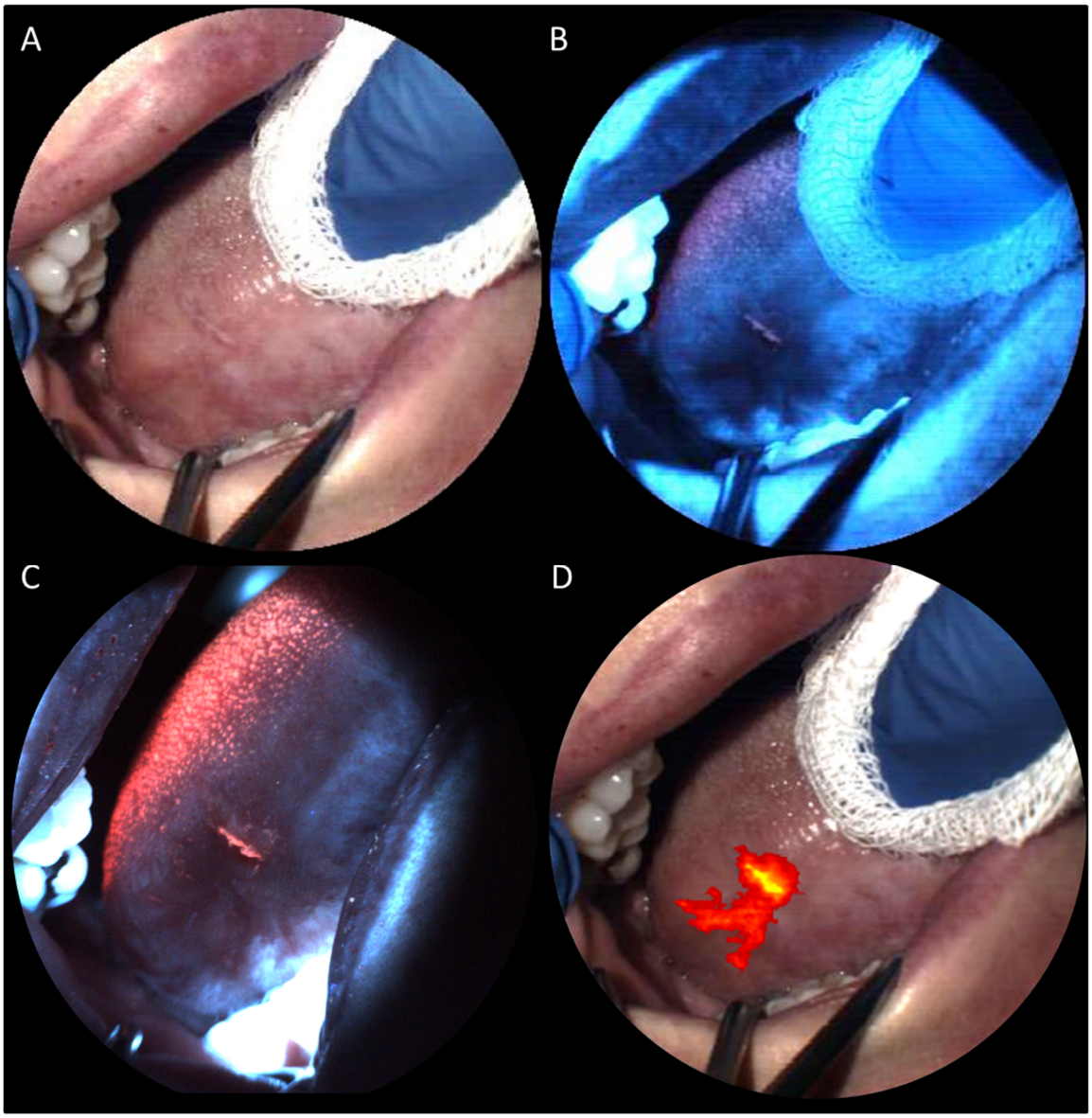

Figure 8-3: Images from a patient diagnosed with oral cancer. Reflectance (A) and autofluorescence (B) true-color images from the snapshot imaging spectrometer show an abnormal region of tissue. An image from a standard widefield autofluorescence camera (C) shows similar autofluorescence distribution. Using the red/green ratio, an abnormal tissue region can be identified (D). Standard widefield image from Richard Schwarz.

Figure 8-4 shows reflectance and autofluorescence spectra from different tissue regions in Figure 8-3, which were obtained in real-time by the snapshot imaging spectrometer. Compared to the spectra of normal tissue, abnormal and keratinized tissue exhibits a loss of overall reflectance intensity. Keratinized tissue also shows diminished oxy-hemoglobin peaks. Autofluorescence spectra of abnormal tissue show an overall decrease in intensity, a relative decrease in blue/green intensity, and increase in red intensity. Keratinized tissue shows significantly increased red autofluorescence, which is most likely from porphyrins in the tissue.

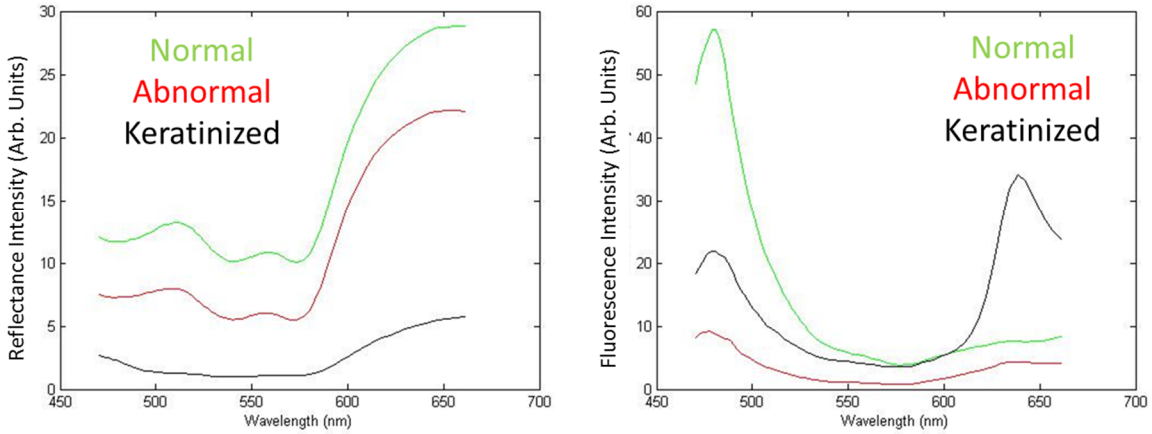

Figure 8-4: Reflectance and autofluorescence spectra from different tissue regions.

8.4. Discussion

This work described a new optical modality for oral cancer imaging. A multimodal snapshot imaging spectrometer was constructed and is capable of streaming true-color images at 7.2 FPS and saving reflectance and autofluorescence datacubes in <

1 second. The device was used to acquire spatial and spectral data *in vivo* from normal volunteers and eleven oral cancer patients. Samples images and spectra are shown for normal and abnormal regions of tissue.

While this chapter demonstrates a new optical modality suitable for clinical studies, the work would benefit from further data analysis. Information such as number of normal and abnormal sites, disease pathology, and anatomical site will be tabulated. Pathology results and clinical impression will be used as a training set for a diagnostic algorithm. We will perform datacube analysis using algorithms such as k-means clustering, spectral unmixing, linear discriminant analysis, and principal component analysis. The result of this work will be a novel device and algorithm for point-of-care early oral cancer diagnosis.

Acknowledgements

This work was supported by research grants R01A124319 and R21EB009186.

Chapter 9

Conclusion

In summary, this dissertation has presented several new optical imaging techniques for cancer diagnosis. The work details improvements in a two-part cancer detection procedure, which uses widefield imaging to survey a large region of tissue, and then high-resolution endomicroscopy to provide the final diagnosis.

The first half of the dissertation describes four improvements to endomicroscopy. An algorithm to expand the effective field-of-view of endomicroscopes was developed and validated on several tissue specimens. While this technique was implemented on a fiber-bundle based endomicroscope, it can be applied to any endomicroscopy device. Next, two methods to improve axial response were described. These low-cost, user-friendly devices were constructed and compared. The solutions provide better visualization of glandular tissue, increased contrast, and can be used to image beneath the

tissue surface. Finally, a technique to improve lateral resolution of endomicroscopes was presented. This work is useful when small subcellular features need to be visualized and for imaging tissue that is difficult to access. Additionally, these devices serve as a platform for imaging with miniature objective lenses. High-quality, low-cost miniature optics can be used to further increase lateral resolution and depth sectioning.

The second half of the dissertation describes the development of a new widefield imaging modality. A description of the operational principle, calibration, and characterization of the spectral imaging device was presented. Next, the technique was configured to acquire widefield spectral images in autofluorescence and reflectance modes for oral cavity imaging. The device was tested on several tissue specimens and used to acquire data from eleven patients with oral cancer. Data acquired from this technique provides spectral information that can be correlated to disease progression. Results from this work could enable identification of key spectral imaging features that can be used to discriminate cancer from benign conditions such as lichen planus, hyperkeratosis, and inflammation. The future of this work includes further spectral images analysis and larger clinical studies.

This work provides advancements to widefield and high resolution imaging for cancer diagnostics. Further research should aim to combine these techniques into a single system used for two-step “bi-FOV” detection. This work could impact areas of research besides cancer diagnosis. Improved optical imaging techniques can be used for detection of other diseases and for *in vivo* animal studies.

References

1. N. Bedard, M. Pierce, A. El-Nagger, S. Anandasabapathy, A. Gillenwater, and R. Richards-Kortum, "Emerging roles for multimodal optical imaging in early cancer detection: a global challenge.," Technol Cancer Res Treat 9, 211-217 (2010).

2. American Cancer Society, "Cancer Facts and Figures 2007," (Atlanta, 2007).

3. S. Franceschi, E. Bidoli, R. Herrero, and N. Munoz, "Comparison of cancers of the oral cavity and pharynx worldwide: etiological clues," Oral oncology 36, 106-115 (2000).

4. F. Kamangar, G. M. Dores, and W. F. Anderson, "Patterns of cancer incidence, mortality, and prevalence across five continents: defining priorities to reduce cancer disparities in different geographic regions of the world," J Clin Oncol 24, 2137-2150 (2006).

5. L. Ries, D. Harkins, and M. Krapcho, "SEER Cancer Statistics Review, 1975-2003," (National Cancer Institute, Bethesda, 2006).

6. B. W. Neville, and T. A. Day, "Oral cancer and precancerous lesions," CA: a cancer journal for clinicians 52, 195-215 (2002).

7. A. Mashberg, and A. M. Samit, "Early detection, diagnosis, and management of oral and oropharyngeal cancer," CA: a cancer journal for clinicians 39, 67-88 (1989).

8. American Cancer Society, "Detailed Guide: What Is Cancer?," (2006).

9. D. Hanahan, and R. A. Weinberg, "The hallmarks of cancer," Cell 100, 57-70 (2000).

10. K. Sokolov, D. Nida, M. Descour, A. Lacy, M. Levy, B. Hall, S. Dharmawardhane, A. Ellington, B. Korgel, and R. Richards-Kortum, "Molecular optical imaging of therapeutic targets of cancer," Advances in cancer research 96, 299-344 (2007).

11. M. C. Skala, G. M. Palmer, C. Zhu, Q. Liu, K. M. Vrotsos, C. L. Marshek-Stone, A. Gendron-Fitzpatrick, and N. Ramanujam, "Investigation of fiber-optic probe designs for optical spectroscopic diagnosis of epithelial pre-cancers," Lasers in surgery and medicine 34, 25-38 (2004).

12. M. Rahman, M. Abd-El-Barr, V. Mack, T. Tkaczyk, K. Sokolov, R. Richards-Kortum, and M. Descour, "Optical imaging of cervical pre-cancers with structured illumination: an integrated approach," Gynecologic oncology 99, S112-115 (2005).

13. A. L. Carlson, and R. Richards-Kortum, "Epithelial pre-cancers and cancers, optical technologies for detection and diagnosis of," Wiley Encyclopedia of Biomedical Engineering (2006).

14. K. Sokolov, J. Aaron, B. Hsu, D. Nida, A. Gillenwater, M. Follen, C. MacAulay, K. Adler-Storthz, B. Korgel, M. Descour, R. Pasqualini, W. Arap, W. Lam, and R. Richards-Kortum, "Optical systems for in vivo molecular imaging of cancer," Technology in cancer research & treatment 2, 491-504 (2003).

15. American Cancer Society, "Testing Biopsy and Cytology Specimens for Cancer," (2007).

16. P. Speight, "Update on oral epithelial dysplasia and progression to cancer," Head and Neck Pathol 1, 61-66 (2007).

17. R. Weissleder, and M. J. Pittet, "Imaging in the era of molecular oncology," Nature 452, 580-589 (2008).

18. T. F. Massoud, and S. S. Gambhir, "Integrating noninvasive molecular imaging into molecular medicine: an evolving paradigm," Trends Mol Med 13, 183-191 (2007).

19. M. B. Barton, M. Frommer, and J. Shafiq, "Role of radiotherapy in cancer control in low-income and middle-income countries," Lancet Oncol 7, 584-595 (2006).

20. H. Tunstall-Pedoe, "Preventing Chronic Diseases. A Vital Investment: WHO Global Report. Geneva: World Health Organization, 2005. pp 200. CHF 30.00. ISBN 92 4 1563001. Also published on http://www.who.int/chp/chronic_disease_report/en," Int J Epidemiol (2006).

21. L. A. Jones, J. A. Chilton, R. A. Hajek, N. K. Iammarino, and L. Laufman, "Between and within: international perspectives on cancer and health disparities," J Clin Oncol 24, 2204-2208 (2006).

22. M. T. Halpern, E. M. Ward, A. L. Pavluck, N. M. Schrag, J. Bian, and A. Y. Chen, "Association of insurance status and ethnicity with cancer stage at diagnosis for 12 cancer sites: a retrospective analysis," Lancet Oncol 9, 222-231 (2008).

23. C. DeNavas-Walt, B. Proctor, and C. Lee, "Income, poverty and health insurance coverage in the Univeted States:2006," US Census Bureau (2007).

24. C. H. Contag, "In vivo pathology: seeing with molecular specificity and cellular resolution in the living body," Annu Rev Pathol 2, 277-305 (2007).

25. M. C. Pierce, D. J. Javier, and R. Richards-Kortum, "Optical contrast agents and imaging systems for detection and diagnosis of cancer," Int J Cancer 123, 1979-1990 (2008).

26. P. Boyle, and C. Levin, "World cancer report," World Health Organization (2008).

27. W. L. Curvers, R. Singh, L. M. Song, H. C. Wolfsen, K. Ragunath, K. Wang, M. B. Wallace, P. Fockens, and J. J. Bergman, "Endoscopic tri-modal imaging for detection of early neoplasia in Barrett's oesophagus: a multi-centre feasibility study using high-resolution endoscopy, autofluorescence imaging and narrow band imaging incorporated in one endoscopy system," Gut 57, 167-172 (2008).

28. A. McWilliams, C. MacAulay, A. F. Gazdar, and S. Lam, "Innovative molecular and imaging approaches for the detection of lung cancer and its precursor lesions," Oncogene 21, 6949-6959 (2002).

29. N. Ikeda, H. Honda, A. Hayashi, J. Usuda, Y. Kato, M. Tsuboi, T. Ohira, T. Hirano, H. Kato, H. Serizawa, and Y. Aoki, "Early detection of bronchial lesions using newly developed videoendoscopy-based autofluorescence bronchoscopy," Lung Cancer 52, 21-27 (2006).

30. J. Q. Brown, L. G. Wilke, J. Geradts, S. A. Kennedy, G. M. Palmer, and N. Ramanujam, "Quantitative optical spectroscopy: A robust tool for direct measurement of breast cancer oxygenation and total hemoglobin content in vivo," Cancer Research (Accepted 2008).

31. A. L. Polglase, W. J. McLaren, S. A. Skinner, R. Kiesslich, M. F. Neurath, and P. M. Delaney, "A fluorescence confocal endomicroscope for in vivo microscopy of the upper- and the lower-GI tract," Gastrointest Endosc 62, 686-695 (2005).

32. A. Tanbakuchi, A. Rouse, J. Udovich, K. Hatch, and F. Gmitro, "A clinical confocal microlaparoscope for real-time in vivo optical biopsies," J Biomed Opt (2009).

33. D. S. Gareau, Y. Li, B. Huang, Z. Eastman, K. S. Nehal, and M. Rajadhyaksha, "Confocal mosaicing microscopy in Mohs skin excisions: feasibility of rapid surgical pathology," J Biomed Opt 13, 054001 (2008).

34. S. Lam, B. Standish, C. Baldwin, A. McWilliams, J. leRiche, A. Gazdar, A. I. Vitkin, V. Yang, N. Ikeda, and C. MacAulay, "In vivo optical coherence tomography imaging of preinvasive bronchial lesions," Clin Cancer Res 14, 2006-2011 (2008).

35. D. K. Walmer, D. Merisier, E. Littman, G. Rodriguez, N. Venero, M. Henderson, D. Katz, and R. Edwards, "Portable colposcopy in low-resource settings," J Acquir Immune Defic Syndr 37 Suppl 3, S167-170 (2004).

36. J. L. Winkler, V. D. Tsu, A. Bishop, R. Scott, and J. W. Sellors, "Confirmation of cervical neoplasia using a hand-held, lighted magnification device," Int J Gynaecol Obstet 81, 35-40 (2003).

37. P. M. Lane, T. Gilhuly, P. Whitehead, H. Zeng, C. F. Poh, S. Ng, P. M. Williams, L. Zhang, M. P. Rosin, and C. E. MacAulay, "Simple device for the direct visualization of oral-cavity tissue fluorescence," J Biomed Opt 11, 024006 (2006).

38. M. Rahman, P. Chaturvedi, A. M. Gillenwater, and R. Richards-Kortum, "Low-cost, multimodal, portable screening system for early detection of oral cancer," J Biomed Opt 13, 030502 (2008).

39. T. J. Muldoon, M. C. Pierce, D. L. Nida, M. D. Williams, A. Gillenwater, and R. Richards-Kortum, "Subcellular-resolution molecular imaging within living tissue by fiber microendoscopy," Opt Express 15, 16413-16423 (2007).

40. P. Boyle, "The globalisation of cancer," Lancet 368, 629-630 (2006).

41. S. J. Goldie, L. Gaffikin, J. D. Goldhaber-Fiebert, A. Gordillo-Tobar, C. Levin, C. Mahe, and T. C. Wright, "Cost-effectiveness of cervical-cancer screening in five developing countries," N Engl J Med 353, 2158-2168 (2005).

42. D. Roblyer, C. Kurachi, V. Stepanek, M. D. Williams, A. K. El-Naggar, J. J. Lee, A. M. Gillenwater, and R. Richards-Kortum, "Objective detection and delineation of oral neoplasia using autofluorescence imaging," Cancer Prev Res (Phila Pa) 2, 423-431 (2009).

43. B. M. Kuehn, "Poverty shift may burden health system," Jama 297, 1047-1048 (2007).

44. N. Thekkek, and R. Richards-Kortum, "Optical imaging for cervical cancer detection: solutions for a continuing global problem," Nat Rev Cancer (2008).

45. B. A. Flusberg, E. D. Cocker, W. Piyawattanametha, J. C. Jung, E. L. Cheung, and M. J. Schnitzer, "Fiber-optic fluorescence imaging.," Nat Methods 2, 941-950 (2005).

46. K. E. Loewke, D. B. Camarillo, C. A. Jobst, and J. K. Salisbury, "Real-time image mosaicing for medical applications.," Stud Health Technol Inform 125, 304-309 (2007).

47. M. L. Hearp, A. M. Locante, M. Ben-Rubin, R. Dietrich, and O. David, "Validity of sampling error as a cause of noncorrelation.," Cancer 111, 275-279 (2007).

48. V. Becker, T. Vercauteren, C. H. von Weyhern, C. Prinz, R. M. Schmid, and A. Meining, "High-resolution miniprobe-based confocal microscopy in combination with video mosaicing (with video)." Gastrointest Endosc 66, 1001-1007 (2007).

49. T. Vercauteren, A. Perchant, G. Malandain, X. Pennec, and N. Ayache, "Robust mosaicing with correction of motion distortions and tissue deformations for in vivo fibered microscopy.," Medical image analysis 10, 673-692 (2006).

50. K. Wu, J. J. Liu, W. Adams, G. A. Sonn, K. E. Mach, Y. Pan, A. H. Beck, K. C. Jensen, and J. C. Liao, "Dynamic real-time microscopy of the urinary tract using confocal laser endomicroscopy.," Urology 78, 225-231 (2011).

51. T. Vercauteren, A. Meining, F. Lacombe, and A. Perchant, "Real time autonomous video image registration for endomicroscopy: fighting the compromises," in *Three-Dimensional and Multidimensional Microscopy: Image Acquisition and Processing XV*(International Society for Optical Engineering, San Jose, CA, USA, 2008).

52. K. E. Loewke, D. B. Camarillo, W. Piyawattanametha, M. J. Mandella, C. H. Contag, S. Thrun, and J. K. Salisbury, "In vivo micro-image mosaicing.," IEEE transactions on bio-medical engineering 58, 159-171 (2011).

53. T. J. Muldoon, M. C. Pierce, D. L. Nida, M. D. Williams, A. Gillenwater, and R. Richards-Kortum, "Subcellular-resolution molecular imaging within living tissue by fiber microendoscopy.," Optics express 15, 16413-16423 (2007).

54. T. J. Muldoon, D. Roblyer, M. D. Williams, V. M. Stepanek, R. Richards-Kortum, and A. M. Gillenwater, "Noninvasive imaging of oral neoplasia with a high-resolution fiber-optic microendoscope.," Head Neck (2011).

55. M. Pierce, D. Yu, and R. Richards-Kortum, "High-resolution fiber-optic microendoscopy for in situ cellular imaging.," J Vis Exp (2011).

56. M. Elter, S. Rupp, and C. Winter, "Physically motivated reconstruction of fiberscopic images," in *18th International Conference on Pattern Recognition*(Hong Kong, 2006), pp. 599-602.

57. B. L. Luck, K. D. Carlson, A. C. Bovik, and R. R. Richards-Kortum, "An image model and segmentation algorithm for reflectance confocal images of in vivo cervical tissue.," IEEE Trans Image Process 14, 1265-1276 (2005).

58. S. Rupp, C. Winter, and M. Elter, "Evaluation of spatial interpolation strategies for the removal of comb-structure in fiber-optic images " in *31st Annual International*

Conference of the IEEE EMBS(Minneapolis, Minnesota, USA, 2009), pp. 3677-3680.

59. P. Soille, *Morphological Image Analysis: Principles and Applications* (Springer, 1999).

60. M. Guizar-Sicairos, S. T. Thurman, and J. R. Fienup, "Efficient subpixel image registration algorithms.," Optics letters 33, 156-158 (2008).

61. E. Laemmel, M. Genet, G. Le Goualher, A. Perchant, J. F. Le Gargasson, and E. Vicaut, "Fibered confocal fluorescence microscopy (Cell-viZio) facilitates extended imaging in the field of microcirculation. A comparison with intravital microscopy.," J Vasc Res 41, 400-411 (2004).

62. C. Liang, M. Descour, K. B. Sung, and R. Richards-Kortum, "Fiber confocal reflectance microscope (FCRM) for in-vivo imaging.," Optics express 9, 821-830 (2001).

63. W. Göbel, J. N. Kerr, A. Nimmerjahn, and F. Helmchen, "Miniaturized two-photon microscope based on a flexible coherent fiber bundle and a gradient-index lens objective.," Optics letters 29, 2521-2523 (2004).

64. L. Gao, N. Bedard, N. Hagen, R. T. Kester, and T. S. Tkaczyk, "Depth-resolved image mapping spectrometer (IMS) with structured illumination," Optics express 19, 17439-17452 (2011).

65. M. Kyrish, R. Kester, R. Richards-Kortum, and T. Tkaczyk, "Improving spatial resolution of a fiber bundle optical biopsy system," Proceedings of SPIE 7558, 755807 (2010).

66. A. L. Polglase, W. J. McLaren, S. A. Skinner, R. Kiesslich, M. F. Neurath, and P. M. Delaney, "A fluorescence confocal endomicroscope for in vivo microscopy of the upper- and the lower-GI tract.," Gastrointest Endosc 62, 686-695 (2005).

67. H. J. Shin, M. C. Pierce, D. Lee, H. Ra, O. Solgaard, and R. Richards-Kortum, "Fiber-optic confocal microscope using a MEMS scanner and miniature objective lens.," Optics express 15, 9113-9122 (2007).

68. G. J. Tearney, R. H. Webb, and B. E. Bouma, "Spectrally encoded confocal microscopy.," Optics letters 23, 1152-1154 (1998).

69. C. Boudoux, S. Yun, W. Oh, W. White, N. Iftimia, M. Shishkov, B. Bouma, and G. Tearney, "Rapid wavelength-swept spectrally encoded confocal microscopy.," Optics express 13, 8214-8221 (2005).

70. M. Strupler, E. D. Montigny, D. Morneau, and C. Boudoux, "Rapid spectrally encoded fluorescence imaging using a wavelength-swept source.," Optics letters 35, 1737-1739 (2010).

71. N. Bedard, N. Hagen, L. Gao, and T. Tkaczyk, "Image mapping spectrometry: calibration and characterization," Optical Engineering (2012 (Submitted)).

72. R. T. Kester, N. Bedard, L. Gao, and T. S. Tkaczyk, "Real-time snapshot hyperspectral imaging endoscope," Journal of biomedical optics 16, 056005 (2011).

73. D. C. Leiner, and R. Prescott, "Correction of chromatic aberrations in GRIN endoscopes.," Applied optics 22, 383-386 (1983).

74. M. Kyrish, U. Utzinger, M. R. Descour, B. K. Baggett, and T. S. Tkaczyk, "Ultra-slim plastic endomicroscope objective for non-linear microscopy.," Optics express 19, 7603-7615 (2011).

75. T. Collier, M. Guillaud, M. Follen, A. Malpica, and R. Richards-Kortum, "Real-time reflectance confocal microscopy: comparison of two-dimensional images and three-dimensional image stacks for detection of cervical precancer.," Journal of biomedical optics 12, 024021 (2007).

76. M. A. Neil, R. Juskaitis, and T. Wilson, "Method of obtaining optical sectioning by using structured light in a conventional microscope.," Optics letters 22, 1905-1907 (1997).

77. N. Bozinovic, C. Ventalon, T. Ford, and J. Mertz, "Fluorescence endomicroscopy with structured illumination.," Optics express 16, 8016-8025 (2008).

78. N. Hagen, L. Gao, and T. S. Tkaczyk, "Quantitative sectioning and noise analysis for structured illumination microscopy.," Optics express 20, 403-413 (2012).

79. J. Oke, J. Cohen, M. Carr, J. Cromer, A. Dingizian, F. Harris, S. Labrecque, R. Lucinio, and W. Schaal, "The Keck Low-Resolution Imaging Spectrometer," Publications of the Astronomical Society of the Pacific 107 (1995).

80. G. Vane, R. Green, T. Chrien, H. Enmark, E. Hansen, and W. Porter, "The airborne visible/infrared imaging spectrometer (AVIRIS)," Remote Sensing of Environment 44 (1993).

81. A. A. Gowen, C. P. O'Donnell, P. J. Cullen, G. Downey, and J. M. Frias, "Hyperspectral imaging - an emerging process analytical tool for food quality and safety control," Trends in Food Science & Technology 18 (2007).

82. T. Zimmermann, J. Rietdorf, and R. Pepperkok, "Spectral imaging and its applications in live cell microscopy," FEBS letters 546, 87-92 (2003).

83. M. E. Dickinson, G. Bearman, S. Tille, R. Lansford, and S. E. Fraser, "Multi-spectral imaging and linear unmixing add a whole new dimension to laser scanning fluorescence microscopy.," Biotechniques 31, 1272, 1274-1276, 1278 (2001).

84. H. R. Morris, C. C. Hoyt, and P. J. Treado, "Imaging spectrometers for fluorescence and Raman microscopy: acousto-optic and liquid-crystal-tunable filters," Applied spectroscopy 48, 857-866 (1994).

85. M. Descour, and E. Dereniak, "Computed-tomography imaging spectrometer: experimental calibration and reconstruction results," Applied optics 34, 4817-4826 (1995).

86. T. Okamoto, and I. Yamaguchi, "Simultaneous acquisition of spectral image information," Optics letters 16, 1277-1279 (1991).

87. A. Wagadarikar, R. John, R. Willett, and D. Brady, "Single disperser design for coded aperture snapshot spectral imaging," Applied optics 47, B44-51 (2008).

88. S. Vivès, and E. Prieto, "Original image slicer designed for integral field spectroscopy with the near-infrared spectrograph for the James Webb Space Telescope," Opt. Eng. 45, 093001 (2006).

89. H. Matsuoka, Y. Kosai, M. Saito, N. Takeyama, and H. Suto, "Single-cell viability assessment with a novel spectro-imaging system.," J Biotechnol 94, 299-308 (2002).

90. A. Bodkin, A. I. Sheinis, and A. Norton, "Hyperspectral imaging systems," U. S. Patent, ed. (2006).

91. L. Gao, R. T. Kester, N. Hagen, and T. S. Tkaczyk, "Snapshot Image Mapping Spectrometer (IMS) with high sampling density for hyperspectral microscopy," Optics express 18, 14330-14344 (2010).

92. L. Gao, R. T. Kester, and T. S. Tkaczyk, "Compact Image Slicing Spectrometer (ISS) for hyperspectral fluorescence microscopy," Optics express 17, 12293-12308 (2009).

93. R. T. Kester, L. Gao, and T. S. Tkaczyk, "Development of image mappers for hyperspectral biomedical imaging applications," Applied optics 49, 1886-1899 (2010).

94. L. Gao, A. Elliot, R. Kester, N. Hagen, D. Piston, and T. Tkaczyk, "Real-time hyperspectral imaging of pancreatic β-cell dynamics with Image Mapping Spectrometer (IMS)," in *Bio-optics: Design and Application*(OSA Technical Digest, 2011).

95. N. Hagen, N. Bedard, A. Mazhar, S. Konecky, B. Tromberg, and T. Tkaczyk, "Spectrally-resolved imaging of dynamic turbid media," (Proc. SPIE 7892, 789206, 2011).

96. R. Keys, "Cubic convolution interpolation for digital image processing," Acoustics, Speech and Signal Processing, IEEE Transactions on 29, 1153 - 1160 (1981).

97. J. Seibert, J. Boone, and K. Lindfors, "Flat-field correction technique for digital detectors," in *Medical Imaging 1998: Physics of Medical Imaging*(Proc. SPIE 3336, San Diego, CA, 1998).

98. R. Gomez, "Hyperspectral imaging: a useful technology for transportation analysis," Opt Eng 41, 2137-2143 (2002).

99. M. Burmen, F. Pernus, and B. Likar, "Spectral characterization of near-infrared acousto-optic tunable filter (AOTF) hyperspectral imaging systems using standard calibration materials," Applied spectroscopy 65, 393-401 (2011).

100. J. Katrašnik, F. Pernuš, and B. Likar, "Deconvolution in acousto-optical tunable filter spectrometry.," Applied spectroscopy 64, 1265-1273 (2010).

101. K. J. Zuzak, M. D. Schaeberle, E. N. Lewis, and I. W. Levin, "Visible reflectance hyperspectral imaging: characterization of a noninvasive, in vivo system for determining tissue perfusion.," Anal Chem 74, 2021-2028 (2002).

102. A. C. Society, "Cancer Facts and Figures 2007," (Atlanta, 2007).

103. S. Franceschi, E. Bidoli, R. Herrero, and N. Muñoz, "Comparison of cancers of the oral cavity and pharynx worldwide: etiological clues.," Oral Oncol 36, 106-115 (2000).

104. H. K. Weir, M. J. Thun, B. F. Hankey, L. A. Ries, H. L. Howe, P. A. Wingo, A. Jemal, E. Ward, R. N. Anderson, and B. K. Edwards, "Annual report to the nation on the status of cancer, 1975-2000, featuring the uses of surveillance data for cancer prevention and control.," J Natl Cancer Inst 95, 1276-1299 (2003).

105. P. M. Lane, T. Gilhuly, P. Whitehead, H. Zeng, C. F. Poh, S. Ng, P. M. Williams, L. Zhang, M. P. Rosin, and C. E. MacAulay, "Simple device for the direct visualization of oral-cavity tissue fluorescence.," Journal of biomedical optics 11, 024006 (2006).

106. D. P. SLAUGHTER, H. W. SOUTHWICK, and W. SMEJKAL, "Field cancerization in oral stratified squamous epithelium; clinical implications of multicentric origin.," Cancer 6, 963-968 (1953).

107. I. Pavlova, M. Williams, A. El-Naggar, R. Richards-Kortum, and A. Gillenwater, "Understanding the biological basis of autofluorescence imaging for oral cancer detection: high-resolution fluorescence microscopy in viable tissue.," Clin Cancer Res 14, 2396-2404 (2008).

108. R. A. Schwarz, W. Gao, D. Daye, M. D. Williams, R. Richards-Kortum, and A. M. Gillenwater, "Autofluorescence and diffuse reflectance spectroscopy of oral epithelial tissue using a depth-sensitive fiber-optic probe.," Applied optics 47, 825-834 (2008).

109. R. A. Schwarz, W. Gao, C. Redden Weber, C. Kurachi, J. J. Lee, A. K. El-Naggar, R. Richards-Kortum, and A. M. Gillenwater, "Noninvasive evaluation of oral lesions using depth-sensitive optical spectroscopy.," Cancer 115, 1669-1679 (2009).

110. D. Roblyer, C. Kurachi, V. Stepanek, M. D. Williams, A. K. El-Naggar, J. J. Lee, A. M. Gillenwater, and R. Richards-Kortum, "Objective detection and delineation of oral neoplasia using autofluorescence imaging.," Cancer Prev Res (Phila) 2, 423-431 (2009).

111. C. F. Poh, L. Zhang, D. W. Anderson, J. S. Durham, P. M. Williams, R. W. Priddy, K. W. Berean, S. Ng, O. L. Tseng, C. MacAulay, and M. P. Rosin, "Fluorescence visualization detection of field alterations in tumor margins of oral cancer patients.," Clin Cancer Res 12, 6716-6722 (2006).

112. C. F. Poh, S. P. Ng, P. M. Williams, L. Zhang, D. M. Laronde, P. Lane, C. Macaulay, and M. P. Rosin, "Direct fluorescence visualization of clinically occult high-risk oral premalignant disease using a simple hand-held device.," Head Neck 29, 71-76 (2007).

113. K. Matsumoto, "[Detection of potentially malignant and malignant lesions of oral cavity using autofluorescence visualization device]." Kokubyo Gakkai Zasshi 78, 73-80 (2011).

114. M. E. Martin, M. B. Wabuyele, K. Chen, P. Kasili, M. Panjehpour, M. Phan, B. Overholt, G. Cunningham, D. Wilson, R. C. Denovo, and T. Vo-Dinh, "Development of an advanced hyperspectral imaging (HSI) system with applications for cancer detection.," Ann Biomed Eng 34, 1061-1068 (2006).

115. L. Gao, R. T. Smith, and T. S. Tkaczyk, "Snapshot hyperspectral retinal camera with the Image Mapping Spectrometer (IMS)." Biomed Opt Express 3, 48-54 (2012).

Appendix A

Rapid, low-cost optomechanical design and prototyping: the plastic imaging spectrometer

This appendix focuses on the evaluation of plastic rapid prototyping as a technique for producing functional optomechanical parts. In our research setting, rapid prototyping can be more effective than CNC milling in terms of production time and cost. We describe a rapid prototyping procedure to print rigid plastic components for a research device called the Image Mapping Spectrometer (IMS). Results from plastic printing show precision alignment and fitting features can be manufactured faster than with metal milling. Plastic components provide opaque optomechanical structures at a fraction of the cost of metal milling ($1,000 vs. $10,000).

Introduction

Here we describe the design, construction, and testing of custom plastic optomechanics for an Image Mapping Spectrometer (IMS) used in cellular research and clinical studies. The IMS is an imaging spectrometer that consists of an image mapping mirror, relay/dispersive optics, and a CCD camera. A durable, rigid enclosure is important to precisely align the numerous optical components within the IMS and to

shield them from external light. A previous version of the IMS was constructed from a shell of custom metal plates. Although the metal components provided adequate alignment precision and stray light protection, producing the system required 1-3 months of production time and a cost of over $10,000. Consequently, machining custom optomechanics was prohibitive for our application. As a research device, the IMS frequently requires physical modifications to its design. Consequently, rapid prototyping is ideal as a more cost/time efficient method of creating components for the device. Through an analysis of part design, component printing, and post processing, we determined 3D plastic printing to be a practical alternative to traditional metal milling.

Methods

This section details design considerations, provides information about the printing process, and discusses the features of a 3D printer called the Projet SD 3000. Finally, methods used to post-process printed plastic pieces are presented.

Design Considerations

Several design modifications were made to the original metal IMS in order to make a functional plastic prototype. The modifications provide structural stability within the new plastic system, incorporate threads, and integrate precise mounting and alignment features. First, the shell of the original IMS consists of eight long, thin metal plates – one of which is shown in the figure below. The thickness of the plate provided adequate rigidity when constructed from metal, but caused bending and warping when

printed with plastic. Simply increasing the total thickness would increase the overall size and cost of the system. In order to provide additional strength without significantly increasing the thickness of the plastic part, patterned structural features were added to the inside of each plate. For each IMS shell piece, the support features required an additional 1 $in.^3$ of plastic (9.75 $in.^2$ surface area, 0.1 in. thickness).

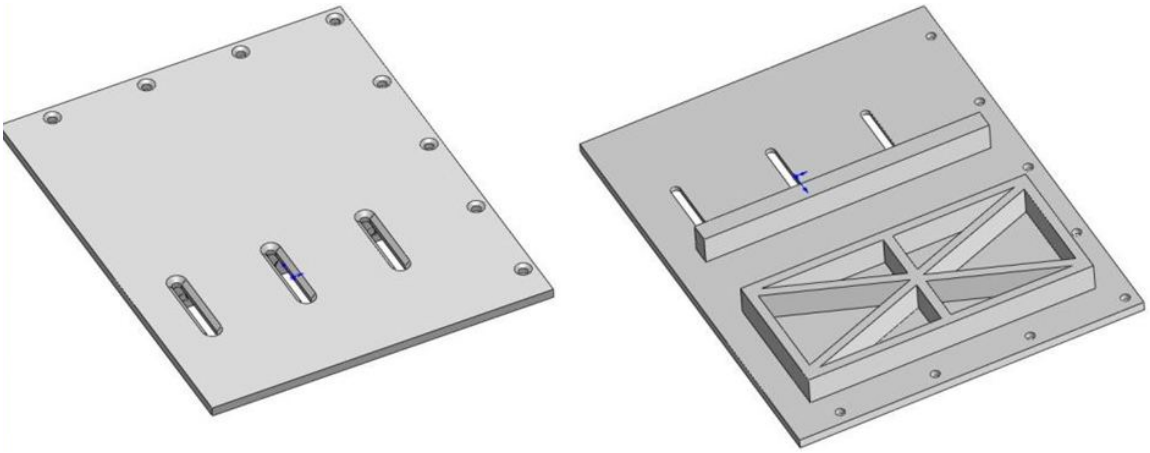

Figure: (left) is the drawing representing a side component of the IMS's metal shell. Triangular additions were appended to the shell's spine to provide additional structural support for the plastic version (right).

Another feature that was added to the original metal design was custom screw threading. In the metal design, threads were indicated with annotations but not physically drawn into the model. Typically, smaller threads are cut with a drill bit and a specialized tapping tool, which requires several steps for each thread location; the process for cutting larger screw threads (greater than 1 in.) is even more tedious. Given the precision and ease with which rapid prototyping creates arbitrary structural features, we found that

printing threads provided convenient time and cost savings. Our custom procedure for drawing a thread is shown in the figure below. Threading involves extruding a hole through a surface, overlaying a helix with a specified pitch, and then extruding a triangle along the path of the helix. Within the complete design of the IMS shell, we implemented 49 custom threads.

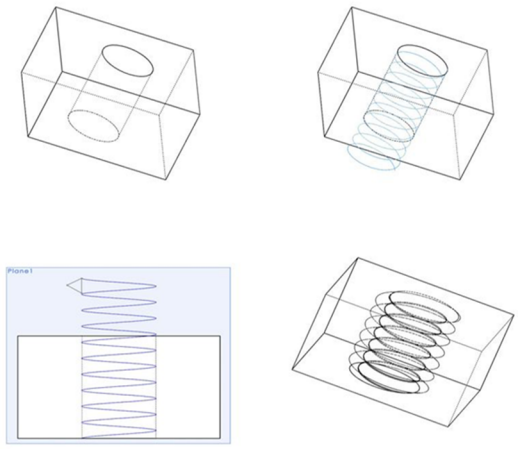

Figure: A cylinder is extruded through a component and given a helix with a pitch of 1/32 in. An equilateral triangle is drawn between one pitch and used to make an extruded cut across the helix.

An additional design modification that we implemented was press-fitted mounts for optical components. Press-fitting involves the connection of two separate entities, held together by friction after an initial force has been applied to join the pieces. In the metal system, press-fitting was not possible because of the parts' high rigidity. Rapid prototyping in plastic is ideal for press-fitting because of its flexible substrate, high-precision, and the ability to quickly iterate feature sizes if necessary. We implemented

press-fitting in the lens array component of the IMS. The mounting part consists of 24 holes arranged in a 4 x 6 configuration. Each hole is printed to the nominal diameter of each lens and includes a stop for depth positioning. The figure below shows a partially press-fitted lens array.

Along with press-fitted mounts, other custom precision alignment features in the plastic design helped to reduce system cost and assembly time. One of these alignment features was a structural support for the prism array assembly, which consists of a rectangular base with protruding cylinders. The prisms are placed between two adjacent protrusions. Neither adhesives nor threads were needed to keep the prisms stationary.

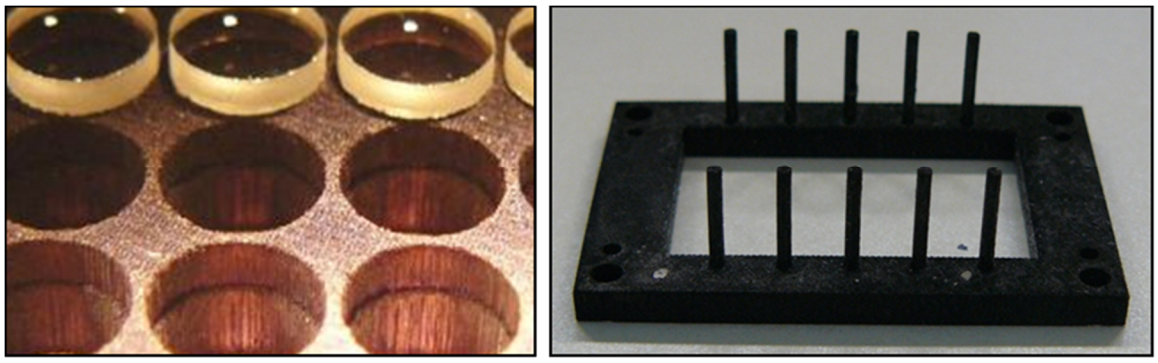

Figure: (left) Lenses are press- fitted into an array without the use of any adhesives. (Right) The cylindrical protrusions on this rectangular base are used to keep a prism array stationary.

Printing

This section describes a procedure for loading 3D files onto the Projet SD 3000 and printing plastic components with high resolution. The resolution of the Projet SD 3000 3D printer is 375 x 375 x 790 DPI, allowing the creation of plastic models with an

accuracy of 0.001-0.002 in. per in. of product. Plastic printing requires a three-dimensional blueprint in the form of a .STL file, which is a format that describes the triangulated surface geometry of part. The .STL file approximates the surfaces of a three-dimensional blueprint with polygons, and Projet recreates the polygons layer by layer during a print job. The figure below illustrates how a .STL file is uploaded onto the Projet software's virtual image of a metal printing plate. The .STL file may be moved to any coordinate on the plate, a feature that allows users to fit multiple files on the printing plate at once. We found that printing parts vertically significantly increased resolution of the part, although this significantly increases printing time.

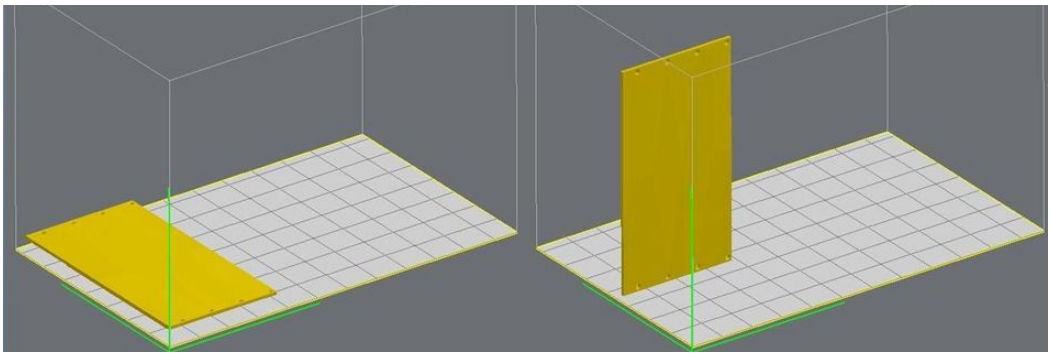

Figure: Printing a part with vertical orientation maximizes the printed resolution.

Post-Processing

The 3D printer creates the plastic part encased in a wax support. To remove the wax, the part is placed in a convection oven called the Projet Finisher. Excess wax deposits are then eliminated in an ultrasonication oil bath (Fig. 7b). Detergent is used to wash off any wax and oil on the plastic. In addition, the plastic used for our application

needs to be opaque to prevent ambient light from entering the system. Two possible post-processing methods for treating plastic include black dying and the application of vinyl sheets. The first method involves immersing the plastic pieces into a black ink bath for two hours and set overnight to dry. A second method employs the use of black, adhesive vinyl. Vinyl is placed over the desired surfaces of a print job and cut to fit the outline of the plastic pieces. The results of each approach are shown in the figure below

Figure: The IMS shell can be given an opaque surface with black ink or adhesive vinyl.

Results

The figure below displays the complete plastic model of the IMS. The plastic shells, with increased structural strength, provide sufficient resistance against physical wear during IMS usage. We found that the use of plastic offers additional benefits that include precision press-fitting and precision alignment, which are techniques that can be used to eliminate the need for adhesives when joining optical components to metal. Savings for time and cost can range from 50% up to 90% when replacing labor intensive techniques such as metal milling with rapid prototyping. While metal machining could require 1-3 months to create the IMS shell, plastic printing accomplishes the same goal in

approximately two days. The speed that plastic printing can output plastic models allows the user to work through several iterations of an optomechanical parts. The lengthy production time for the metal system results in an equally large monetary cost of > $10,000. A plastic device with sufficient structural integrity can be printed at the cost of ~$1,000 by avoiding labor costs. These results support plastic printing as viable solution for manufacturing precise and rigid optomechanical parts.

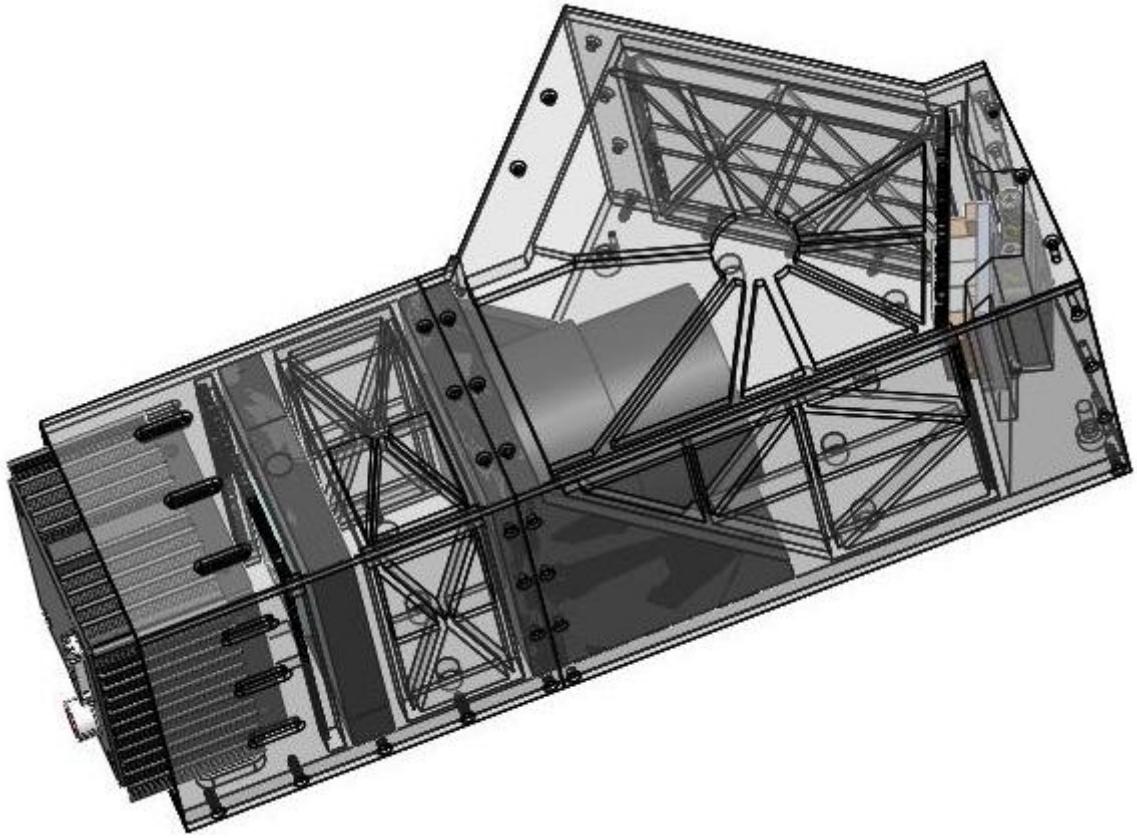

Figure: The complete IMS contains a protective shell that holds the optomechanics. A transparent view of the IMS shell reveals numerous threads that have been extruded into the shell components.

Appendix B

IMS Calibration Summary: Slit-scanning

This appendix describes an alternative to the pinhole scanning technique for geometric/spectral calibration of an imaging spectrometer. The spatial point-source can be replaced with a spatial line-source. Instead of scanning to every spatial position ($x * y$ locations), a line can be scanned once along each spatial dimension ($x + y$ locations), while saving images at each slit location. After data collection, images from any two perpendicular locations can be computationally combined, with the intersection representing a single spatial point. In the case of the IMS, this requires 0.57% the acquisition time of the point-scanning approach, approximately two hours, yet describes the same transformation. This principle is explained in the figure below. The following sections describe how spectral line-scanning was implemented for calibrating the IMS.

A custom setup was built to implement spectral slit-scanning calibration in the laboratory. A 5 µm slit (Thorlabs) was used as the spatial line-source. It was mounted to two motorized translation stages (Newport) and positioned at the sample plane of a standard microscope (Zeiss AxioVert). Using a 5X microscope objective, the slit was magnified to about half the facet width of the mapping mirror. Wavelength tunable trans-illumination was achieved with a halogen lamp and a liquid crystal tunable filter (CRI), which provided light with a spectral full-width half-maximum of approximately 10 nm. A

daylight filter and neutral density filter were also included to flatten the spectrum of the halogen lamp.

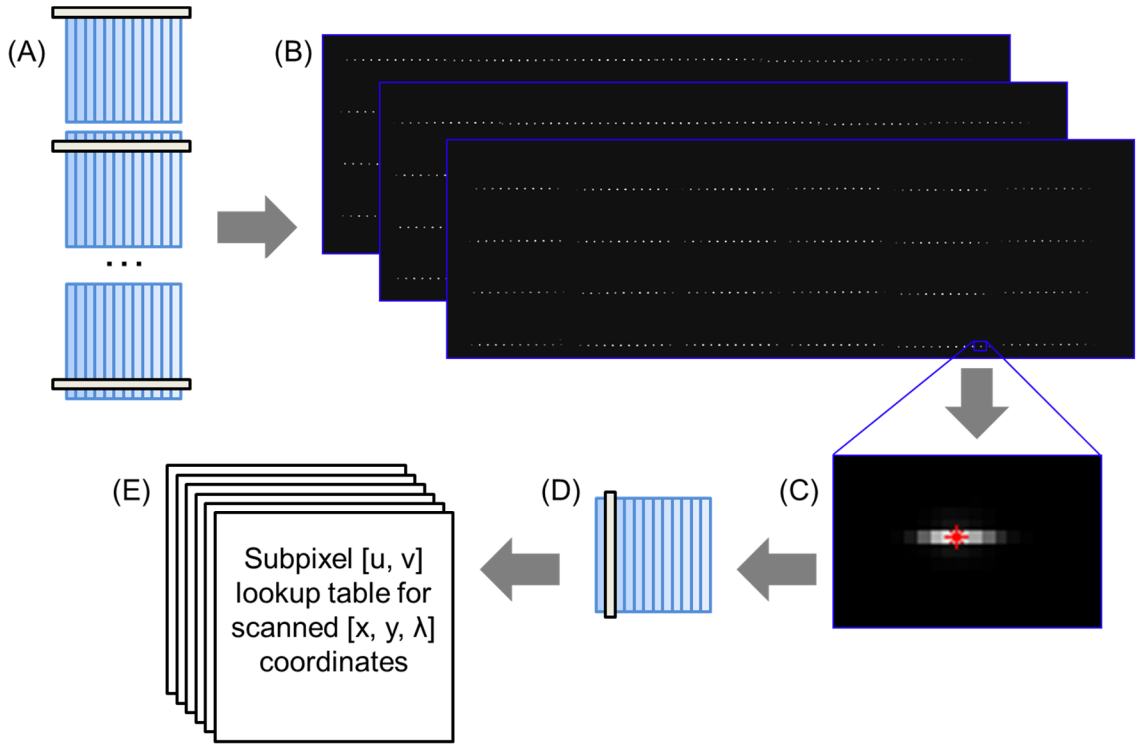

Figure: Concept of line-scanning to obtain system response matrix. (A) A line of monochromatic light is scanned to every spatial-spectral point of object space (x, y, λ), shown here projected on a simplified mapping mirror. (B) A detector image is recorded at each scan position. (C) Each image is analyzed for spatial-spectral point spread functions; here the width is due to the spectral bandwidth used. The subpixel peak (*) of these areas on the detector (u, v) correspond to the position of the scan in object space (x, y, λ). (D) A single perpendicular scan determines the linear arrangement of detected peaks. (E) All subpixel locations are saved into a lookup table that represents the transformation matrix of the system.

Calibration settings were chosen based on the parameters of the IMS. The device was designed to acquire 350 x 350 spatial samples over a FOV of 250 μm with 48 spectral channels between 450 – 650 nm. The tunable filter was programmed to sample the spectral λ dimension at ten evenly spaced steps between 450 – 650 nm. The spatial *y* dimension was sampled at 120 even spaced locations. In order to accurately determine the order of facets, the non-contiguous *x* dimension was sampled at 700 locations for only the 650 nm wavelength.

Once data was collected from the calibration scans, there were several post-processing steps required to obtain the inverse mapping transformation. The following sub-sections describe each part in detail.

Calculating Sub-pixel Detector Locations from Y-Scan Data

The first goal in processing the calibration data was to identify the locations *(u, v)* of point spread functions (PSFs) within every scan image. For each image there were approximately 350 PSFs corresponding to the number of facets in the mapping mirror. Each PSF on the detector was two to three pixels tall and five to six pixels wide; the vertical dimension corresponded to the spatial PSF and the horizontal dimension to the spectral bandwidth of the light. As a first step, dead pixels and hot pixels were eliminated from the data with thresholding and a morphological area opening operation. Weighted centroids were then calculated for all remaining areas in order to approximate sub-pixel locations of PSFs on the detector.

Reducing Noise and Filtering Weighted Centroid Data

Typically several invalid centroids were detected. These points were filtered out based on the fact that the combination of all PSF images from one wavelength should trace approximately 350 lines (facet images) on the detector. Using this assumption, calibration images for a given wavelength were summed and morphologically dilated to produce a boundary region where valid PSFs should appear. Outside points were eliminated with a morphological area opening operation, as shown in the illustration below.

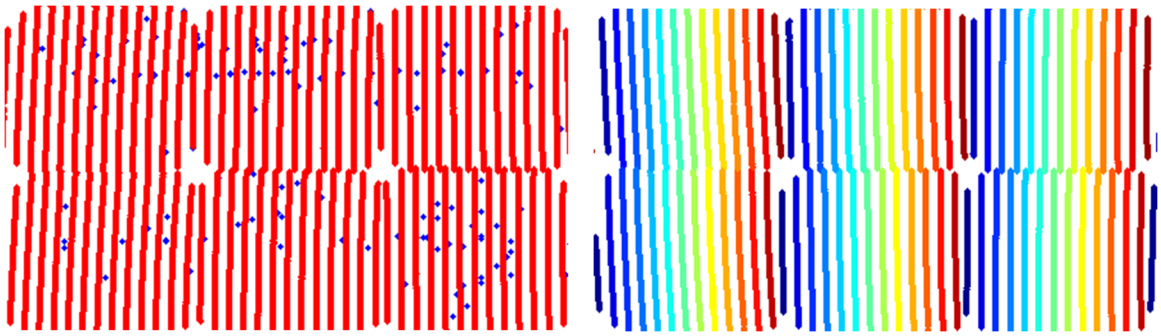

Figure: (Left) A subsection of the detector, with centroid locations for one wavelength shown in red. Blue represents the centroids that were eliminated during noise filtering. (Right) A subsection of the detector, with facet clusters color-coded for one wavelength. Each color represents a cluster of centroids from one mirror facet. The hue of the color represents the spatial position it belongs in the reconstructed cube.

Assigning Additional Dimensions to Centroid Points

Remaining centroids were assigned five parameters that described their position in detector space *(u, v)* and object space *(x, y, λ)*: the sub-pixel coordinates on the detector

indicated the *(u, v)* values, the *y*-scan position indicated the *y* value, and the filter wavelength the λ value. Centroids corresponding to the 650 nm edge wavelength were assigned *x* values based on the *x*-scan position that yielded the highest peak intensity value at *(u, v)*. In other words, the *x*-value indicated the order in which lines were illuminated during the *x*-scan. Centroids from all other wavelength were assigned *x* values as described in Section 3E.

Cluster Analysis to Identify Facet Image Locations

After processing calibration images from the 650 nm wavelength scan, a set of about 35,000 points with five dimensions had been identified. Cluster analysis was used to organize this data. First, a distance was calculated between every centroid in five-dimensional Euclidean space. For example, centroids that were adjacent in *(u, v)* detector space but far apart in *(x, y, λ)* object space were assigned a value between the two distances. Using this distance value, centroids were organized into clusters that corresponded to facets on the image mapper. A distance cutoff of 20 pixels worked to achieve this separation, because it was less than the distance between two adjacent facet images in *(u, v)* detector space, yet greater than the separation between adjacent points within a facet. Finally, all clusters were put in order, from 1 to 350, based on the average *x* value of the contained points.

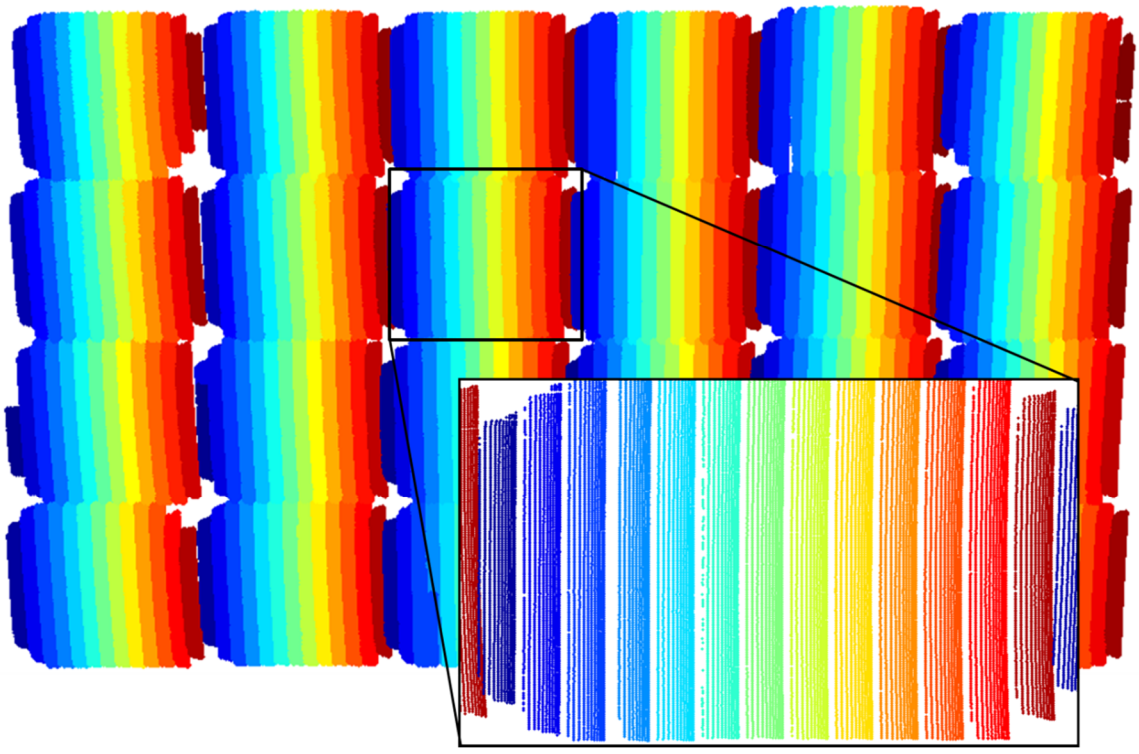

Figure: Color-coded facet clusters for all wavelengths. The hue represents the spatial position in the reconstructed cube. Each vertical line within a color group represents a wavelength position in the cube.